

**University of Alberta**

Photoluminescence and Patterning of Silicon Nanocrystals

by

José Roberto Rodríguez Núñez

A thesis submitted to the Faculty of Graduate Studies and Research  
in partial fulfillment of the requirements for the degree of

Doctor of Philosophy

Department of Chemistry

©José Roberto Rodríguez Núñez  
Spring 2012  
Edmonton, Alberta

Permission is hereby granted to the University of Alberta Libraries to reproduce single copies of this thesis and to lend or sell such copies for private, scholarly or scientific research purposes only. Where the thesis is converted to, or otherwise made available in digital form, the University of Alberta will advise potential users of the thesis of these terms.

The author reserves all other publication and other rights in association with the copyright in the thesis and, except as herein before provided, neither the thesis nor any substantial portion thereof may be printed or otherwise reproduced in any material form whatsoever without the author's prior written permission.

## **Examining Committee**

Dr. Jonathan G. C. Veinot, Chemistry

Dr. Steven H. Bergens, Chemistry

Dr. Arthur Mar, Chemistry

Dr. Jed Harrison, Chemistry

Dr. Alkiviathes Meldrum, Physics

Dr. Matthew Moffitt, Chemistry, University of Victoria

*“It always seems impossible, until it is done”*

Nelson Mandela

I dedicate this thesis to Mom, Dad, Francisco and Tiara, I love you always

## **Abstract**

Silicon nanocrystals (Si-NCs) have been suggested for sensing and lasing applications due to their low-toxicity and compatibility with existing microelectronic technologies. Their broad luminescence, due to homogeneous (150 meV or 40 nm at room temperature) and inhomogeneous broadening, may hamper their incorporation into the aforementioned applications. This thesis begins with a discussion on the optical properties of Si-NCs (Chapter one). Then, it presents methods to decrease the breadth of the luminescence obtained upon photoexcitation of Si-NCs prepared via thermal processing of hydrogen silsesquioxane (HSQ). Narrowing of luminescence profile can be accomplished by sensitization of sharply emissive species. Chapter two outlines a solution processable method to obtain sharp, Si-NC sensitized, erbium luminescence. The luminescence obtained (FWHM Er emission  $\sim$  40 nm) lies in the low-loss window of silica fiber optics and may be useful for telecommunication applications. A method to pattern oxide-embedded Si-NCs using amine containing block copolymers is presented in Chapter 3. This method utilizes gelation of HSQ with amine moieties in the polymer. This straightforward, inexpensive, non-lithographic, patterning technique was also extended to germanium features. Chapter four presents a photo-assisted etching method of Si-NCs. This unique etching method provides a means to control the optical properties of Si-NCs by exposing a Si-NC:HF:HCl mixture to light of varying wavelengths. The narrowest luminescence obtained using this technique is approximately 80 nm (twice the width of homogeneously broadened NCs). A method to prepare Si-NC

coated microcavities is presented in Chapter five. The coupling of NC luminescence to optical cavities produces high quality, whispering-gallery modes which results in sharp peaks ( $\text{FWHM} < 0.5 \text{ nm}$ ) over the broad PL spectrum. A proof-of-concept refractometric sensor using these cavities is also discussed. Finally, Chapter 6 includes general conclusions on the work presented and outlines new research that can be performed to enable incorporation of these materials into everyday technologies.

## **Acknowledgements**

During the time of my doctoral studies at the University of Alberta, I have enjoyed the support of many people. These people have all contributed in different ways to making my time in Edmonton both successful and enjoyable. I want to begin by thanking “The Boss”, Dr. J. G. C. Veinot. After spending a year and a half in another research group, I realized that I needed to move elsewhere and Jon quickly offered me a place to do research in his group. He encouraged me to pursue my research interests and was always supportive of the work I did. I certainly could not have done any of the work presented in this thesis without his support.

I would also like to thank all the people that worked with me in the Veinot research group. When I joined the group, Dr. Colin Hessel, Dr. Eric Henderson, Dr. Janet MacDonald, and De-ann Rollings welcomed me and modeled excellence in conducting research. I learned more science in my first year in the Veinot group than at any other point in my life and this is all largely because of them. I also had the opportunity to work with Dr. Joel Kelly, Sarah Regli, and Melanie Hoffman. Joel, Sarah and Mel made my time at the Veinot group an enjoyable one. With ski trips, ‘quick 20’s,’ pub lunches and getting wedding ready, I was able to step away from research and come back refreshed. I want to thank all of you and I will always remember you. You are awesome. Other individuals in the group I would like to acknowledge are Kevin, Shuai, Shaune, Lydia, Amber, Leah, Rhett, and Pablo. I would also want to thank the members of the Meldrum group who I worked with through the years, specially Kyle, Ross,

Shalon, and Florian. Thank-you for everything you helped me with through the years.

My family has been a constant source of support during my life and I would like to take this time to thank them as well. After moving away from my home country of Ecuador, South America, over 10 years ago, I have continued to feel their love and encouragement just as much as when I was at home. Papi, tu siempre dices que “estás jorobando” pero en realidad siempre estás pensando en mi, y en como puedo ser más para server mejor, gracias siempre. Mami, como siempre digo, gracias por todo; gracias por venir a Canadá, gracias por cada rezo y vela, gracias por acolitarme en cada locura y gracias por aguantar todas las dribladas. Francisco, siempre he podido contar contigo, en las buenas y en las malas, gracias por ser el mejor hermano que uno pueda pedir.

During my Ph.D. studies I also met my lovely wife, Tiara Joy Sharon Rodríguez Núñez. Tiara, thanks for reading all the chapters in this thesis and for listening about each one of the projects I have ever worked on, you are amazing. Your support, prayers, and encouragement have truly been a blessing through the years. I love you always.

Professor J. Takats, Professor J. Buriak, Professor A. Meldrum, Professor J. Harrison are also thanked for their insightful discussions.

Special thanks to Dr. Dimitre Karpuzov and all the staff at the Alberta Center for Surface Engineering and Science. Thanks to Wayne Moffat and all the

staff at the Analytical and Instrumentation Laboratory. Thanks to George Braybrook at the Earth and Atmospheric Science, SEM facility.

Most importantly, I want to thank God for blessing me with such amazing people and experiences in my life during these last few years. I couldn't be more grateful. Thank-You.

## Table of Contents

<b>Chapter 1: Introduction to Semiconductor Nanocrystals and their Optical Properties.....</b>	<b>1</b>
1.1. Introduction to Nanoscale Materials .....	2
1.2. Quantum Dots.....	5
1.3. Bonding in Solids.....	9
1.3.1. Direct and Indirect Bandgap semiconductors.....	13
1.4. Size effects in semiconductor nanocrystals.....	18
1.4.1. Quantum confinement in semiconductor nanocrystals.....	18
1.5. Silicon Nanocrystals.....	22
1.5.1. Optical properties of Si-NCs.....	24
1.5.1.1. Erbium Sensitization using oxide embedded silicon nanocrystals.....	25
1.5.1.2. Homogeneous and Inhomogeneous broadening.....	27
1.5.2. Methods to prepare Silicon Nanocrystals.....	29

1.5.2.1.	Physical Methods for preparing silicon nanocrystals.....	29
1.5.2.2.	Chemical methods for preparing silicon nanocrystals.....	30
1.5.2.3.	Synthesis and thermolysis of Sol-gel Derived Silicon rich oxides.....	32
1.6.	Thesis outline.....	37
1.7.	References.....	40
<b>Chapter 2: Realization of Sensitized Erbium Luminescence in Silicon Nanocrystal Composites.....</b>		<b>45</b>
2.1.	Introduction.....	46
2.2.	Experimental Details.....	50
2.2.1.	Material preparation.....	50
2.2.1.1.	Erbium chloride ( $\text{ErCl}_3$ ) and Erbium tris(bis(trimethyl) silyl) amide (ErA) precursor mixtures.....	50
2.2.1.2.	Erbium octanoate (ErOct) solution preparation.....	52

2.2.1.3.	Preparation of Er-doped Si-NC/SiO <sub>2</sub> composites.....	52
2.2.2.	Material Characterization.....	52
2.2.2.1.	Fourier Transform IR spectroscopy (FTIR).....	52
2.2.2.2.	Scanning electron microscopy (SEM).....	53
2.2.2.3.	X-ray photoelectron spectroscopy (XPS).....	53
2.2.2.4.	X-ray diffraction (XRD).....	54
2.2.2.5.	Photoluminescence (PL) measurements.....	54
2.2.2.6.	<i>In situ</i> PL during HF etching of composites.....	54
2.2.2.7.	Nuclear Magnetic Resonance (NMR).....	55
2.3.	Results and Discussion.....	56
2.4.	Conclusions.....	74
2.5.	References.....	75

<b>Chapter 3: Patterning of Silicon and Germanium Nanostructures</b> .....	78
3.1. Introduction.....	79
3.2. Experimental Details .....	84
3.2.1. Material preparation.....	84
3.2.1.1. Solution preparation.....	84
3.2.1.1.1. PS-b-P4VP and PS-b-PMMA.....	84
3.2.1.1.2. Hydrogen Silsesquioxane (HSQ) solutions.....	85
3.2.1.1.3. Tetraethoxygermane solutions.....	85
3.2.1.2. Patterning of silicon and germanium nanostructures.....	85
3.2.1.3. Thermal Processing of Silicon nanostructures.....	86
3.2.1.4. Thermal Processing of Ge nanostructures.....	86
3.2.2. Material Characterization.....	87
3.2.2.1. Atomic Force Microscopy (AFM).....	87
3.2.2.2. X-ray photoelectron spectroscopy (XPS).....	87

3.2.2.3.	Scanning Electron Microscopy (SEM) and Auger Electron Spectroscopy (AES) .....	88
3.2.2.4.	Thermal Gravimetric Analysis (TGA).....	89
3.3.	Results and Discussion.....	90
3.3.1.	Patterning of Silicon Nanostructures .....	90
3.3.2.	Patterning of Germanium Nanostructures.....	100
3.4.	Conclusions.....	109
3.5.	References.....	111
<b>Chapter 4:</b>	<b>Photoassisted Etching of Oxide Embedded Silicon Nanocrystals.....</b>	<b>114</b>
4.1.	Introduction.....	115
4.2.	Experimental Details.....	121
4.2.1.	Material preparation.....	121
4.2.1.1.	Composite preparation.....	121
4.2.1.2.	Etching of OE-Si-NCs using HCl(aq), HNO <sub>3</sub> (aq), and H <sub>2</sub> SO <sub>4</sub> (aq).....	121
4.2.1.3.	Laser etching of OE-Si-NCs.....	122

4.2.1.4.	Functionalization of OE-Si-NCs.....	123
4.2.2.	Material Characterization.....	124
4.2.2.1.	Photoluminescence (PL) Spectroscopy...	124
4.2.2.2.	Small Angle X-ray scattering (SAXS)....	124
4.3.	Results and Discussion.....	126
4.3.1.	Optical properties.....	128
4.3.2.	Etching mechanism.....	137
4.3.3.	Size distribution.....	143
4.4.	Conclusions.....	150
4.5.	References.....	152
<b>Chapter 5:</b>	<b>Coating of Cylindrical Microcavities with Oxide Embedded Silicon Nanocrystals.....</b>	<b>155</b>
5.1.	Introduction.....	156
5.2.	Experimental Details.....	160
5.2.1.	Materials preparation.....	160
5.2.2.	Coating of Cylindrical microcavities with oxide-embedded silicon nanocrystals.....	160
5.2.3.	Materials Characterization.....	162

5.2.3.1.	Photoluminescence Imaging and Spectroscopy.....	162
5.2.3.2.	Scanning Electron Microscopy.....	162
5.2.4.	Capillary mode indexing.....	163
5.3.	Results and Discussion.....	164
5.3.1.	Whispering-Gallery Modes in Capillaries.....	164
5.3.2.	Whispering-Gallery Modes in Fiber Optics.....	170
5.4.	Conclusions.....	178
5.5.	References.....	180
<b>Chapter 6:</b>	<b>Conclusions and Future Work.....</b>	<b>182</b>
6.1.	Conclusions.....	183
6.2.	Future work.....	190
6.3.	References.....	191
<b>Appendix A:</b>	<b>Functionalization of thin Oxide-Embedded Silicon Nanocrystal films with Oligonucleotides.....</b>	<b>192</b>
A.1.	Introduction.....	193
A.2.	Experimental.....	195

A.2.1. DNA functionalization of glass and OE-Si-NC surfaces.....	195
A.2.2. X-ray photoelectron spectroscopy (XPS).....	197
A.2.3. Photoluminescence (PL) measurements.....	197
A.3. Results and Discussion.....	198
A.4. Conclusions and Future work .....	202
A.5. References.....	203
<b>Appendix B: Capillary and Fiber Mode Modeling and Indexing.....</b>	<b>204</b>
B.1. Mode Modeling and Indexing.....	205
B.2. References.....	207

## List of Tables

<b>Table 2.1</b>	Synthesis of Erbium containing Si-NC/SiO <sub>2</sub> composites.....	51
<b>Table 3.1</b>	Molecular weights of PS-b-P4VP polymers used for patterning of Group IV semiconductor nanostructures.....	84
<b>Table 3.2</b>	Solutions used to produce OE-Si-NP and germanium patterns....	86
<b>Table 3.3</b>	Particle to particle spacing, particle diameter, and particle height of the resulting OE-Si-NP patterns.....	95
<b>Table 3.4</b>	Particle height and diameter of patterns heated to 400 °C, 470 °C, and 500 °C.....	105
<b>Table 4.1</b>	Conditions of samples etched using different acids.....	122
<b>Table 4.2</b>	PL max and FWHM of photoetched samples before and after functionalization.....	144
<b>Table 4.3</b>	Calculated diameter from the PL spectra before functionalization (b.f) and after functionalization (a.f.) using the reduced mass approximation. Diameter and size distribution obtained from SAXS of dodecene functionalized particles.....	146
<b>Table 4.4</b>	Calculated diameter and standard deviation of two-step, water, and acid only etched samples using the reduced mass approximation and SAXS.....	148

## List of Figures

- Fig. 1.1** a) As orbital overlap increases the spacing between energy levels increases. b) Orbital energies for a chain of H atoms as the chain length increases (image adapted from Ref. 42).....10
- Fig 1.2** A representation of the filled and empty bands in an a) insulator, b) semiconductor, and c,d) metal (image adapted from Ref. 31).....13
- Fig. 1.3** Absorption coefficients of common semiconductors. InP and GaAs show a sharp decrease in the absorption coefficient at the bandgap energies. Si and Ge show a gradual decrease (image adapted from Ref. 48).....14
- Fig. 1.4** Pictorial representation of energy vs. momentum wave vector ( $k$ ) for a) a direct bandgap semiconductor and an b) indirect bandgap semiconductor. In a) the bottom of the CB and the top of the VB occur at the same value of  $k$ , in b) the values of  $k$  are different. (image adapted from Ref. 1).....16
- Fig. 1.5** Density of states for a semiconductor. As crystal size decreases, discrete energy levels appear in the band structure (image adapted from Ref. 22).....19

<b>Fig 1.6</b>	a) Pictorial representation of the increased bandgap observed in semiconductor nanocrystals due to the erosion of the bands. b) Quantum confinement effects in the absorption of CdS quantum dots showing a shift in the absorption energy. (image adapted from Ref. 53).....20
<b>Fig. 1.7</b>	a) PL spectra of HF etched silicon nanocrystals spanning the visible range. b) Mechanisms of light emission (image adapted from Ref. 68 and Ref. 71).....25
<b>Fig. 1.8</b>	a) Structure of commercially available HSQ. b) Patterning of OE-Si-NCs via e-beam lithography of HSQ. The images on the far right show the characteristic red PL after photoexcitation.....36
<b>Fig. 2.1</b>	Photoluminescence spectra of composites containing (a) ErCl <sub>3</sub> (1a-4a), (b) ErA (5a-8a), and (c) ErOct (9a-12a). Composites were drop coated onto silicon wafers and excited using the 325 nm line of a He/Cd (not resonant with Er <sup>3+</sup> excitation). All spectra are normalized to the silicon luminescence.....59
<b>Fig. 2.2</b>	Backscattered SEM images of composites 3a (a), 4a (b), 7a (c), 8a (d), 11a (e), and 12a (f); bright spots are microscopic erbium clusters. EDX of 4a (g), 8a (h), and 12a (i) was collected by focusing on the bright spots in the backscattered electron images. EDX suggests the presence of ErCl <sub>3</sub> in sample 4a.....62

- Fig. 2.3** NMR of HSQ mixed with ErA at -80 °C (a), -60 °C (b), -40 °C (c), -30 °C (d). Inset on (d) shows the mixture at -30 °C for a few minutes. At -40 °C a small peak can be seen at 4.5 ppm characteristic of H<sub>2(g)</sub>. At -30°C a clear decrease in the Si-H peak (4.26 ppm) is observed while the H<sub>2(g)</sub> signal increases.....65
- Fig. 2.4** IR spectra showing the disappearance of the OH stretch (~ 3200 cm<sup>-1</sup>) and the appearance of the C-O symmetric and asymmetric stretches upon acid coordination.....66
- Fig. 2.5** XRD patterns of samples 4a, 8a, 12a, and 13a. The 111, 220 and 311 reflections are clear in the control sample and visible in sample 4a, other composites show small or undetectable peaks. Samples were run on a silicon <100> holder.....68
- Fig. 2.6** XP spectra of samples 4a, 8a, 12a, and 13a. Spectra were normalized to the highest intensity Si(IV) peak. Samples 8a and 12a have lower Si (0) intensity compared to samples 4a and 13a. ErA (8a) sample displays more suboxide character than all other samples.....70
- Fig. 2.7** In situ HF etching of samples 13a (a), 4a (b), 8a (c), and 12a (d). Intensity changes upon etching are shown by the arrows. Erbium emission disappears after 15 minutes of etching, similar to the time it takes to remove the SiO<sub>2</sub> matrix in sample 13a (a). Comparison of the Si-NC luminescence intensity in (a) and (b) shows some of the NC energy is being transferred into the Er<sup>3+</sup>.....73

<b>Fig 3.1</b>	AFM images of all PS-P4VP polymers used to pattern silicon nanoparticles. The features observed are due to the P4VP block segregating. The particle-to-particle spacing is directly proportional to the PS MW.....	93
<b>Fig. 3.2</b>	a) AFM of BCP 4 on Si, heated to 1100 °C in the absence of HSQ, b) HSQ spin coated on Si heated to 1100 °C in the absence of BCP, c) SEM of a pattern resulting from spin coating HSQ with BCP 4 after heating to 1100 °C, d) AFM of OE-Si-NPs patterns on Si with BCP 1, e) BCP 3, f) BCP 4.....	95
<b>Fig. 3.3</b>	a) TGA of block copolymers heated under air and b) under 5 % H <sub>2</sub> /95 % Ar.....	96
<b>Fig. 3.4</b>	a) AFM images of BCP 1/HSQ features before heating (inset shows formation of islands) and b) after heating. c) AFM images of BCP 4/HSQ features before heating and b) after heating.....	98
<b>Fig. 3.5</b>	a) XP spectrum obtained from an HOPG substrate patterned with BCP 3 and HSQ after heating. b) Expected structure and composition of patterned features.....	99
<b>Fig. 3.6</b>	a) BCP 3/TEOG patterns heated to 350 °C and b) 500 °C. c) BCP 3 heated to 350 °C without TEOG.....	103

<b>Fig. 3.7</b>	XP spectra of substrates patterned with BCP 2 and TEOG after heating to a) 470 °C and to b) 500 °C and their corresponding AFM images (e and f, respectively). c) Characteristic SEM image of a patterned substrate using BCP2/TEOG on Si heated to 470 °C. d) Characteristic AFM image of a substrate patterned using BCP 2 and TEOG heated to 400 °C.....105
<b>Fig. 3.8</b>	a) Secondary electron SEM image showing patterns obtained from heating a sample of TEOG and BCP 2 to 400 °C. b) AES point measurements of the areas shown in a). c) High resolution SEM confirming the presence of features on the substrate.....107
<b>Fig. 3.9</b>	Structure of a) PS-P4VP and b) PS-PMMA, the pyridyl moiety can act as a catalytic base in sol gel polymerization. c) Patterned substrate using PS-PMMA, d) Resulting surface after two step heating PS-b-PMMA patterned substrate. e) Representative AFM image of a substrate patterned using TEOG/PS-b-PMMA heated using two-step process.....108
<b>Fig. 4.1</b>	Schematic of the size control expected using exciton mediated etching of silicon nanocrystals.....119
<b>Fig. 4.2</b>	IR spectra of FS-Si-NCs etched using and HF <sub>(aq)</sub> , HCl <sub>(aq)</sub> , EtOH mixture under ambient light (sample 5) for 1, 5, and 10 minutes. Ethanol is added after 5 minutes.....128

<b>Fig 4.3</b>	PL spectra of toluene extracted FS-Si-NCs etched using and HF, HCl, ethanol mixture (see samples 1-5 experimental section) when exposed to no light (a), 700 nm (b), 600 nm (c), 500 nm (d), and ambient light (e).....129
<b>Fig 4.4</b>	(a) PL maximum of Si-NCs in toluene as a function of etching time etched under different irradiation conditions. The dark, 700 nm and 600 nm photoetched samples behave as expected, while the 500 nm and ambient light appear more erratic. (b) Full-width at half maximum as a function of etching time. The high energy photoetched particles display a noticeable spike of the FWHM..131
<b>Fig. 4.5</b>	a) PL of etched silicon nanocrystals extracted into toluene displaying a blueshift with increasing etching time, nanocrystals were radiated with the 647 nm line for the first four hours and then with the 568 nm line for the last four hours. b) PL of etched silicon nanocrystals extracted into toluene displaying a blueshift with increasing etching time. c) A plot of PL max (green traces) and FWHM (purple traces) as a function of etching time for nanocrystals extracted into toluene (solid line) and nanocrystals in the etching mixture (dashed).....136
<b>Fig. 4.6</b>	PL spectra of Si-NCs etched in the dark (a), and with 600 nm irradiation (b) using $H_2SO_{4(aq)}$ . Plot of PL max (c) and FWHM (d) as a function of time showing an intermediate behaviour between etching with $HNO_{3(aq)}$ and $HCl_{(aq)}$ .....140

<b>Fig. 4.7</b>	PL spectra of composites etched with water at pH 0.5 (a), 1.0 (b), 3.5 (c), and 6.6 (d). Plot of photoluminescence maxima as a function of time for different pH etching solutions (e).....	142
<b>Fig. 4.8</b>	PL spectra of photoetched Si-NCs in the dark, ambient, and using 568 nm laser irradiation before (a) and after (b) functionalization.....	144
<b>Figure 4.9</b>	PL before (a) and after (b) functionalization for samples etching using a two-step etch, a “water” etch, and an “acid” etch.....	148
<b>Fig. 5.1</b>	Schematic of planar, disk, and sphere microcavities. (Adapted from Ref. 22 and Ref. 12).....	158
<b>Fig 5.2</b>	a), b) Films of OE-Si-NCs in 25 μm capillaries, the dark brown colour suggests the film is thick c) Defect-free films. d) 50x magnification of a section from c). Optical luminescence image of an OE-Si-NC film excited using the 488 nm line of an Ar <sup>+</sup> laser.....	165

<b>Fig. 5.3</b>	<p>a) Schematic of the experiment.. The capillary (light blue) coated with OE-Si-NCs (light orange) is excited from the side using the 488 nm line of an Ar<sup>+</sup> laser. The PL is collected by a microscope lens located under the capillary. b) Representative PL spectrum taken from the end of a 25 μm capillary. Low <i>Q</i>-factors (ca. 100) are obtained when upon collecting the light from the end of the capillary. c) Fluorescence image of the tip of a 25 μm inner diameter capillary, in which the blue pump laser light defines the outer diameter of the capillary.....167</p>
<b>Fig. 5.4</b>	<p>a) PL spectra of 100, 50, and 25 μm capillaries taken perpendicular to the axis. Dots above the spectra show modeling data (solving Eq. (1) and (2)) for first-order modes. c) Theoretical intensity profile (derived from Eq. 4) for the luminescence from a cylindrical WGM in a 25 μm inner-diameter capillary.....168</p>
<b>Fig. 5.5</b>	<p>a) SEM image of a Si-NC-coated fiber, with a smooth, crack-free coating. b) Cross-sectional SEM image showing a 70-nm-thick NC film on the fiber surface. SEM images were obtained using a 5 keV beam in the secondary electron imaging mode. c) Optical microscope image of a 125-μm-wide Si-NC-coated fiber. d) PL image of the fiber in c) excited by the 488 nm line of an Ar<sup>+</sup> laser incident from the left side of the image.....171</p>

<b>Fig. 5.6.</b>	a) Spectral image of a Si-NC-coated fiber, where intensity increases from blue to red. b) Spatial profile of the emission taken along the direction of the black line shown. c) Magnified view of a section of mode spectrum showing the WGM structure in more detail. The dashed line corresponds to a numerical fit using a single Lorentzian on top of a Gaussian background. The black circles represent calculated resonant solutions for radial index $p=1$ for angular mode numbers $l$ between 752 and 760. Inset shows a profile across the direction of intense PL of the image in a), the resonant peaks are clearly visible over a broad PL background.....	173
<b>Fig. 5.7</b>	WGM spectra for different concentrations of a) EG and b) glucose in water. Insets: Resonance peak shift as a function of the concentration and the refractive index change for the peak marked with the red line. The solid and dashed lines are the best fit and calculated mode shifts, respectively. $R^2$ values are better than 0.95 for both linear fits shown.....	176
<b>Fig. A.1</b>	Schematic of a DNA based sensor using WGMs.....	194
<b>Fig. A.2</b>	Amine modifier used to attach DNA to a quartz or OE-Si-NC surfaces. b) DNA bases.....	196

**Fig. A.3** a) PL of a quartz surface exposed to fluorescently labeled DNA (green trace) and a control quartz substrate not exposed to fluorescent DNA (blue trace). XP spectra of an OE-Si-NC surface with covalently bound DNA showing the b) Si (2p), c) P (2p), and d) N (1s) binding energies.....200

## List of Schemes

<b>Scheme 1.1.</b>	a) Hydrolysis and b) condensation reactions of molecular silicon precursors.....	33
<b>Scheme 1.2</b>	Mechanism of hydrolysis under a) acidic and b) basic conditions. Mechanism of condensation under c) acid and d) basic conditions.....	34
<b>Scheme 2.1</b>	Proposed amine based catalysis of Si-H moieties in HSQ. Resulting silanols can crosslink via condensation releasing water.....	63
<b>Scheme 3.1</b>	a) Commercially available HSQ yields OE-Si-NCs upon thermal processing. b) PS-P4VP self-assembles into micelles which can crosslink HSQ. Upon thermal processing, the features are expected to contain Si-NPs embedded in a silica matrix.....	92
<b>Scheme 3.2</b>	Suggested crosslinking mechanism for TEOG crosslinking in the presence of P4VP.....	102
<b>Scheme 4.1</b>	Etching mechanism based on oxidation of silicon surface. An oxidizing agent (nitric acid in this case) is necessary for this process to occur. Once the oxide surface is formed it can be etched away via HF acid.....	117
<b>Scheme 4.2</b>	Exciton mediated etching mechanism of silicon surfaces using hydrofluoric acid.....	118

**Scheme A.1** Quartz and OE-Si-NC surfaces have hydroxyl groups on the surface which can undergo epoxysilanization upon standard based catalyzed sol-gel reaction. The epoxide ring is opened using an amine terminated DNA strand dissolved in water.....199

# Chapter 1:

## Introduction to Semiconductor Nanocrystals and their Optical Properties

## **1.1. Introduction to Nanoscale Materials**

People in the Neolithic period started shaping rocks to make utensils and weaponry, since then, humans have been using materials to address societal needs. Looking at the development of materials through most of history there are two common themes: 1) a new material is discovered and 2) a property unique to the material is exploited. Up until the 18<sup>th</sup> century, discovery of new materials primarily occurred serendipitously, while the processing of these new materials to obtain desired characteristics was almost always a result of an empirical approach.<sup>1</sup> It is only in the last 200 years scientists began to understand why particular syntheses or processes yielded materials of specific properties.<sup>1</sup> Today, the relationship between the structure of materials at atomic or molecular scales and their macroscopic properties is widely recognized as an essential part of the scientific endeavour and the field of Materials Science.<sup>2</sup>

More recently, attention has turned to materials with dimensions below 100 nm. These materials are called nanomaterials and often have unique and potentially useful properties that differ from those of their bulk and atomic counterparts.<sup>3</sup> As a result of this apparent potential, nanotechnology, and in turn nanoscale materials are of important societal and economic value.<sup>4</sup> Governments, and industries in developed countries are investing a significant amount of money in nanomaterials ensuring their presence in society and in turn exposure of humans and wildlife to it.<sup>5</sup>

Dr. Mihail Roco, a senior advisor for nanotechnology at the National Science Foundation, led a study entitled Nano2 that assesses the past decade of nanomaterials research and potential projects for the next decade. Nano2 makes three key recommendations for future research: 1) continue fundamental research in nanotechnology, 2) initiate public education regarding the developments and challenges of nanotechnology and nanomaterials, and 3) establish an understanding of safety and health consequences of utilizing nanomaterials.<sup>6</sup>

These recommendations are being addressed to varying degrees. Fundamental research in the field of nanomaterials is not diminishing. A testament to this is the increasing number of nanoscience journals that have appeared.<sup>7,8</sup> In addition, Nobel prizes recognizing work focused on nanoscience and nanomaterials have been awarded. The most recent examples are the work focused on solid surface reactivity (Gerhard Ertl, 2007), giant magnetoresistance (Albert Fert and Peter Grünberg, 2007), and the synthesis and properties of graphene (Andre Geim and Konstantin Novoselov, 2010).<sup>9</sup> To maintain and even expand the quality of research in nanomaterials and nanoscience, many universities now offer undergraduate and graduate courses in this field.<sup>10,11</sup> Some institutions have entire degrees dedicated to this field of study.<sup>12</sup> These efforts are effectively addressing (whether intentional or not) the second recommendation of Nano2 quite effectively. Very recently, researchers have begun to evaluate the potential risks associated with nanomaterial implementation.<sup>13,14</sup> Potential environmental impacts such as any toxicological effects of materials used for *in vivo* applications must be considered. It is reassuring to see many toxicological

studies emerging which systematically describe the potential risks of nanosystems. Toxicological properties are just as important as the property that makes the material unique and pose significant challenges when commercializing a product.

## 1.2. Quantum Dots

Quantum dots (QDs) are a type of nanomaterial with unique optical and electronic properties that could revolutionize photonics as well as biological and medicinal applications.<sup>1,15-17</sup> QDs are semiconductor nanocrystals most commonly containing elements of Group II and VI or III and V of the periodic table.<sup>1</sup> Study of their unique size dependent properties was pioneered by Dr. Louis Brus from Bell laboratories.<sup>18-20</sup> Since then, researchers have developed methods to control their size and shape by modifying the duration, temperature, and ligand molecules used in their synthesis.<sup>21</sup> These materials are unique because of the exquisite tunability of their physical, electronic, and optical properties available simply by controlling their particle size.<sup>22</sup> Using CdS QDs as an example, increasing the crystal size causes the melting temperature to increase from 400 °C to 1600 °C, the bandgap to decrease from 4.5 to 2.5 eV, and the radiative lifetime to increase from picoseconds to nanoseconds.<sup>22</sup> As a result of their size-dependent bandgap, nanocrystal optical luminescence can be tuned across a wide range of wavelengths.<sup>22</sup> Two effects are responsible for these observations: the large number of high energy surface atoms and the appearance of size effects.<sup>22</sup> Surface atoms contribute to increasing the free energy of any material. The large fraction of surface atoms in QDs is responsible for altering the thermodynamic properties of nanosized materials.<sup>22</sup> In addition, variations in electrical and optical properties occur through systematic changes of the density of states as size decreases.<sup>22</sup> These variations are termed quantum size effects and explain the change in bandgap or radiative lifetimes with size.<sup>22</sup> Because these

properties arise only by decreasing particle size, they are not only specific to CdS QDs. In general, all semiconductor NCs exhibit marked changes in their properties as size decreases. However, the size at which these changes become apparent is dependent on the atoms that make up the material and their bonding geometry.

QDs can be synthesized via a variety of methods. High-temperature colloidal growth using molecular precursors is commonly used to prepare QDs. Generally, this method uses organic or inorganic ligands to prevent agglomeration of the particle as it grows.<sup>23</sup> In addition, synthetic methods have been developed to cap the nanocrystal with larger bandgap materials, CdSe-core, ZnS-shell QDs being the most widely studied example.<sup>24</sup> Other synthetic methods involve thermolysis of silicon or germanium rich oxides to produce Si and Ge QDs. In addition, CdSe (the workhorse material in this field), CdS, Si, among others can be synthesized via mechanical ball milling.<sup>25-27</sup> Since the unique properties of QDs are due to the size of the particles, it should be clear that single-size clusters with well-defined surfaces are of paramount importance for the understanding and development of this field.

Tunability of the bandgap and optical properties of QDs has been utilized for immunofluorescence labelling of fixed cells and tissues, immunostaining of membrane proteins, and *in situ* fluorescence hybridization of chromosomes.<sup>16</sup> The resistance of QDs to photobleaching also makes these materials ideal for biological tagging applications.<sup>16</sup> In part because of these properties, II-VI QDs are currently being commercialized for a number of applications.<sup>28</sup> As these

materials become more widely available, a thorough understanding of their toxicity is of utmost importance.<sup>29</sup> It has been found that depending on the concentration, many of the Cd based QDs render different cells non-viable.<sup>29</sup> Toxicity has been reported to also depend upon size, surface charge, surface coating, as well as oxidative, photolytic, and mechanical stability.<sup>29</sup> In addition, the long biologic half-life of the II-VI QD precursors is of great concern ( $\text{Cd}^{2+}$  has a biological half-life of 15-20 years) when considering commercialization of these materials.<sup>29</sup> The ban of Cd based electronics (with a few exceptions) by the European Union in 2004 serves to highlight the importance of toxicity in the incorporation of nanomaterials into everyday use products.<sup>30,31</sup>

Toxicology concerns of II-VI and III-V semiconductors led to substantial research investigations into alternative materials that are expected to be less toxic (e.g., silicon).<sup>32-36</sup> Unlike the components of II-VI and III-V compound semiconductor QDs, Si is non-toxic and an essential nutrient for humans.<sup>37</sup> Bulk, porous-Si (p-Si), silicon nanowires and silicon nanocrystals exhibit minimal toxicity under a number of conditions.<sup>32-34</sup> In the human body, Si-NCs are believed to be metabolized to silicic acid, which is readily cleared by the kidneys.<sup>38</sup> Their low toxicity has made it possible for silicon nanomaterials to be commercialized in drug delivery devices (pSivida Corporation) that can release a drug payload over a period of months or years.<sup>39</sup> Low-toxicity must be accompanied by optical properties comparable to those of II-VI and III-V semiconductors if Si is to be an effective replacement. The luminescence of Si-NCs can be tuned from the NIR to visible wavelengths and has been reported to

exhibit PL quantum yields as high as 70% depending on the particle size, and surface functionality.<sup>40</sup> The excited state lifetimes of Si-NCs are long in comparison to the workhorse material in this field, CdSe. In addition, the luminescence profile and size distribution are broader than what can be obtained from CdSe or other compound semiconductors.<sup>41</sup>

Research in the field of QDs is expanding. Education about the technological potential of these particles is becoming common place in undergraduate programs.<sup>1</sup> Studies evaluating the toxicity of these nanomaterials are advancing and will provide policymakers with appropriate information to make informed decisions. Concerns over the toxicity of Cd based QDs was not taken as a setback by the scientific community, rather as a challenge to develop materials with similar optical and electrical tunability as Cd based QDs with reduced toxicity. Efforts like these will continue to drive research in the field of nanomaterials which may well shape a new technological age.

### 1.3. Bonding in Solids

When a large number of atoms form an extended solid, the resulting electronic structure that arises is not straightforward to envision. Two methods to solve this problem are: 1) solving the Schrödinger equation exactly for a periodically repeating system or 2) using a linear combination of atomic orbitals (LCAO) to obtain the approximate molecular orbital picture.<sup>42</sup> Using the first method is complicated (exact solutions do not exist for small molecules). The second method is routinely used for small molecules and provides a reasonable approximation for extended solids.<sup>42</sup>

The simplest description of LCAO arises using H atoms and combining their 1s orbitals to form a chain. If two H atoms come together, their orbitals can combine in-phase (the 1s wavefunctions combine constructively) forming a bonding orbital or out-of-phase (the 1s wavefunctions combine destructively) forming an anti-bonding orbital. The bonding and anti-bonding orbitals are lower and higher in energy than the original atomic 1s orbitals (Figure 1.1.a).<sup>42</sup> When orbital overlap is high, there is a large difference in energy between the bonding and anti-bonding orbitals (Figure 1.1.a). Orbital overlap is directly proportional to bond strength, therefore a strong bond will be one where the energy difference between a bonding and anti-bonding orbitals is large and vice versa.<sup>42,43</sup> As the number of atoms in a theoretical chain of H atoms increases, bonding and anti-bonding orbitals are added. The new orbitals appear at higher and lower energies than the starting bonding and anti-bonding orbitals (Figure 1.1.b). As the number of levels increases the spacing between the energy levels becomes smaller. This

means that for a very large number of atoms (e.g., an infinite chain) the energy levels will be approximated by a continuum that is referred to as a band.

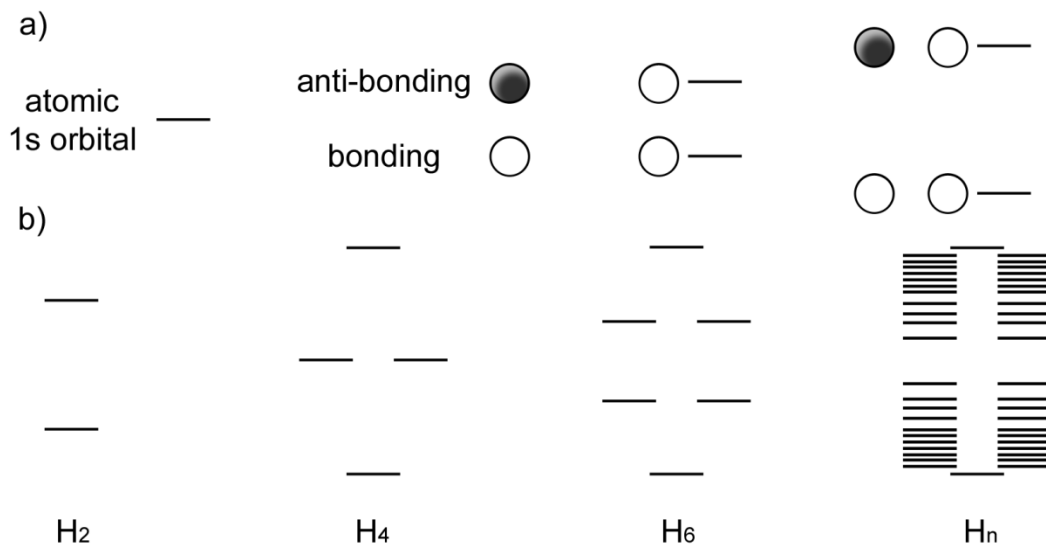


**Fig. 1.1** a) As orbital overlap increases the spacing between energy levels increases. b) Orbital energies for a chain of H atoms as the chain length increases (image adapted from Ref. 42)

The bonding of multiple hydrogen atoms provides a useful conceptual model, however the atoms that make-up quantum dots and all other solids have more complex electronic structure. For example, silicon has an electronic configuration of  $[\text{Ne}] 3s^2 3p^2$ . As is the case with all bonding, the core orbitals,  $1s^2 2s^2 2p^6$ , of Si can be neglected because these orbitals are close to the nucleus and experience little overlap with orbitals in neighbouring nuclei.<sup>43</sup> Since the overlap is so small the bands formed by core orbitals are very narrow.<sup>43</sup> The bands formed by the valence orbitals however, are wide and dominate the electronic structure.<sup>43</sup> In Si, the 3s and 3p orbitals overlap and form two distinct

bands.<sup>43,44</sup> The bands are separated by an energy range with no energy levels called the bandgap ( $E_g$ ).<sup>43,44</sup> A Si crystal with  $N$  atoms has  $2N$  orbitals forming the lower energy band or valence band (VB) and  $2N$  orbitals forming the higher energy band or the conduction band (CB).<sup>43</sup> Since each silicon atom has four valence electrons ( $3s^2 3p^2$ ) there will be  $4N$  electrons to fill the bands. According to the Aufbau and Pauli exclusion principles each energy level in the bands can hold up to two electrons. For Si, all  $4N$  electrons will fill the valence band while the conduction band remains empty at 0 K.<sup>43</sup> Not all elements separate into one filled band and one empty band as in Si. For example, solids of Group I or II elements behave differently. These solids have increased orbital overlap causing the formation of wide bands.<sup>43</sup> The small energy gap between  $ns$  and  $np$  orbitals causes these wide bands to overlap. In addition, Group I elements have only one electron thus the continuum will be partially filled.<sup>43</sup>

The conductivity of a solid is dependent on how full the band is, as well as the magnitude of the gap between a full band and an empty band.<sup>43-45</sup> For a solid to be conductive, there must be a net movement of electrons when a potential field is applied. This will only occur if the VB is not entirely full and the CB is not entirely empty. The size of the bandgap ( $E_g$ ) is a very important factor in determining whether a band is full, partially filled, or empty at room temperature.<sup>45</sup> In an insulator, the VB is filled and the CB is empty (Figure 1.2.a), therefore, when an electric field is applied there is no net movement of electrons and thus no conductivity. It is generally agreed that insulators have a bandgap higher than 4 eV.<sup>1</sup> With such a large gap, electrons cannot be thermally excited

from the VB to the CB. For a semiconductor, at 0 K the valence band is full and the conduction band is empty, just as in the case for an insulator.<sup>45</sup> However, since the bandgap in a semiconductor is smaller than in an insulator (i.e.,  $< 4$  eV), some electrons can populate the conduction band at temperatures higher than 0 K.<sup>1</sup> In fact, a small number of electrons that possess  $k_B T > E_g$  will populate the conduction band (Figure 1.2.b).<sup>45</sup> At any given moment, at room temperature, an electron is promoted from the VB to the CB leaving a vacancy in the VB. This vacancy is known as a hole, and it is a theoretical construct that represents the absence of an electron.<sup>45</sup> If an electric field is applied to a semiconductor, the small number of electrons and holes in the CB and VB, respectively are free to move through the empty states available, thus generating a current.<sup>45</sup> As the temperature increases, the number of electrons promoted also increases resulting in higher conductivities and this increase depends on the bandgap.<sup>43</sup> At any temperature the number of electrons promoted to the CB will increase for a solid with a smaller bandgap.<sup>43</sup> Lastly, the high conductivity of metals arises from two scenarios. In the first case (Figure 1.2.c), electrons in a metal occupy the CB (even at 0 K) and are free to move. In the second case (Figure 1.2.d), the VB and CB overlap and the electrons are also free to move about in the solid.

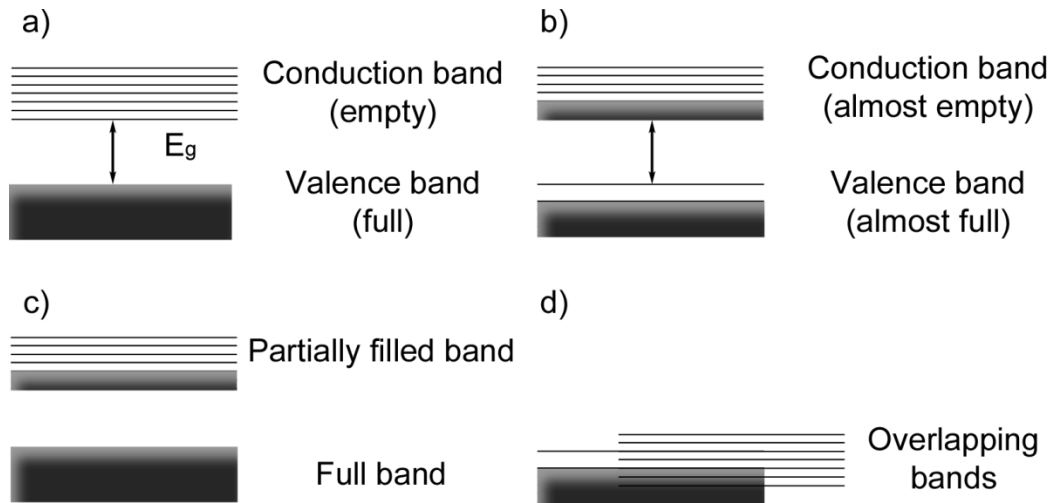


**Fig 1.2** A representation of the filled and empty bands in an a) insulator, b) semiconductor, and c,d) metal (image adapted from Ref. 31)

### 1.3.1. Direct and Indirect Bandgap semiconductors

The above description of electronic band structure (Section 1.3) fails to account for the varied optical properties of semiconductors. For example, GaAs emits light upon photoexcitation and has been used for laser diodes.<sup>46,47</sup> In addition, the absorption spectrum of GaAs shows a sharp decrease at the bandgap energy (1.42 eV ~ 870 nm, Figure 1.3).<sup>48</sup> In contrast, Si is essentially non-emissive in the bulk state and its absorption spectrum shows a gradual decrease along its bandgap (1.1 eV ~ 1060 nm, Figure 1.3). In addition, the lifetime of optically excited electrons in the CB is order of magnitudes shorter for GaAs than for Si.<sup>49,50</sup> To understand these observations it is necessary to examine the electronic structure of semiconductor in more detail.

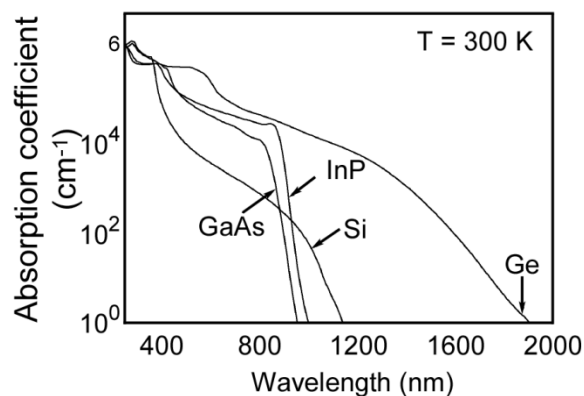


**Fig. 1.3** Absorption coefficients of common semiconductors. InP and GaAs show a sharp decrease in the absorption coefficient at the bandgap energies. Si and Ge show a gradual decrease (image adapted from Ref. 48)

In a molecule, electrons can be promoted to higher energy levels upon absorption of light of a suitable wavelength. The electron will only absorb photons with energy equal or higher than, the gap between the highest occupied (HOMO) and lowest unoccupied (LUMO) electronic levels. In addition to energy considerations, certain selection rules must be obeyed if the transition is to occur. In molecular species the spin of the electron cannot change (i.e.,  $\Delta s = 0$ ) and the angular momentum must change by one unit ( $\Delta l = \pm 1$ ).<sup>43</sup> These rules can be relaxed via coupling of the spin and orbital angular momenta. Following excitation, an electron can return to its ground state by emitting a photon (spontaneous emission).<sup>43</sup> It can also relax if a photon of the appropriate energy induces relaxation (stimulated emission).<sup>43</sup> The electron can also relax via non-radiative pathways such as vibronic coupling, or through atomic collisions where the excess energy is lost.<sup>43</sup>

In extended solids, such as semiconductors, the selection rules are slightly different. Radiation falling on a semiconductor will be absorbed by electrons in delocalized bands (generally those near the top of the valence band). Because of the many levels present over a small range of energies, the absorption band is broader than that observed for atomic spectra.<sup>43</sup> Light of wavelength matching the bandgap can be absorbed by a semiconductor and used to excite electrons from the VB to the CB (see Figure 1.3). Just as in molecules, transitions from the VB to the CB are governed by selection rules. The spin selection rule noted above still holds.<sup>43</sup> The orbital angular momentum rule in atoms is replaced by a restriction of the momentum of the electron wave ( $k$ ).<sup>43</sup> This rule states that an electron cannot change its momentum when it absorbs or emits radiation.<sup>43</sup> The electron can only be excited to energy levels with the same wave vector  $k$ . This is represented pictorially in Figure 1.4 in a plot of energy as a function of  $k$ . Only transitions that occur at the same value of  $k$  are allowed, conversely, any transitions that involve a change in momentum (i.e., ground and excited states occurring at different values of  $k$ ) are not allowed.<sup>1</sup> In a semiconductor, when an electron is excited from the top of the VB to the bottom the CB and both bands lie in the same  $k$  (Figure 1.4.a), the transition is allowed and the solid is said to be a direct bandgap semiconductor.<sup>1,43</sup> Transitions occurring between energy levels at the top of the VB and bottom of the CB that do not occur at the same  $k$  are not allowed because they violate the conservation of momentum selection rule.<sup>1,43</sup> Semiconductors of this type are called indirect bandgap semiconductors.<sup>1,43</sup> Excitation from VB to CB in an indirect bandgap material requires interaction

with the crystal in order to conserve momentum.<sup>45</sup> This interaction occurs via quantized lattice vibrations called phonons.<sup>43,45</sup> In essence, for an electron to be optically excited (or to relax) from the bottom (top) of the VB (CB) to the top (bottom) of the CB (VB) band, the excitation (emission) process must include a phonon. Transition of an electron from the CB to the VB only occurs when coupled to a phonon of the right energy to conserve momentum. Consequently, the probability of photon emission from an indirect bandgap semiconductor is lower than for a direct bandgap semiconductor.<sup>45</sup>

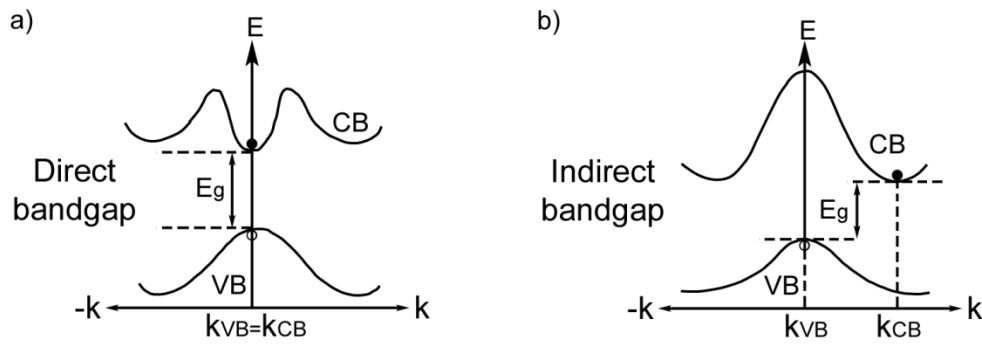


**Fig. 1.4** Pictorial representation of energy vs. momentum wave vector ( $k$ ) for a) a direct bandgap semiconductor and an b) indirect bandgap semiconductor. In a) the bottom of the CB and the top of the VB occur at the same value of  $k$ , in b) the values of  $k$  are different. (Image adapted from Ref. 1)

The conservation of momentum selection rule explains the differences noted above between a direct bandgap semiconductor (e.g., GaAs) and an indirect bandgap semiconductor (e.g., Si). GaAs, emits light efficiently because the transition is allowed (momentum is conserved).<sup>48</sup> Incident energy matching  $E_g$  of GaAs is directly absorbed (i.e. there is no need of a phonon) resulting in a sharp

decrease in the absorption coefficient in Figure 1.3.<sup>48</sup> Electron relaxation into the VB is fast because it does not need to be phonon mediated. These properties are in stark contrast with Si, a material that does not emit light appreciably due to the electronically forbidden (and weakly vibronically allowed by phonons) transition across the bandgap.<sup>48</sup> The gradual decrease in the absorption coefficient observed at the bandgap of Si (and Ge, another indirect bandgap semiconductor) occurs because all electronic transitions near  $E_g$  are weakly allowed via phonon coupling.<sup>22,48</sup> This produces a larger spread of energies at which absorption can occur. The excited state lifetime of Si is long because decay from CB to VB needs to be mediated by a phonon of the right energy. Since two events need to occur simultaneously for radiative recombination to take place, this process has decreased probability of occurring.<sup>48</sup> Due to the long excited state lifetimes of Si, electrons and holes can migrate across the bulk solid and recombine non-radiatively in trap states.

## **1.4. Size effects in semiconductor nanocrystals**

It was not until the early 1980s that the dimensionality of semiconductor particles was considered relevant when reporting their physical properties. Semiconductor particles with sizes lying in between a few nanometers and tens of nanometers show properties that deviate from the bulk significantly.<sup>22</sup> Section 1.1 described the changes observed in the thermodynamic, optical and electronic properties of CdS as the crystal size decreases to a few nm.<sup>22</sup> These effects are not exclusive to CdS; other semiconductor nanomaterials exhibit similar size dependent properties.<sup>21,51</sup> These changes can be attributed to: 1) the large fraction of surface atoms in a nanocrystals and 2) quantum size effects.<sup>22</sup>

The large fraction of surface atoms affects the thermodynamic properties of NCs. A detailed review of thermodynamic changes in the nanoregime has been published by Professor Paul Alivisatos.<sup>22</sup> Quantum size effects impact the intrinsic properties of the bands in a nanocrystal and as a result are responsible for changes in electronic and optical properties of QDs.

### **1.4.1. Quantum confinement in semiconductor nanocrystals**

Semiconductor nanocrystals with the same interior bonding geometry as the bulk, often exhibit unique size dependent optical properties.<sup>22</sup> These effects, known as quantum size effects, arise through changes in the density of energy levels that become appreciable in the nanosize regime. While bands are a continuum, the number of energy states at a given energy is not equal for all energies<sup>1,44,45</sup> A density of states (DOS) representation of semiconductors is

presented in Figure 1.5. On the one hand, bulk semiconductors (left of Figure 1.5.a) display large number of states located at the center of the band and fewer the band edges.<sup>52</sup> On the other hand, atoms possess discrete density of electronic states (right of Figure 1.5). Nanocrystals lie in between the atomic and molecular limit of quantized DOS and continuous bands (middle of Figure 1.5).<sup>22</sup>

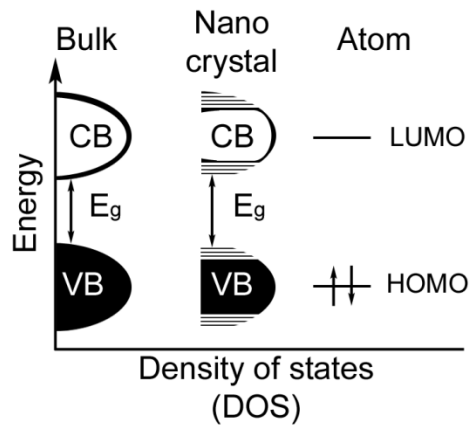


**Fig. 1.5** Density of states for a semiconductor. As crystal size decreases, discrete energy levels appear in the band structure (image adapted from Ref. 22)

In any material, there is a size below which the electrical and optical properties will start to change with dimension. This critical size depends on whether the solid is a metal or a semiconductor. In a semiconductor, the spacing between the band edges (the bandgap) is responsible for the optical and electrical behaviour of the solid.<sup>22</sup> In a solid, as particle size increases, the center of a band develops first and the band edges last. When a particle decreases in size the opposite occurs, i.e. the band edges are removed first (Figure 1.5).<sup>22</sup> At a critical size, semiconductor band edges start to disappear and become discrete.<sup>22</sup>

The formation of quantized energy states at the band edges affects the optical properties of the nanocrystals greatly. Decreasing crystal size results in an increased bandgap due to the removal of energy levels at the band edges (Figure 1.6a).<sup>22</sup> This causes a size dependence of the absorption and emission spectra. Figure 1.6.b shows the difference in the absorption spectra between CdS nanocrystals with diameters ranging from 48 nm to 6.4 nm. The spectra clearly show an increase in the band gap absorption energy as the crystal size decreases.<sup>53</sup> The bandgap of CdS QDs can be tuned over a range of 1.5 eV (Figure 1.6b).<sup>53</sup> In addition, QDs show an absorption peak such as those that occur between discrete energy levels (in contrast to bulk semiconductors, see Figure 1.3).

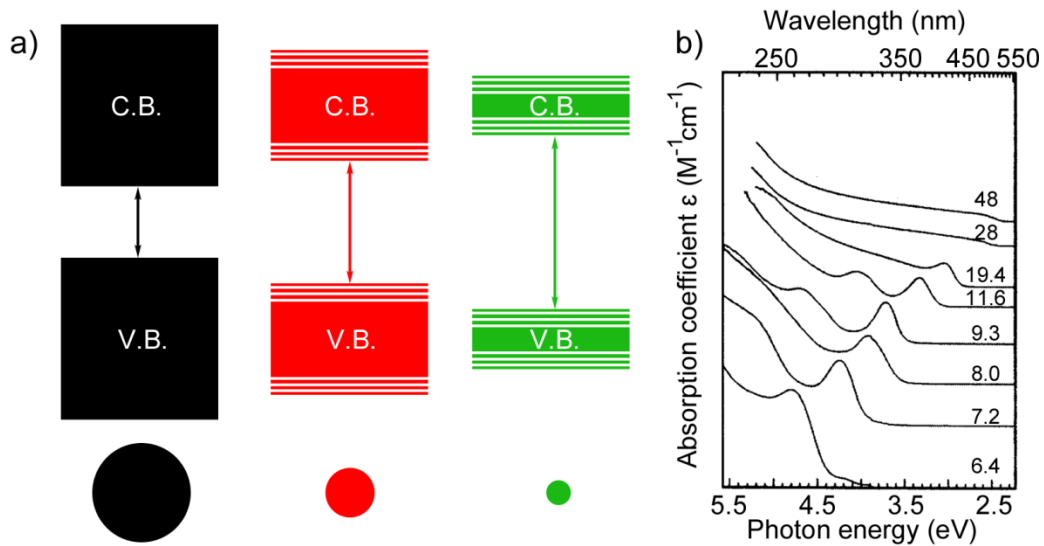


**Fig 1.6** a) Pictorial representation of the increased bandgap observed in semiconductor nanocrystals due to the erosion of the bands. b) Quantum confinement effects in the absorption of CdS quantum dots showing a shift in the absorption energy. The size in nm of the crystals is shown at the right of the absorption band. (Image adapted from Ref. 53)

The exciton binding energy is also influenced by particle size. Upon photoexcitation an electron is promoted across the bandgap, leaving a hole. These species can act as free carriers or as an electrically neutral, bound, quasi-particle referred to as an exciton.<sup>54</sup> If the binding energy between electrons and holes is small they will act as free carriers, if it is large they will form bound states.<sup>54</sup> The exciton binding energy is material dependent. For example, the binding energy is 27 meV for CdS or 4.9 meV for GaAs in the bulk.<sup>54</sup> Free carriers are common in bulk materials because the wavefunctions of electrons and holes are spread over an almost infinite number of atoms. The physical distance between an electron and hole in the bulk is known as the Bohr exciton radius. The Bohr exciton radius  $r_B^{ex}$  can be expressed by (1):

$$r_B^{ex} = \frac{\epsilon r_B m_0 \left[1 + \frac{m_e}{m_h}\right]}{\epsilon_0 m_e} \quad (1)$$

Where  $\epsilon$  is the dielectric constant of the material,  $r_B$  is the Bohr radius in hydrogen,  $m_0$  is the mass of a free electron,  $m_e$  and  $m_h$  are the effective masses of electron and hole respectively and  $\epsilon_0$  is the dielectric constant of free space.<sup>55</sup> When the electron and a hole are confined in a particle whose dimension approaches the size of the Bohr exciton radius, the coulombic forces between them increases and so does the binding energy.<sup>56</sup> The increased binding energy in nanomaterials is responsible for increased radiative rates leading to decreased lifetimes of electrons in the excited state.

## 1.5. Silicon Nanocrystals

Silicon nanocrystals (Si-NCs) are of great interest due to their size-tunable luminescence and their expected low toxicity (as opposed to Cd based QD nanocrystals).<sup>34,57</sup> Red luminescence from silicon nanostructures was first reported by Canham 1990.<sup>58</sup> This was a remarkable observation given crystalline, diamond lattice silicon is an indirect gap semiconductor. The red luminescence was attributed to quantum confinement within nanosize Si crystallites in the pillars formed by anodic etching of silicon substrates.<sup>59</sup> This discovery initiated a revolution in the field of Si-based photonics. The technological interest in these materials is immense, as a result of the potential of bridging digital computing (silicon based microelectronics) and digital communication (silica based fibre optics).<sup>60</sup> Si-based photonics is expected to fill a void between these two powerful technologies.

It is well established that as the dimensions of Si approach the radius of an exciton in the bulk material (ca. 5 nm for Si), the band gap energy increases and the band edges become discrete and photoluminescence (PL) occurs.<sup>61</sup> The band structure of nanosized Si crystals varies with size. Very small Si-NCs (i.e.,  $d < 2$  nm) have been reported to exhibit a direct bandgap.<sup>62</sup> In addition, de Boer *et al.* reported a fast transition between the bottom of the CB and top of the VB attributed to no-phonon, radiative recombination of hot-carriers that increases in intensity with decreasing crystallite size.<sup>63</sup> This observation suggests the NCs transition from indirect bandgap to direct bandgap semiconductors at sizes near 2 nm.

It is well established that in Si crystals with diameters larger than 2 nm the bandgap transition remains indirect.<sup>64</sup> This leads to the question: what makes Si-NCs of these dimensions luminesce? It has been proposed that in nanometer sized Si crystals the bandgap transition becomes weakly dipole-allowed.<sup>65</sup> As size decreases the electronic states become localized within the NC and the momentum distribution spreads as a result of the Heisenberg uncertainty principle (small  $\Delta x$ , high  $\Delta p$ ).<sup>65</sup> Thus, the momentum conservation law is not violated in this case, which yields a nonzero probability of a radiative transition between different values of  $k$  ( $k_{VB} \neq k_{CB}$ ) even without phonon coupling.<sup>65</sup>

In bulk crystalline Si, optical absorption generally occurs via a transverse optic (TO) phonon occurring at  $458 \text{ cm}^{-1}$ .<sup>66</sup> Upon excitation, radiative and non-radiative electron-hole recombinations are slow and often mediated by defect or trap states which increase electron phonon coupling.<sup>66</sup> Compared to bulk silicon, NC silicon can be rendered optically active due to: 1) increased vibronic interactions,<sup>66,67</sup> 2) the high exciton binding energy preventing non-radiative electron hole recombination in defects,<sup>66</sup> 3) decreased probability of defects,<sup>64,68</sup> 4) decreased Auger recombination.<sup>64</sup> The increased vibronic interactions lead to reduced luminescence lifetime from  $10^{-4}$  to  $10^{-6}$  s when the crystal size decreases from 4 nm to 1.5 nm.<sup>66</sup> The high exciton binding energy in NCs prevents dissociation of the electron and hole at room temperature.<sup>66</sup> In addition, non-radiative recombination rates are diminished in the nanoregime because NCs lack the high density of crystallographic imperfections.<sup>64,68</sup> Defects present as the NCs are being formed can migrate to the surface, where they can be eliminated via

surface reconstruction during processing.<sup>68</sup> Lastly, in the bulk, when the electron-hole density is high, excitons can recombine via Auger recombination. In a nanocrystal, the generation of multiple electron hole pairs is unlikely due to their small size, thus Auger recombination is strongly suppressed.<sup>64</sup> These combined effects (fewer defects and suppressed carrier migration) decrease the probability of non-radiative recombination.<sup>66</sup>

### **1.5.1. Optical properties of Si-NCs**

It is important to study the different mechanisms that can give rise to light emission from Si-NCs. An exciton, formed by coulombic interaction between electron and hole can recombine emitting a photon (Figure 1.7.a,b).<sup>69</sup> In this case, the emitted photon has energy close to that of the bandgap.<sup>68</sup> This emission can be modified by tailoring the NC bandgap by changing the NC size. A common method to control particle size is via HF-etching (Figure 1.7.a).<sup>70,71</sup> Luminescence from Si NCs can also be influenced by surface defects (Figure 1.7.c). One important example has been proposed by Wolkin et al. where Si=O species are proposed to be responsible for red luminescence in small crystallites.<sup>68,72</sup> Figure 1.7.d highlights a third mechanism of light emission arising from photoexcitation of Si-NCs in which energy is transferred from the Si-NC to a luminescent center that can be located several angstroms or nanometers away. The most relevant example is that of Er<sup>3+</sup> ions in SiO<sub>2</sub> located in close proximity to a NC.

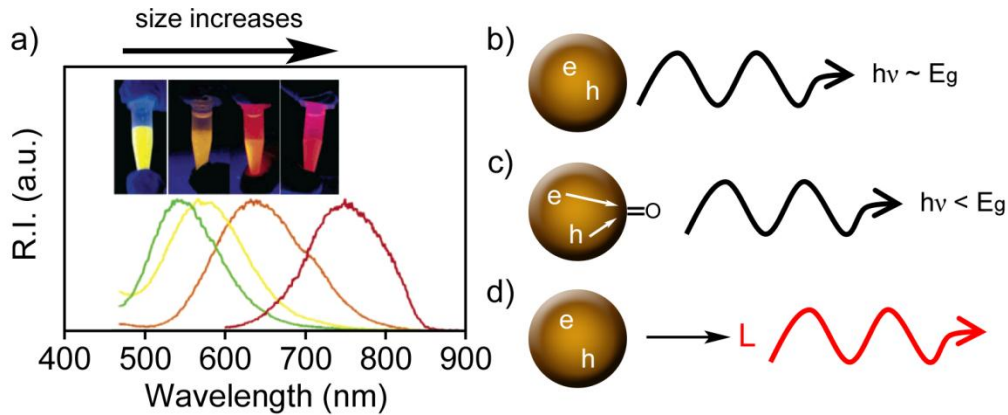


**Fig. 1.7** a) PL spectra of HF etched silicon nanocrystals spanning the visible range. b) Mechanisms of light emission (image adapted from Ref. 68 and Ref. 71)

In addition, the optical properties of Si-NCs can also be affected by carrier tunneling or by Förster energy transfer (FRET) occurring between two nanocrystals in close proximity. Computational studies have demonstrated that tunnelling can occur at distances of less than 2 nm while FRET occurs at distances of 5 nm or more.<sup>65</sup>

#### 1.5.1.1. Erbium Sensitization using oxide-embedded Si-NCs (OE-Si-NCs)

Er-doped materials are of great interest in optical communications technology.<sup>73-75</sup> They are routinely used as the gain medium in lasers and optical amplifiers operating at the standard telecommunications wavelength of 1.5  $\mu\text{m}$ .<sup>76</sup> The transition of  $\text{Er}^{3+}$  ions from the first excited state to the ground state ( ${}^4\text{I}_{13/2}$  to  ${}^4\text{I}_{15/2}$ ) occurs at 1.54  $\mu\text{m}$  which lies in the low-loss window of silica fiber optics.<sup>75</sup>

For this reason,  $\text{Er}^{3+}$  ions are currently employed in fiber amplifiers in long-distance telecommunication links worldwide.<sup>77</sup>

The transition of interest occurs between two  $f$ -orbitals and is thus Laporte forbidden ( $\Delta l \neq \pm 1$ ), for this reason the absorption cross-section is low.<sup>78</sup> To overcome this issue, amplifiers are doped with high concentrations of Er and pumped using high powers.<sup>78</sup> This approach can give rise to two different issues, namely upconversion and excited state absorption.<sup>79,80</sup> These processes decrease the efficiency of Er emission especially under the high pumping powers required to excite electrons through a Laporte forbidden transition.

To circumvent these issues,  $\text{Er}^{3+}$  ions can be excited using an energy transfer process.<sup>81</sup> In this approach a sensitizer coupled to an  $\text{Er}^{3+}$  ion absorbs light and then transfers its energy to Er.<sup>81</sup> This results in an effective increase of the absorption cross-section. If the absorption spectrum of the sensitizer is broad, low power white light LEDs may be used as pumping sources.<sup>81</sup> OE-Si-NCs have been proposed as erbium sensitizers.<sup>82</sup> OE-Si-NCs have an absorption cross section about four orders of magnitude higher than  $\text{Er}^{3+}$  and unlike organic sensitizers they do not degrade in the presence of light.<sup>81</sup> For the aforementioned reasons, and bearing in mind the broad absorption spectrum of Si-NCs, white-light or LED sources have been used to excite Si-NC sensitized rare earth  $\text{Er}^{3+}$  ions.<sup>81</sup>

Fujii *et al.* were the first to report that the presence of Si-NCs in Er-doped  $\text{SiO}_2$ , prepared via r.f. cosputtering, considerably enhances the effective Er

absorption cross section.<sup>82</sup> This observation was later confirmed by other groups using other methods to prepare OE-Si-NCs with Er ions.<sup>83-86</sup> The evidence strongly suggests energy is transferred from Si-NCs to Er ions via a Förster process (FRET).<sup>87,88</sup> In this mechanism, a photon is absorbed by the NC creating an exciton which can non-radiatively recombine thereby exciting nearby Er ions.<sup>78,82</sup> In addition, as the concentration of Er<sup>3+</sup> increases the PL intensity of quantum confined Si-NCs decreases, while the Er characteristic PL increases (as expected for a FRET process).<sup>89</sup> In other words, the NC becomes dark if it is coupled to an Er<sup>3+</sup> ion. At very high Er ion concentrations, upconversion (one ion in the excited state relaxes non-radiatively, thereby exciting a nearby ion to a higher energy state) is observed in the form of a sharp feature at 980 nm.<sup>89</sup> Some studies of the excitation rate per ion show that one NC can excite only one or two Er ions, resulting in a maximum excitable Er concentration of 0.02 – 0.04 at.% Er.<sup>89</sup> This concentration limit may be an intrinsic property of Si-NC sensitized erbium luminescence. The amount of excitable Er can be strongly affected by the higher excitation efficiency in a sensitized system. This behaviour can be explained by 1) Auger de-excitation processes occurring between the NC and an excited Er ion or by 2) cooperative upconversion occurring due to the higher probability of finding excited ions in a sensitized system.<sup>90</sup>

#### **1.5.1.2. Homogeneous and Inhomogeneous broadening**

A typical Si-NC photoluminescence spectrum is characterized by a broad fluorescence band.<sup>57,65</sup> The breadth of the luminescence is interesting from a

fundamental point of view and for the development of optoelectronic applications.<sup>91</sup>

Peak broadening arises from two factors: 1) homogeneous broadening and 2) inhomogeneous broadening.<sup>65,92,93</sup> For homogeneous broadening, the mechanism that causes broadening has the same effect on each nanocrystal.<sup>92,93</sup> For inhomogeneous broadening, the emission wavelength (or energy) changes for each NC.<sup>93</sup> Typically, oxide embedded silicon nanocrystals have a PL maxima in the range of 800 – 900 nm with a full-width-at-half-maximum (FWHM) of approximately 200 nm (250 – 275 meV).<sup>65</sup> This breadth arises from homogeneous and inhomogeneous broadening.

A study on “single Si-NC” luminescence by Valenta et al. reports a FWHM of almost 150 meV at room temperature.<sup>94</sup> This significant breadth is due to homogeneous broadening of Si-NCs.

Often, the main source of broadening in an ensemble of nanocrystals is due to the size distribution.<sup>92</sup> This form of inhomogeneous broadening arises from the principle that each NC has a bandgap dependent on its size.<sup>65</sup> Particle shape or defects can contribute to increasing breadth of the PL (inhomogeneous) and thus must be carefully controlled during synthesis.<sup>22</sup> For this reason, methods to synthesize nanocrystals with narrow size distribution are pivotal in the field of silicon photonics.<sup>91</sup>

## **1.5.2. Methods to prepare Silicon Nanocrystals**

Since the early 90s many methods to prepare Si-NCs have been reported in the literature. These methods can be divided into physical and chemical.

### **1.5.2.1. Physical Methods for preparing Si-NCs**

Ion implantation uses energetic ions (accelerated using an electrical field) and implants them into a host substrate.<sup>95</sup> The implanted ions can reach depths of a few hundreds of nanometers into the host material.<sup>95</sup> Nanoparticles are then formed by annealing and in some cases further ion irradiation.<sup>95,96</sup> Ion implantation is a commercially established technique used to dope silicon wafers and thus can be of industrial interest. The first synthesis of Si-NCs using ion implantation came from Japanese researchers in the early 1990s.<sup>96</sup> The resulting material showed characteristic red luminescence from Si-NCs in a silica matrix. Erbium sensitization was also demonstrated in films prepared by ion implantation of Er and Si.<sup>84,85</sup> Samples prepared via ion implantation are generally annealed under slightly reducing conditions to crystallize the resulting Si nanoparticles and to cure defects present from the implantation process.<sup>96</sup> The size distribution of ion implanted materials varies with depth. Smaller particles are routinely found near the edges of the implant profile due to the smaller concentration of implanted ions in these areas.<sup>96</sup>

Other common physical techniques to prepare silicon nanocrystals are vacuum evaporation, laser ablation, or magnetron sputtering to name a few. In vacuum evaporation, a thin layer of  $\text{SiO}_x$  ( $1 \leq x \leq 2$ ) is deposited on a heated

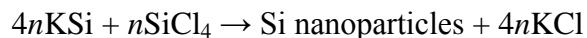
substrate via thermal evaporation under high vacuum.<sup>97</sup> Films are heated to 1000 °C to produce Si-NCs in an oxide matrix. Size is controlled by using small amounts of oxygen gas during film evaporation (more oxygen results in smaller crystals and higher PL energy).<sup>97</sup>

To prepare Si-NCs using laser ablation a Si target is ablated by a pulsed laser under reduced pressure in an inert atmosphere.<sup>98,99</sup> Films exhibiting photo and electroluminescence have been prepared using this method.<sup>98,99</sup> Reactive magnetron sputtering of SiO<sub>2</sub> accompanied by *in-situ* reduction using a mixture of argon and hydrogen and plasma has been utilized to make silicon rich layers on substrates.<sup>100</sup> As in vacuum evaporation, precipitation of silicon crystallites is brought about by heating the substrates to 1100 °C.<sup>100</sup> The aforementioned techniques constitute some of the physical methods utilized to make Si-NCs. Although these techniques have been central in helping understand the optical properties of Si-NCs, they can be costly and yield only small quantities of nanocrystals on a substrate.

#### **1.5.2.2. Chemical methods for preparing Si-NCs**

Chemical methods used to synthesize nanocrystals (e.g., reduction of silicon precursors) can produce larger quantities (ranging from milligrams to grams) of materials than the aforementioned physical methods. In these methods, care must be taken to reduce impurities during synthesis which may yield unexpected optical properties. The Kauzlarich group has reported two low

temperature syntheses of colloidal nanocrystals.<sup>101</sup> The first report used Zintl salts to reduce SiCl<sub>4</sub> as shown below:



This method produced particles in low-yield exhibiting lattice fringes in HRTEM analysis corresponding to <111> Si planes.<sup>101</sup> A second method involved reaction of a silicon Zintl salt with ammonium bromide and is suspected to occur via chemical metathesis.<sup>102</sup> Hydride-terminated Si-NCs were formed by reduction with one of the many byproducts (NH<sub>3</sub>, H<sub>2</sub>, and NaBr). Kauzlarich et al. also functionalized the surface of the Si-NCs with octyl groups. The particles obtained are 3 ± 1 nm in diameter (TEM), and their PL varies with excitation wavelength peaking at 438 nm (λ<sub>EX</sub> = 380 nm).<sup>102</sup> Interestingly, the absorption spectra shows a clear narrow peak centered at 275 nm.<sup>102</sup> It is unlikely a sharp absorption of this type would arise from indirect bandgap Si-NCs of the reported diameter (*vide supra*).

The methods described above are only a handful of examples of the many physical and chemical techniques developed in the last 20 years to synthesize silicon nanocrystals.<sup>103</sup> Other methods rely on precursor thermolysis, such as pyrolysis of silanes using laser radiation which was reported by the Swihart group.<sup>70</sup> This high-throughput method produces Si-NCs at rates ranging between 20-200 mg/h. The size and PL of the nanocrystals can be controlled via HF-etching. Another example of precursor thermolysis was presented by Korgel et al.

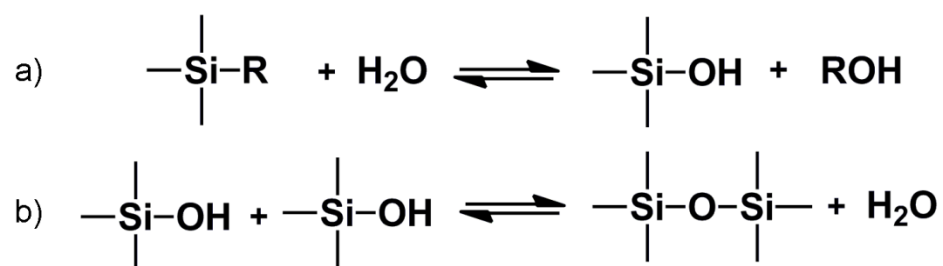
by thermal treatment of diphenylsilane in supercritical solvent mixtures.<sup>104</sup> The particles display strong luminescence attributed to quantum confined carriers.

Physical methods such as vacuum evaporation and magnetron sputtering form nanocrystals by thermal treatment of silicon rich layers. Silicon rich oxides (SROs) can also be procured synthetically. Upon thermal treatment, SROs can yield Si-NCs in an oxide matrix.<sup>105</sup> Thermolysis of SROs is a powerful technique that can yield high quantities or thin films of luminescent OE-Si-NCs.<sup>105</sup>

### **1.5.2.3. Synthesis and thermolysis of Sol-gel Derived Silicon rich oxides**

An important method to produce OE-Si-NCs is by the formation of substoichiometric silica precursors with a large excess of Si. Thermal processing of these materials leads to phase separation between SiO<sub>2</sub> and Si.<sup>105</sup> At temperatures higher than 1000 °C the silicon domains crystallize to form Si-NCs.<sup>106</sup> Most synthetic methods use slightly reducing conditions to passivate defects during thermal processing.<sup>107</sup> Synthesis of SROs has been routinely performed using sol-gel chemistry to yield silsesquioxanes with an empirical formula RSiO<sub>1.5</sub> where R can be a hydride or an organic functional group.<sup>105</sup> A sol is a stable colloidal suspension in contrast with a gel consisting of a three-dimensional continuous solid network.<sup>108</sup> This soft-chemical approach creates an oxide network by polycondensation reactions of molecular precursors and can be mechanistically described in terms of hydrolysis and condensation reactions.<sup>105</sup> During hydrolysis, the substituents of the molecular silicon precursor are replaced by hydroxyl groups in the presence of water (Scheme 1.1).<sup>108</sup> Under the

appropriate conditions, condensation ensues between two hydrolyzed molecules, yielding a polymer with a Si-O-Si backbone.<sup>108</sup> The rates of hydrolysis and condensation are dependent on many factors such as the nature of the substituents (R), the ratio of alcohol to water used, the kind of solvent, temperature, the concentration of the precursor mixtures and the pH.<sup>108</sup> Since these variables affect the SRO obtained, they will also influence the resulting OE-Si-NC composite resulting from thermal treatment.<sup>109</sup>

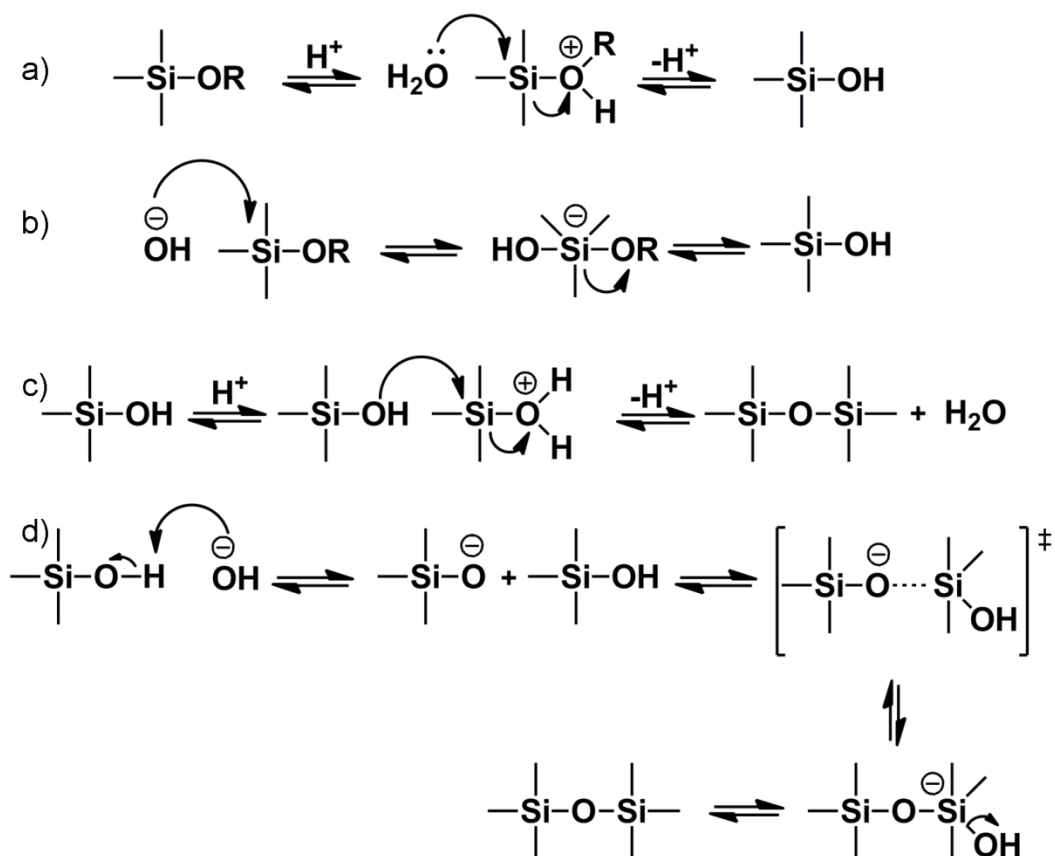


**Scheme 1.1.** a) Hydrolysis and b) condensation reactions of molecular silicon precursors.<sup>108,110</sup>

The versatility of the sol-gel synthetic approach is highlighted by the work of Soraru et al. and Das et al.<sup>111,112</sup> These two reports use triethoxysilane as a molecular precursor producing either a solid gel or a solution processable sol by changing the reaction temperature and aging conditions.

The pH also affects the morphology of the resulting polymer. Under acidic conditions the condensed polymer gel is linear, under basic conditions the polymer is branched.<sup>110</sup> This can be explained by studying the sol-gel mechanisms under the two different conditions. Hydrolysis under acidic (Scheme 1.2.a) or basic (Scheme 1.2.b) conditions occurs via a S<sub>N</sub>2 mechanism.<sup>110</sup> The

condensation step is what controls the morphology of the resulting polymer. As can be seen from the condensation mechanism under acidic conditions (Scheme 1.2.c), the reaction is favoured at terminal silicon atoms. The condensation mechanism under basic conditions is expected to occur via a stable 5-coordinate intermediate (Scheme 1.2.d) with a negative charge on the silicon atom.<sup>110</sup> For this reason, condensation is more likely to occur in central Si atoms to inductively stabilize the negative charge during condensation.<sup>110</sup>



**Scheme 1.2** Mechanism of hydrolysis under a) acidic and b) basic conditions. Mechanism of condensation under c) acid and d) basic conditions.<sup>108,110</sup>

Sols and gels derived from hydrolysis and condensation of triethoxysilane precursors can be thermally treated to obtain OE-Si-NCs.<sup>111,112</sup> Sols are routinely prepared at low temperatures and can be spin coated into thin films.<sup>112</sup> Gels generally require aging and solvent removal steps before thermal treatment.<sup>111</sup> Thin films and gels heated to 1000 °C or higher yield OE-Si-NCs displaying the characteristic red PL upon laser irradiation.<sup>111,112</sup> Gels derived from hydrolysis and condensation of trichlorosilane also yield OE-Si-NCs upon thermal processing at 1100 °C.<sup>109</sup>

Another SRO of great importance in the synthesis of OE-Si-NCs is hydrogen silsesquioxane (HSQ).<sup>71,105</sup> HSQ ( $H_8Si_8O_{12}$ , Figure 1.8.a) was first synthesized by Frye and Collins by scarce water addition of trichlorosilane.<sup>113</sup> Currently, HSQ is used as a spin-on dielectric for microelectronics applications.<sup>114</sup> HSQ is sold by Dow Corning Corporation dissolved in methyl isobutylketone (MIBK). When HSQ is heated to temperatures ranging from 1100 °C – 1400 °C under slightly reducing conditions (5%  $H_2$  in 95% Ar or  $N_2$ ) it produces OE-Si-NC.<sup>71</sup> The nanocrystal formation process from HSQ can be divided into three temperature regimes: 1) <400 °C, 2) 500°C – 900°C, 3) >900 °C.<sup>115</sup> Rearrangement of the cage structure occurs in 1). The second regime is characterized by thermal cleavage of the Si-H bonds and disproportionation. Non-crystalline Si nanodomains are formed in this temperature range. The last regime is characterized by crystallization and growth of NCs. It has been shown HSQ-derived OE-Si-NC composites contain elemental silicon (XPS) with crystalline reflections corresponding to the diamond lattice of Si (XRD).<sup>61,71</sup> The optical

properties of the oxide-embedded material are characterized by a broad luminescence spanning the red and near-IR (Figure 1.7.a and 1.8.b).<sup>71,116</sup> The luminescence of oxide-embedded and free standing Si-NCs has been attributed to quantum confined carriers.<sup>61</sup> Heating to higher temperatures produces larger NCs that luminesce closer to the bulk bandgap energy.<sup>71</sup> The silica matrix can be removed by exposure to an etching mixture composed of hydrofluoric acid, ethanol and water yielding FS-Si-NCs.<sup>71</sup> The size of the FS-Si-NCs can be controlled by further exposure to the etching mixture yielding NCs with optical luminescence spanning the visible range from red to green (Figure 1.7.a inset). In order to improve solution-stability, FS-Si-NCs can be functionalized with polar or non-polar groups via hydrosilylation.<sup>117,118</sup> Thin films of OE-Si-NCs can be prepared by spin coating a solution of HSQ on any substrate that can stand the heating conditions. In addition, HSQ can be used to pattern OE-Si-NCs on a substrate using e-beam lithography (Figure 1.8.b).<sup>116</sup>

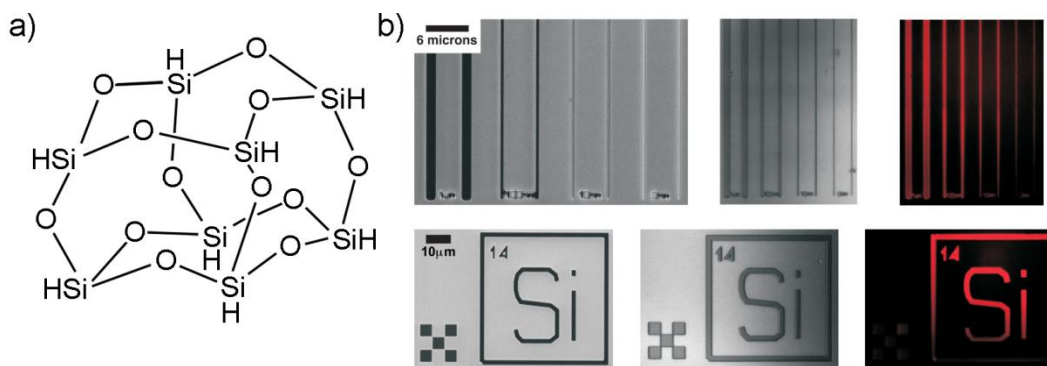


**Fig. 1.8** a) Structure of commercially available HSQ. b) Patterning of OE-Si-NCs via e-beam lithography of HSQ. The images on the far right show the characteristic red PL after photoexcitation (Image adapted from Ref. 116)

## 1.6. Thesis outline

The optical properties of OE-Si-NCs are characterized by a broad luminescence arising from recombination of carriers inside the NC. Luminescence can be affected by homogeneous and inhomogeneous broadening width. Although luminescence from Si, an indirect bandgap semiconductor, is interesting in its own right, a narrower emission profile could lead to many new applications. For example, lasing or sensing applications will benefit greatly from narrower emission profiles.<sup>119,120</sup> Additionally, biological tagging can be more versatile if the luminescence from different markers does not overlap in the emission spectrum. The most intuitive method to narrow the luminescence bandwidth is by decreasing the NC size distribution. Other less intuitive methods include coupling the emission of NCs to optical cavities or to use of NCs as sensitizers for species possessing narrow luminescence profile.

The most common example of sensitization uses trivalent erbium ions in a silica matrix containing silicon nanocrystals. Sensitization of Er emission will be described in Chapter two of this thesis. The *intra-f* transition between the first excited state and the ground state of  $\text{Er}^{3+}$  ions lies in the low-loss window of silica fiber optics and is of importance for telecommunication applications. This transition is Laporte forbidden, resulting in a very low absorption cross-section. To address this challenge Si-NCs can be used to sensitize emission from erbium ion emission. In this process, photoexcitation causes the formation of an exciton in the NC that relaxes non-radiatively using the recombination energy to excite a neighbouring  $\text{Er}^{3+}$  ion. This process increases the effective absorption cross-

section of  $\text{Er}^{3+}$  ions by at least 3 orders of magnitude. Chapter two outlines a method to prepare OE-Si-NCs with trivalent  $\text{Er}^{3+}$  ions in the matrix.

Chapter three reports a method to pattern oxide-embedded Silicon nanoparticles (OE-Si-NPs) using diblock copolymer templates (namely polystyrene-*b*-poly-4-vinylpyridine). This method forms nanodiscs on silicon and silica surfaces. Patterning is believed to occur via base catalyzed gelation of HSQ molecules in the amine moieties of the block copolymer. The disc-to-disc spacing and disc diameter can be modified by altering the molecular weights of the diblock copolymer units. Controlling disc size provides a means to manipulate the number of particles in a disc. This technique may provide a means to improve size distribution. In addition a structure of this type may be important to study particle-particle interactions. The method was extended to pattern Ge nanostructures using tetraethoxygermane as a precursor.

In order to narrow the luminescence spectrum by narrowing the size distribution, a photo-assisted etching method was developed. Chapter four describes this method in detail. During the etching process, an exciton is formed in the NC via light irradiation. If the hole migrates to the NC surface, a Si surface atom will become polarized and will be susceptible to nucleophilic attack by hydrofluoric acid. Only NCs where an exciton is formed will be etched. As the NC size decreases its bandgap increases, consequently, the irradiation energy needed to produce an exciton will also increase. Based upon this principle, if a population of NCs is irradiated with light of wavelength  $\lambda$  during etching, only

NCs with a bandgap corresponding to  $\lambda$  will be etched. This method is expected to narrow the luminescence profile by decreasing inhomogeneous broadening.

Another method to decrease the broad luminescence profile is by coupling the NC emission to an optical cavity. A method to place NCs in cylindrical cavities (i.e., capillaries and fiber optics) is described in Chapter five. Coupling causes the broad luminescence from Si-NCs to develop sharp peaks superimposed over the broad PL profile. The sharp peaks correspond to Si-NC energies that are resonant with the microcavity. The confined photons show minimal losses as they circulate through the cavity. A proof-of-concept sensor was designed using Si-NCs coupled to a fiber optic which takes advantage of the sharp peaks now present in the PL spectrum. A more elaborate DNA sensor that is both sensitive and selective may be developed from the NC-fiber optic architecture. Preliminary studies on a method to functionalize the NC films with DNA for sensing applications will be reported in Appendix A.

Lastly, conclusions regarding the presented work, and future directions that may be pursued is presented in Chapter six.

## 1.7. References

- (1) Fahlman, B. *Materials Chemistry*; Springer: Dordrecht, Netherlands, 2007.
- (2) ACS; ACS; Vol. 2011.
- (3) Cao Guozhong; Wang, Y. *Nanostructures and nanomaterials: synthesis, properties, and applications*; World Scientific Publishing, Co. Pte. Ltd.: Singapore, 2011.
- (4) Shapira, P.; Wang, J. *Nature* **2010**, *468*, 627.
- (5) Service, R. F. *Science* **2004**, *304*, 1732.
- (6) Hersam, M. *ACS Nano* **2011**, *5*, 1.
- (7) Leydesdorff, L. *Scientometrics* **2008**, *76*, 159.
- (8) Yu, G.; Wang, M. Y.; Yu, D. R. *Scientometrics* **2010**, *84*, 81.
- (9) Vol. 2011.
- (10) Simeon, T.; Aikens, C. M.; Tejerina, B.; Schatz, G. C. *J. Chem. Educ.* **2011**, *88*, 1079.
- (11) Balasubramanian, G.; Lohani, V. K.; Puri, I. K.; Case, S. W.; Mahajan, R. L. *Int. J. Eng. Educ.* **2011**, *27*, 333.
- (12) Russo, D.; Fagan, R. D.; Hesjedal, T. *IEEE T. Educ.* **2011**, *54*, 428.
- (13) Oberdörster, G.; Oberdörster, E.; Oberdörster, J. *Environ. Health Perspect.* **2005**, *113*, 823.
- (14) Nel, A.; Xia, T.; Mädler, L.; Li, N. *Science* **2006**, *311*, 622.
- (15) Shields, A. J. *Nat. Photonics* **2007**, *1*, 215.
- (16) Michalet, X.; Pinaud, F. F.; Bentolila, L. A.; Tsay, J. M.; Doose, S.; Li, J. J.; Sundaresan, G.; Wu, A. M.; Gambhir, S. S.; Weiss, S. *Science* **2005**, *307*, 538.
- (17) Chan, W. C. W.; Maxwell, D. J.; Gao, X.; Bailey, R. E.; Han, M.; Nie, S. *Curr. Opin. Biotechnol.* **2002**, *13*, 40.
- (18) Brus, L. E. *J. Chem. Phys.* **1983**, *79*, 5566.
- (19) Brus, L. E. *J. Chem. Phys.* **1984**, *80*, 4403.
- (20) Rossetti, R.; Nakahara, S.; Brus, L. E. *J. Chem. Phys.* **1983**, *79*, 1086.
- (21) Burda, C.; Chen, X.; Narayanan, R.; El-Sayed, M. A. *Chem. Rev.* **2005**, *105*, 1025.
- (22) Alivisatos, A. P. *J. Phys. Chem.* **1996**, *100*, 13226.
- (23) Wang, Y.; Herron, N. *J. Phys. Chem.* **1991**, *95*, 525.
- (24) Dabbousi, B. O.; Rodriguez-Viejo, J.; Mikulec, F. V.; Heine, J. R.; Mattoussi, H.; Ober, R.; Jensen, K. F.; Bawendi, M. G. *J. Phys. Chem. B* **1997**, *101*, 9463.
- (25) Durose, K.; Fellows, A. T.; Brinkman, A. W.; Russell, G. J.; Woods, J. *J. Mater. Sci.* **1985**, *20*, 3783.
- (26) Tan, G. L.; Liu, R. H. *J. Nanopart. Res.* **2010**, *12*, 605.
- (27) Heintz, A. S.; Fink, M. J.; Mitchell, B. S. *Adv. Mater.* **2007**, *19*, 3984.
- (28) Bawa, R. *Nanotechnology Law and Business* **2008**, *5*, 135.
- (29) Hardman, R. *Environ. Health Perspect.* **2006**, *114*, 165.

- (30) Deaves, M. *Manuf. Eng.* **2004**, 83, 12.
- (31) Sinha, P.; Kriegner, C. J.; Schew, W. A.; Kaczmar, S. W.; Traister, M.; Wilson, D. J. *Energy Policy* **2008**, 36, 381.
- (32) Nagesha, D. K.; Whitehead, M. A.; Coffey, J. L. *Adv. Mater.* **2005**, 17, 921.
- (33) Park, J. H.; Gu, L.; Von Maltzahn, G.; Ruoslahti, E.; Bhatia, S. N.; Sailor, M. J. *Nat. Mater.* **2009**, 8, 331.
- (34) Erogbogbo, F.; Yong, K. T.; Roy, I.; Xu, G. X.; Prasad, P. N.; Swihart, M. T. *ACS Nano* **2008**, 2, 873.
- (35) Alsharif, N. H.; Berger, C. E. M.; Varanasi, S. S.; Chao, Y.; Horrocks, B. R.; Datta, H. K. *Small* **2009**, 5, 221.
- (36) Ruizendaal, L.; Bhattacharjee, S.; Pournazari, K.; Rosso-Vasic, M.; De Haan, L. H. J.; Alink, G. M.; Marcelis, A. T. M.; Zuilhof, H. *Nanotoxicology* **2009**, 3, 339.
- (37) Carlisle, E. M. *Sci. Total Environ.* **1988**, 73, 95.
- (38) Anglin, E. J.; Cheng, L.; Freeman, W. R.; Sailor, M. J. *Adv. Drug. Deliv. Rev.* **2008**, 60, 1266.
- (39) *Biomedical Materials* **2006**, 6.
- (40) Miura, S.; Nakamura, T.; Fujii, M.; Inui, M.; Hayashi, S. *Phys. Rev. B* **2006**, 73.
- (41) Talapin, D. V.; Rogach, A. L.; Kornowski, A.; Haase, M.; Weller, H. *Nano Lett.* **2001**, 1, 207.
- (42) Hoffmann, R. *Angew. Chem. Int. Edit.* **1987**, 26, 846.
- (43) Smart, L. E. M. E. A. *Solid State Chemistry An Introduction*; 3rd ed.; CRC Press: Florida, USA, 2005.
- (44) West, A. R. *Basic Solid State Chemistry*; John Wiley & Sons, Ltd: England, 1999.
- (45) Neamen, D. A. *Semiconductor Physics and Devices Basic Principles*; Richard D. Irwin, INC: USA, 1992.
- (46) Dupont, E.; Liu, H. C.; Buchanan, M.; Chiu, S.; Gao, M. *Appl. Phys. Lett.* **2000**, 76, 4.
- (47) Sugawara, H.; Ishikawa, M.; Hatakoshi, G. *Appl. Phys. Lett.* **1991**, 58, 1010.
- (48) Piprek, J. *Semiconductor optoelectronic devices: introduction to physics and simulation*; Elsevier: Electronic reproduction, 2003.
- (49) Gupta, S.; Whitaker, J. F.; Mourou, G. A. *IEEE J. Quantum Elect.* **1992**, 28, 2464.
- (50) Sinton, R. A.; Cuevas, A. *Appl. Phys. Lett.* **1996**, 69, 2510.
- (51) Li, Y.; Jing, L.; Qiao, R.; Gao, M. *Chem. Commun.* **2011**, 47, 9293.
- (52) Alivisatos, A. P. *Science* **1996**, 271, 933.
- (53) Vossmeier, T.; Katsikas, L.; Giersig, M.; Popovic, I. G.; Diesner, K.; Chemseddine, A.; Eychmüller, A.; Weller, H. *J. Phys. Chem.* **1994**, 98, 7665.
- (54) Scholes, G. D.; Rumbles, G. *Nat. Mater.* **2006**, 5, 683.

- (55) Ashby, M. F. F., Paulo J.; Schodek, Daniel L. *Nanomaterials, Nanotechnologies and Design: An Introduction for Engineers and Architects* Elsevier: Electronic Reproduction, 2009.
- (56) Klimov, V. I. *Nanocrystal Quantum Dots*; CRC Press: Boca Raton, USA, 2010.
- (57) Ledoux, G.; Guillois, O.; Porterat, D.; Reynaud, C.; Huisken, F.; Kohn, B.; Paillard, V. *Phys. Rev. B* **2000**, *62*, 15942.
- (58) Canham, L. T. *Appl. Phys. Lett.* **1990**, *57*, 1046.
- (59) Cullis, A. G.; Canham, L. T.; Calcott, P. D. J. *J. Appl. Phys.* **1997**, *82*, 909.
- (60) Koehl, S.; Liu, A.; Paniccia, M. *Optics and Photonics News* **2011**, *22*, 25.
- (61) Hessel, C. M.; Henderson, E. J.; Kelly, J. A.; Cavell, R. G.; Sham, T. K.; Veinot, J. G. C. *J. Phys. Chem. C* **2008**, *112*, 14247.
- (62) Kovalev, D.; Heckler, H.; Ben-Chorin, M.; Polisski, G.; Schwartzkopff, M.; Koch, F. *Phys. Rev. Lett.* **1998**, *81*, 2803.
- (63) De Boer, W. D. A. M.; Timmerman, D.; Dohnalová, K.; Yassievich, I. N.; Zhang, H.; Buma, W. J.; Gregorkiewicz, T. *Nat. Nanotech.* **2010**, *5*, 878.
- (64) Nirmal, M.; Brus, L. *Acc. Chem. Res.* **1999**, *32*, 407.
- (65) V. A. Belyakov, V. A.; V. A. Burdov, V. A.; Lockwood, R.; Meldrum, A. *Adv. Opt. Tech.* **2008**, *2008*, 1.
- (66) Brus, L. *J. Phys. Chem.* **1994**, *98*, 3575.
- (67) Schmitt-Rink, S.; Miller, D. A. B.; Chemla, D. S. *Phys. Rev. B* **1987**, *35*, 8113.
- (68) Fauchet, P. M. *Mater. Today* **2005**, *8*, 26.
- (69) Kasap, S. O. C., Peter *Springer handbook of electronic and photonic materials*; Springer: Electronic reproduction, 2006.
- (70) Li, X.; He, Y.; Talukdar, S. S.; Swihart, M. T. *Langmuir* **2003**, *19*, 8490.
- (71) Hessel, C. M.; Henderson, E. J.; Veinot, J. G. C. *Chem. Mater.* **2006**, *18*, 6139.
- (72) Wolkin, M. V.; Jorne, J.; Fauchet, P. M.; Allan, G.; Delerue, C. *Phys. Rev. Lett.* **1999**, *82*, 197.
- (73) Ainslie, B. J. *J. Lightwave Technol.* **1991**, *9*, 220.
- (74) Bünzli, J. C. G.; Comby, S.; Chauvin, A. S.; Vandevyver, C. D. B. *J. Rare Earth* **2007**, *25*, 257.
- (75) Kenyon, A. J. *Prog. Quant. Electron.* **2002**, *26*, 225.
- (76) Pedersen, B.; Bjarklev, A.; Povlsen, J. H.; Dybdal, K.; Larsen, C. *J. Lightwave Technol.* **1991**, *9*, 1105.
- (77) Becker, P. C. *Erbium-doped fiber amplifiers: fundamentals and technology*; Academic Press.: Electronic reproduction, 1999.
- (78) Polman, A. *J. Appl. Phys.* **1997**, *82*, 1.
- (79) Mears, R. J.; Baker, S. R. *Opt. Quant. Electron.* **1992**, *24*, 517.
- (80) Kenyon, A. J. *Semicond. Sci. Technol.* **2005**, *20*, R65.

- (81) Polman, A.; van Veggel, F. C. J. M. *J. Opt. Soc. Am. B: Opt. Phys.* **2004**, *21*, 871.
- (82) Fujii, M.; Yoshida, M.; Kanzawa, Y.; Hayashi, S.; Yamamoto, K. *Appl. Phys. Lett.* **1997**, *71*, 1198.
- (83) St John, J.; Coffey, J. L.; Chen, Y.; Pinizzotto, R. F. *J. Am. Chem. Soc.* **1999**, *121*, 1888.
- (84) Chryssou, C. E.; Kenyon, A. J.; Iwayama, T. S.; Pitt, C. W.; Hole, D. E. *Appl. Phys. Lett.* **1999**, *75*, 2011.
- (85) Franzò, G.; Vinciguerra, V.; Priolo, F. *Appl. Phys. A-Mater.* **1999**, *69*, 3.
- (86) Kik, P. G.; Brongersma, M. L.; Polman, A. *Appl. Phys. Lett.* **2000**, *76*, 2325.
- (87) Choy, K.; Lenz, F.; Liang, X. X.; Marsiglio, F.; Meldrum, A. *Appl. Phys. Lett.* **2008**, *93*.
- (88) Kashkarov, P. K.; Kamenev, B. V.; Lisachenko, M. G.; Shalygina, O. A.; Timoshenko, V. Y.; Schmidt, M.; Heitmann, J.; Zacharias, M. *Phys. Solid State+* **2004**, *46*, 104.
- (89) Kik, P. G.; Polman, A. *Mat. Sci. Eng. B-Solid* **2001**, *81*, 3.
- (90) Kik, P. G.; Polman, A. *J. Appl. Phys.* **2000**, *88*, 1992.
- (91) Heitmann, J.; Müller, F.; Zacharias, M.; Gösele, U. *Adv. Mater.* **2005**, *17*, 795.
- (92) Sattler, K. D. *Handbook of nanophysics. Nanoparticles and quantum dots*; Taylor & Francis: Electronic reproduction, 2009.
- (93) Kannatey-Asibu, E. *Principles of laser materials processing* Wiley: New Jersey, USA, 2009.
- (94) Valenta, J.; Juhasz, R.; Linnros, J. *Appl. Phys. Lett.* **2002**, *80*, 1070.
- (95) Meldrum, A.; Haglund Jr, R. F.; Boatner, L. A.; White, C. W. *Adv. Mater.* **2001**, *13*, 1431.
- (96) Shimizu-Iwayama, T.; Ohshima, M.; Niimi, T.; Nakao, S.; Saitoh, K.; Fujita, T.; Itoh, N. *J. Phys.: Condens. Matter* **1993**, *5*, L375.
- (97) Kahler, U.; Hofmeister, H. *Opt. Mater.* **2001**, *17*, 83.
- (98) Yoshida, T.; Yamada, Y.; Orii, T. *J. Appl. Phys.* **1998**, *83*, 5427.
- (99) Orii, T.; Hirasawa, M.; Seto, T. *Appl. Phys. Lett.* **2003**, *83*, 3395.
- (100) Gourbilleau, F.; Portier, X.; Ternon, C.; Voivenel, P.; Madelon, R.; Rizk, R. *Appl. Phys. Lett.* **2001**, *78*, 3058.
- (101) Bley, R. A.; Kauzlarich, S. M. *J. Am. Chem. Soc.* **1996**, *118*, 12461.
- (102) Zhang, X.; Neiner, D.; Wang, S.; Louie, A. Y.; Kauzlarich, S. M. *Nanotechnology* **2007**, *18*.
- (103) Veinot, J. G. C. *Chem. Commun.* **2006**, 4160.
- (104) Holmes, J. D.; Ziegler, K. J.; Doty, R. C.; Pell, L. E.; Johnston, K. P.; Korgel, B. A. *J. Am. Chem. Soc.* **2001**, *123*, 3743.
- (105) Kelly, J. A.; Henderson, E. J.; Veinot, J. G. C. *Chem. Commun.* **2010**, *46*, 8704.
- (106) Wang, J.; Wang, X. F.; Li, Q.; Hryciw, A.; Meldrum, A. *Philos. Mag.* **2007**, *87*, 11.

- (107) Wilkinson, A. R.; Elliman, R. G. *Appl. Phys. Lett.* **2003**, 83, 5512.
- (108) Schubert, U. *Synthesis of inorganic materials*; Wiley-YCH: Germany, 2000.
- (109) Henderson, E. J.; Kelly, J. A.; Veinot, J. G. C. *Chem. Mater.* **2009**, 21, 5426.
- (110) Brinker, J. C. S., George, W. *Sol-gel science : the physics and chemistry of sol-gel processing*; Academic Press: USA, 1990.
- (111) Sorarù, G. D.; Modena, S.; Bettotti, P.; Das, G.; Mariotto, G.; Pavese, L. *Appl. Phys. Lett.* **2003**, 83, 749.
- (112) Das, G.; Ferraioli, L.; Bettotti, P.; De Angelis, F.; Mariotto, G.; Pavese, L.; Di Fabrizio, E.; Soraru, G. D. *Thin Solid Films* **2008**, 516, 6804.
- (113) Frye, C. L.; Collins, W. T. *J. Am. Chem. Soc.* **1970**, 92, 5586.
- (114) Loboda, M. J.; Grove, C. M.; Schneider, R. F. *J. Electrochem. Soc.* **1998**, 145, 2861.
- (115) Hessel, C. M.; Henderson, E. J.; Veinot, J. G. C. *J. Phys. Chem. C* **2007**, 111, 6956.
- (116) Hessel, C. M.; Summers, M. A.; Meldrum, A.; Malac, M.; Veinot, J. G. C. *Adv. Mater.* **2007**, 19, 3513.
- (117) Kelly, J. A.; Veinot, J. G. C. *ACS Nano* **2010**, 4, 4645.
- (118) Clark, R. J.; Dang, M. K. M.; Veinot, J. G. C. *Langmuir* **2011**, 27, 2073.
- (119) Bianucci, P.; Rodríguez, J. R.; Clements, C. M.; Veinot, J. G. C.; Meldrum, A. *J. Appl. Phys.* **2009**, 105.
- (120) Rodríguez, J. R.; Veinot, J. G. C.; Bianucci, P.; Meldrum, A. *Appl. Phys. Lett.* **2008**, 92.

# Chapter 2:

## Realization of Sensitized Erbium Luminescence in Silicon Nanocrystal Composites

*A version of this chapter has been published:*

*Rodriguez Núñez, J.; Veinot, J. G. C. J. Mat. Chem., 2011, 21, 1713.*

## 2.1. Introduction

Fiber optic technology has helped drive the globalization revolution of the last 50 years.<sup>1</sup> Thousands of kilometres of silica fiber optic cable under the Atlantic Ocean are responsible for communication between North America and Europe.<sup>2</sup> Optical signals carried over long distances suffer from attenuation and as a result multiple amplification steps are necessary to ensure their integrity. Common silica fibers employed in telecommunication applications exhibit a characteristic low-loss window between 1200 and 1700 nm.<sup>3</sup> Rare earth ions (e.g., Er<sup>3+</sup>,  $\lambda_{EM} = 1554\text{nm}$ ) are of particular interest for these applications given their sharp photoemission within this spectral region.<sup>4</sup> For this reason, erbium doped fiber amplifiers (EDFAs) are ubiquitous in the telecommunication industry.

Producing efficient Er<sup>3+</sup> based emission at 1554 nm is non-trivial and requires control of the matrix as well as Er environment; this photoemission arises from a Laporte forbidden (i.e.,  $\Delta l \neq \pm 1$ ) *f-f* transition ( $^4I_{13/2} \rightarrow ^4I_{15/2}$ ) with an optical cross-section of ca.  $10^{-21} \text{ cm}^2$ .<sup>5,6</sup> Furthermore, the desired luminescence at 1554 nm is also coincident with the second vibronic transition of many hydroxyl-containing species within impure silicon oxides making non-radiative relaxation more probable and the use of high purity silica paramount.<sup>7-9</sup>

The coordination environment of the Er center is also believed to impact the efficiency of the 1554 nm emission. *Cooperative upconversion* (UC), in which one ion decays non-radiatively to the ground state while transferring its excess energy to an ion in close proximity, substantially lowers emission intensity.

Similarly, *excited state absorption* in which a promoted electron of the long-lived  $\text{Er}^{3+}$  excited state may be additionally pumped to a higher energy state by the pump beam.<sup>10,11</sup> Both of these processes lead to diminished photoluminescence at 1554 nm and can play an important role which is compounded in telecommunication applications because of the associated high pumping powers necessary to realize the desired emission with sufficient intensity.<sup>5</sup>

A promising approach toward improving the efficiency of room temperature 1554 nm luminescence exploits the interaction of implanted  $\text{Er}^{3+}$  ions in a silicon substrate. In bulk silicon, the desired optical transition is “partially allowed” when  $\text{Er}^{3+}$  ions are bonded in a distorted octahedral geometry.<sup>12,13</sup> Furthermore, it is now known that when erbium ions are placed in close proximity to emissive silicon nanocrystals (Si-NCs), the rare earth emission is greatly enhanced and the effective absorption cross-section is markedly improved (i.e.,  $10^{-15}$  vs.  $10^{-21}$   $\text{cm}^2$ ).<sup>14-19</sup> Similar observations are noted when silicon nanoclusters (i.e., non-crystalline particles) that exhibit defect related luminescence are employed.<sup>20-22</sup> While nanocluster-based systems hold some advantages (e.g., lower processing temperatures), ions must be closer to the nanoclusters for the sensitization process to occur efficiently.<sup>23,24</sup> The exact mechanism for nanocluster/crystal sensitization of  $\text{Er}^{3+}$  emission remains the subject of some debate, however it is generally accepted that a Förster energy transfer mechanism is active in which the Si-NCs act as antennae, receiving the excitation energy and transferring it to the erbium center with high efficiency.<sup>25-29</sup>

A variety of approaches toward placing erbium ions near Si-NCs in an oxide matrix have been reported. Coffey et al. developed chemical vapour deposition methods in which a Si-NC precursor mixes with an erbium precursor along a heated tube.<sup>30,31</sup> The resulting deposited material displays strong erbium luminescence when pumped using the 488 nm line of an Ar<sup>+</sup> laser (i.e., resonant with Er<sup>3+</sup> excitation). Other physical methods such as ion implantation,<sup>25</sup> plasma enhanced vapour deposition,<sup>32</sup> and magnetron sputtering,<sup>33</sup> have also yielded various nanomaterials displaying strong luminescence in the near-IR spectral region. All these investigations have contributed to an understanding of the energy transfer mechanism, however the incorporation of the associated methods into practical application could prove challenging. For example, physical deposition methods are line-of-sight techniques, thus coating non-planar surfaces such as silica fibers using these methods is not straightforward; these procedures also require expensive infrastructure that can be both labour and resource intensive to operate and maintain.

There is a need to develop precursors that yield silicon nanocrystals in high quality erbium containing silica matrix through straightforward methodologies while affording control of erbium ion concentration and distribution homogeneity. Our group has demonstrated that reductive thermal processing of hydrogen silsesquioxane (HSQ) yields Si-NCs embedded in a silica matrix (Si-NC/SiO<sub>2</sub>).<sup>34</sup> The solution processability of this unique Si-NC precursor has facilitated effective patterning, coating of non-planar surfaces (e.g., optical fibers)<sup>35</sup> and the efficient confinement of Si-NC emission in cylindrical

optical cavities leading to the observation of whispering gallery modes.<sup>36</sup> We have also reported that a mixture of erbium chloride ( $\text{ErCl}_3$ ) and HSQ dissolved in methyl isobutylketone (MIBK) may be spin coated and thermally processed to yield thin films that luminesce at  $\sim 880$  nm (characteristic of Si-NCs) as well as 1534 nm (characteristic of  $\text{Er}^{3+}$ ).<sup>35</sup> These early reports suggest effective  $\text{Er}^{3+}$  doping into a Si-NC/ $\text{SiO}_2$  matrix, however further study is required if useful practical materials are to be prepared. Adding to the appeal of a study investigating Er doping of HSQ derived Si-NC/ $\text{SiO}_2$  composites is the unique opportunity to obtain bulk quantities (i.e., grams) of doped material that allow for detailed characterization. To the best of our knowledge the ability to produce gram quantities of Er doped composites is limited to our synthetic method.

In this work, we present an in-depth study of a series of molecular erbium precursors and their impact on material properties of Si-NCs/ $\text{SiO}_2$  placing emphasis on the homogeneity of the erbium distribution, crystallinity of the silicon nanodomains and photoluminescence (PL) properties.

## **2.2. Experimental Details**

All commercially available reagents were purchased at the highest possible purity from the indicated suppliers and used as received.

### **2.2.1. Material preparation**

#### **2.2.1.1. Erbium chloride ( $\text{ErCl}_3$ ) and Erbium tris(bis(trimethyl silyl) amide (ErA) precursor mixtures:**

Erbium chloride (Alpha-Aesar) and ErA (Gelest) were added to stock HSQ solution dissolved in MIBK (sold as 4-methyl 2-pentanone 99+% Sigma Aldrich) at concentrations (at% of erbium relative to total silicon content) listed in Table 2.1.  $\text{ErCl}_3$  containing precursor mixtures were stirred for 30 minutes to suspend the fine powder and maximize the homogeneity of physical mixing. ErA containing mixtures form gels which produce hydrogen gas while crosslinking. Following mixing and/or gelation, MIBK is removed yielding a white powder that was thermally processed under slightly reducing conditions (*vide infra*) to yield Er-doped Si-NC/SiO<sub>2</sub> composites.

**Table 2.1** Synthesis of Erbium containing Si-NC/SiO<sub>2</sub> composites

Sample <sup>a</sup>	Erbium Source	Concentration (at.%)
1	ErCl <sub>3</sub>	0.01
2	ErCl <sub>3</sub>	0.05
3	ErCl <sub>3</sub>	0.1
4	ErCl <sub>3</sub>	0.5
5	ErA	0.01
6	ErA	0.05
7	ErA	0.1
8	ErA	0.5
9	ErOct	0.01
10	ErOct	0.05
11	ErOct	0.1
12	ErOct	0.5
13	-	-
Si-NC/SiO <sub>2</sub>		

<sup>a</sup> Samples before heating will be denoted by their designated sample number. Samples after heating will be denoted by the sample number followed by the letter a.

### **2.2.1.2. Erbium octanoate (ErOct) solution preparation**

ErOct is prepared by reacting ErA with three equivalents of octanoic acid (Sigma Aldrich) in anhydrous m-xylene 99+% (Sigma Aldrich). The by-product, hexamethyldisilazane (HMDS, b.p. 124 °C) is quantitatively removed by evaporation using standard Schlenk techniques. The ErOct solution is added to HSQ dissolved in dry m-xylene at concentrations ranging between 0.01 to 0.5 at.% as outlined in Table 1. After stirring for 30 min., the solvent was removed to yield a white powder.

### **2.2.1.3. Preparation of Er-doped Si-NC/SiO<sub>2</sub> composites**

A control sample of Si-NCs/SiO<sub>2</sub> (free of Er) was prepared by heating HSQ to 1100 °C under 5% H<sub>2</sub> 95% Ar. Detailed characterization has been reported elsewhere.<sup>34,35</sup> White powders containing HSQ and the erbium precursors were heated to 1100 °C, at a heating rate of 18°C/min, under a 95% Ar, 5%H<sub>2</sub> atmosphere for 1 hour, composites were allowed to cool to room temperature over 4 hours.

## **2.2.2. Material Characterization**

### **2.2.2.1. Fourier Transform IR spectroscopy (FTIR)**

A Thermo Nicolet Nic-Plan FTIR microscope attached to a Magna 750 main bench was used to collect spectra. The sample spectra and backgrounds were collected in transmission mode at 4 cm<sup>-1</sup> resolution and 32 scans. The ErOct samples were drop coated from an m-xylene solution onto a KBr plate.

### **2.2.2.2. Scanning electron microscopy (SEM)**

Backscattered electron imaging, as well as energy dispersive X-ray spectroscopy (EDX) were used to study the distribution of erbium in the composites. SEM samples were coated with chromium using an Edwards Xenosput XE 200 coater. EDX of composites was obtained using a liquid nitrogen cooled lithium drifted silicon energy dispersive X-ray detector with a Norvar window manufactured by PGT. Backscattered electron images were collected using a JEOL 6301F field emission SEM.

### **2.2.2.3. X-ray photoelectron spectroscopy (XPS)**

XPS measurements were performed on AXIS-165 spectrometers (Kratos Analytical) at the Alberta Centre for Surface Engineering and Science (ACES), in the University of Alberta. The base pressure in the analytical chamber was lower than  $3 \times 10^{-8}$  Pa. A monochromatic Al K $\alpha$  source ( $h\nu = 1486.6$  eV) was used at a power of 210 W. The analysis spot was 400 x 700  $\mu\text{m}$ . The instrument resolution is 0.55 eV and 0.70 eV for the Ag 3d and Au 4f emissions, respectively. For high resolution spectra the pass-energy was 20 eV with a step of 0.1 eV. Electron flooding was required to compensate the sample charging during the analysis.

#### **2.2.2.4. X-ray diffraction (XRD)**

XRD was performed using an INEL XRG 3000 X-ray diffractometer equipped with a Cu K $\alpha$  radiation source ( $\lambda = 1.54 \text{ \AA}$ ). All samples were finely ground and placed on silicon (100) sample holder for data collection.

#### **2.2.2.5. Photoluminescence (PL) measurements.**

PL samples were prepared by drop coating composites onto a silicon wafer. The 325 nm line of a He/Cd laser (non-resonant with Er<sup>3+</sup> excitation) was used to excite all samples presented in this study. The spectral response was corrected using a standard blackbody radiator. Luminescence between 300 nm and 900 nm was detected using a USB2000 spectrometer from Ocean Optics, near-IR photoluminescence (880 nm – 1700 nm) was collected using a NIR 512 spectrometer from Ocean Optics. Visible and near-IR PL spectra were collected simultaneously using a split fiber optic. Laser light was filtered out using a 450 nm coloured glass long pass filter purchased from Thor Labs.

#### **2.2.2.6. *In situ* PL during HF etching of composites**

Composites 4a, 8a, 12a, and 13a were etched using a mixture of H<sub>2</sub>O:EtOH:49%HF in a 1:1:1 (v/v/v) ratio. 0.01 g of composite was placed in a sealed Eppendorf tube, the etching mixture was then added. (**Caution:** Hydrofluoric acid is poisonous, corrosive, extremely hazardous and may be fatal if swallowed or inhaled. Exercise extreme caution when using this acid). A small hole was made in the Eppendorf tube to release the pressure build-up due to the

SiF<sub>4</sub> gas being evolved. As the etching proceeded, PL spectra were collected *in situ* using a fiber optic attached to the setup described in the PL measurements section. Spectra obtained are not normalized to display the difference in PL intensity after matrix removal.

#### **2.2.2.7. Nuclear Magnetic Resonance (NMR)**

An NMR study was used to elucidate the gas being evolved during gelation of HSQ. In this experiment a small amount of HSQ was dissolved in deuterated toluene inside an NMR tube. Once HSQ is thoroughly dissolved the solution is frozen using liquid nitrogen. Once it is frozen, a small amount of solid ErA is added into the NMR tube. The tube is placed in an i400 Agilent/Varian Inova two-channel 400 MHz NMR at -80 °C and slowly warmed up. NMR spectra were collected at -80 °C, -60 °C, -40 °C and 30 °C. Once the NMR tube is warmed up to room temperature it is removed from i400 and a gel is clearly visible.

### 2.3. Results and Discussion

Hydrogen silsesquioxane (HSQ) is available commercially from Dow Corning Corporation as FOx-#, where # defines the solution concentration. FOx-# is sold as a high purity, electronics grade material and finds application as a spin-on dielectric and e-beam resist.<sup>37</sup> We have established HSQ as a versatile Si-NC/SiO<sub>2</sub> precursor that affords gram quantities of material making detailed material characterization possible.<sup>34</sup> In light of small sample size, similar evaluations are not readily accessible for analogous materials from physical methods. Adding to the appeal of HSQ, its solution processability provides a convenient method to coat non-planar surfaces (e.g., optical fibers and capillary tubes)<sup>35,36,38</sup> with Si-NC/SiO<sub>2</sub>. Realizing effective coating of these and other more complex architectures is pivotal in the development of Si-NC optical components such as photonic amplifiers and lasers.<sup>39,40</sup>

Obtaining efficient photoluminescence from Si-NC/SiO<sub>2</sub> within the optimal transparency window of silica-based photonic materials could have a significant impact in the development of optical communication systems. The integration of solution processable HSQ to the fabrication of these materials will allow for unprecedented and convenient solution-based device fabrication. Previously, we reported that thin films, obtained from thermal processing a physical mixture of ErCl<sub>3</sub> with HSQ, showed characteristic erbium luminescence at 1554 nm when pumped non-resonantly.<sup>35</sup> These observations indicate Si-NC sensitization is indeed possible with HSQ-derived materials; still, substantial Si-

NC emission remained indicating energy transfer from Si-NCs to the Er<sup>3+</sup> centers was not optimized. In light of the limited solubility of ErCl<sub>3</sub> in HSQ compatible solvents, two reasonable factors that could limit the Er-based emission intensity are: i) Er concentration is not sufficient to facilitate energy transfer from all Si-NCs to Er emissive centers, and ii) distribution of Er throughout the composite is not homogeneous, thereby limiting energy transfer and increasing the probability of cooperative upconversion. Clearly, if HSQ-derived materials are to find application in photonic devices, the effect of Er precursor chemical structure on composite properties structure and optical response must be elucidated and understood. To further explore sensitized Er emission from HSQ derived materials, we initiated the present study of two structurally tailored Er-precursors with HSQ compatible solubility properties and expanded our investigation of ErCl<sub>3</sub>.

Preparation of precursor mixtures 1-12 was achieved via suspension (1-4) or solution (5-12) mixing of the erbium source of choice with HSQ in an appropriate solvent. In light of its limited solubility in MIBK, addition of ErCl<sub>3</sub> yielded a colloidal suspension. ErA is soluble in MIBK, but its addition induced liberation of a gas and gelling of the HSQ, gelation occurs in other non-polar solvents such as THF, toluene and m-xylene. Solutions of ErOct and HSQ in m-xylene were combined, no gelation was observed. For all precursor mixtures, solvent was removed to yield white powders that were subsequently thermally processed in slightly reducing conditions (*vide supra*) to yield Er doped

composites that were evaluated for photoluminescent response, compositional uniformity, and presence of Si-NC.

Photoluminescence (PL) spectra of all erbium doped Si-NC/SiO<sub>2</sub> composites (i.e., 1a-12a) were evaluated using the 325 nm line of a He/Cd laser and emission was detected using a USB2000 and a NIR 512 spectrometers. This excitation source is non-resonant with all erbium energy transitions and permits efficient excitation of Si-NCs. From this, we conclude all observed erbium luminescence arises from indirect pumping (i.e., energy transfer processes).

PL spectra obtained from 1a-4a (Fig. 2.1) show erbium luminescence at 1554 nm. We also note small variations in the emission maximum of the emission band arising from Si-NCs at ~ 800 nm. Increasing the erbium concentration (i.e., samples 1-4) causes a corresponding increase in the Er-based emission intensity indicating that, at the present concentrations and laser power, UC is not measurable in HSQ/ErCl<sub>3</sub> derived systems. UC will manifest itself by a decrease in Er<sup>3+</sup> PL at 1554 nm and the appearance of a peak at ~ 980 nm, neither of these occur in our samples. While UC was not observed for 1a-4a, challenges could remain when using higher pumping powers routinely employed in erbium doped fiber amplifiers. Unfortunately, higher power excitation was not accessible with the laser used in this experiment.

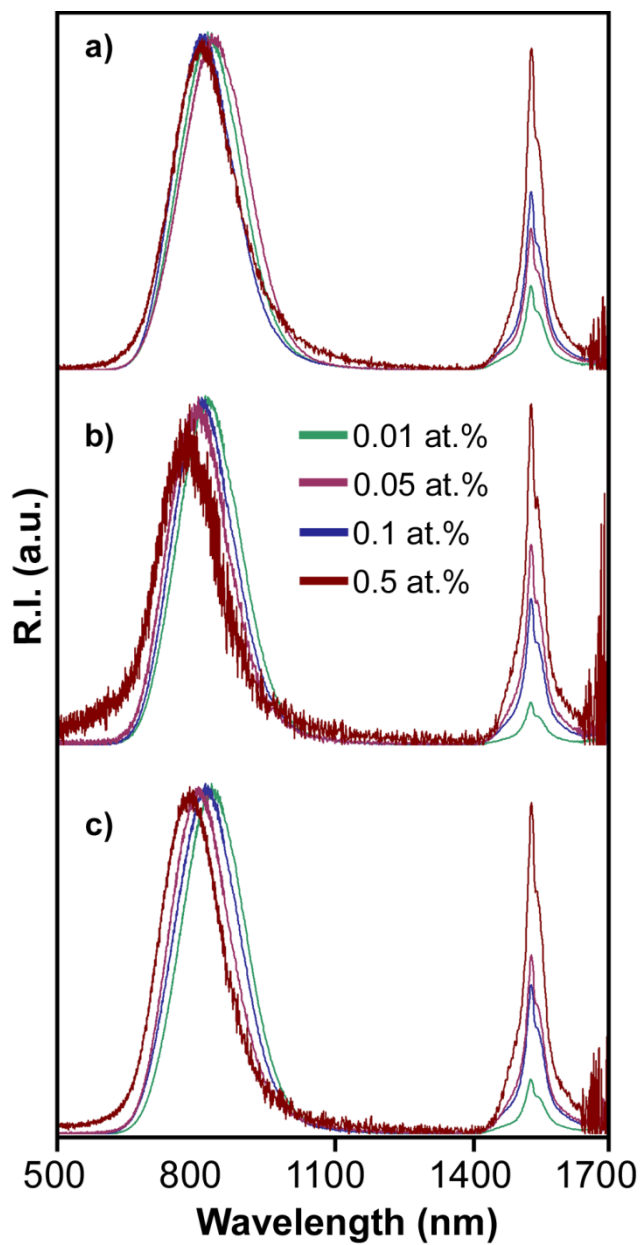


**Fig. 2.1** Photoluminescence spectra of composites containing (a) ErCl<sub>3</sub> (1a-4a), (b) ErA (5a-8a), and (c) ErOct (9a-12a). Composites were drop coated onto silicon wafers and excited using the 325 nm line of a He/Cd (not resonant with Er<sup>3+</sup> excitation). All spectra are normalized to the silicon luminescence.

Similar Er concentration dependencies are noted when examining the PL spectra of 5a – 8a (Figure 2.1b). An increase in 1554 nm emission intensity is seen with greater Er incorporation. A slight blue shift is also noted for the Si-NC emission with higher Er concentrations, as well as a marked decrease in the intensity of the Si-NC emission band relative to the erbium emission. Two possible explanations for this are: an increase in sensitization efficiency or decrease in the nanocrystal size and concentration arising from a decreased yield of Si-NCs resulting from ErA induced crosslinking of HSQ. The latter of these is consistent with present XRD analyses (*vide infra*).

Comparing the PL of samples containing 0.5 at.% ErCl<sub>3</sub> and ErA, (4a and 8a) we note the Si-NC emission of 8a appears blueshifted approximately 20 nm compared to that of 4a. In addition, while the relative intensities of erbium and Si-NC based emissions are similar for composites obtained using ErCl<sub>3</sub> and ErA we can qualitatively state the silicon luminescence is lower in the ErA prepared samples based upon the observed spectral noise (collection times were the same for all spectra). As with samples 1a-4a, UC effects were not detected.

PL analyses (Fig. 2.1c) of ErOct-derived composites (i.e., 9a-12a) also show a clear increase in the Er-based emission as Er concentration increases up to 0.5 at.%. As was the case for ErA, the Si-based PL blueshifts and decreases in intensity with increased Er content. A reasonable explanation for this trend, consistent with our XRD analysis (*vide infra*), is the formation of smaller Si

domains resulting from a high density of heterogeneous nucleation centres that arise because of the addition of ErOct.<sup>30</sup>

It is well established UC occurs when erbium ions are in close spatial proximity.<sup>5,11,30</sup> In 2009, Lu, et al. reported a green Er<sup>3+</sup> microlaser using resonant excitation at 1460 nm.<sup>41</sup> In the design of an erbium device expected to emit at 1554 nm, the even distribution of the ions in the matrix is critical in decreasing UC and therefore increasing the efficiency of the system. Furthermore, homogeneous distribution of erbium ions in the matrix might increase sensitization efficiencies. For this reason, homogeneity of the Er dispersion was evaluated for the present systems. Backscattered electron SEM imaging and EDX provide insight into erbium dispersion homogeneity. SEM of **3a** (i.e., 0.1 at.% Er, Fig. 2.2a) and **4a** (Fig. 2.2b) show bright regions confirmed to contain (EDX) erbium and chlorine (Fig. 2.2c). Differentiating between ErCl<sub>3</sub> and optically active erbium oxide is not possible using these techniques. Based on the respective solubilities of ErCl<sub>3</sub> and HSQ in MIBK, it can be suggested that ErCl<sub>3</sub> precipitates to form small ErCl<sub>3</sub> rich regions. Upon thermal processing, ErCl<sub>3</sub> regions melt (m.p. = ErCl<sub>3</sub>: 776 °C) and some Er<sup>3+</sup> ions diffuse into the SiO<sub>2</sub> matrix; these ions are sensitized by Si-NCs upon photoexcitation. Following processing, relatively large ErCl<sub>3</sub> regions remain and appear as bright spots in backscattered SEM analyses. As a result of the non-uniform Er distribution, it is reasonable that UC will play a deleterious role when optically pumping these materials with higher power sources. Furthermore, much of the Er remains inaccessible to Si-NC sensitization.

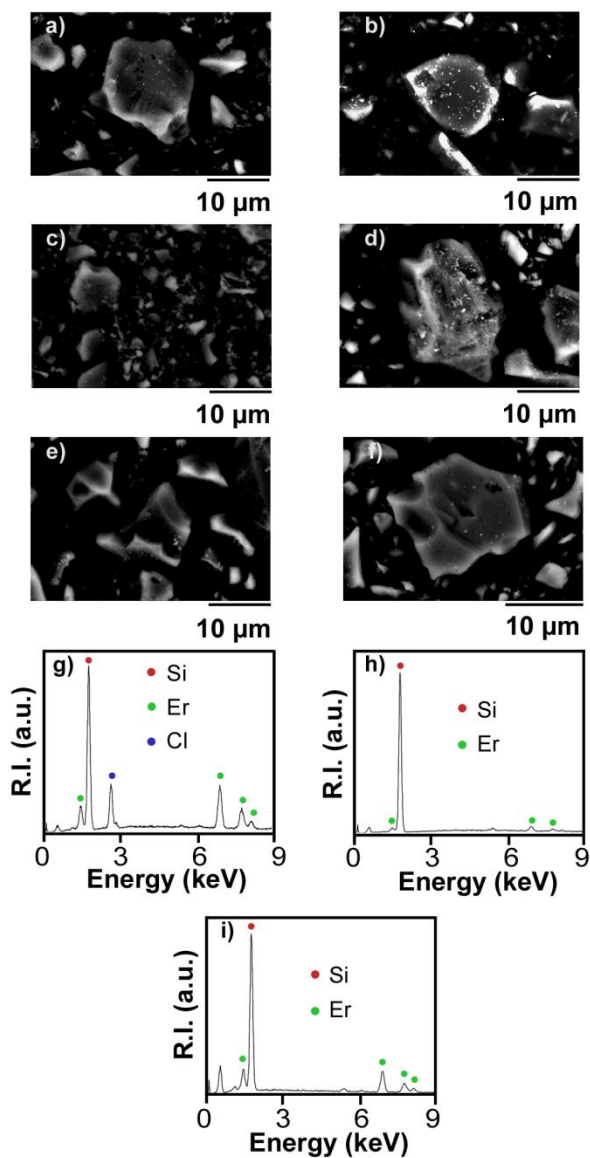
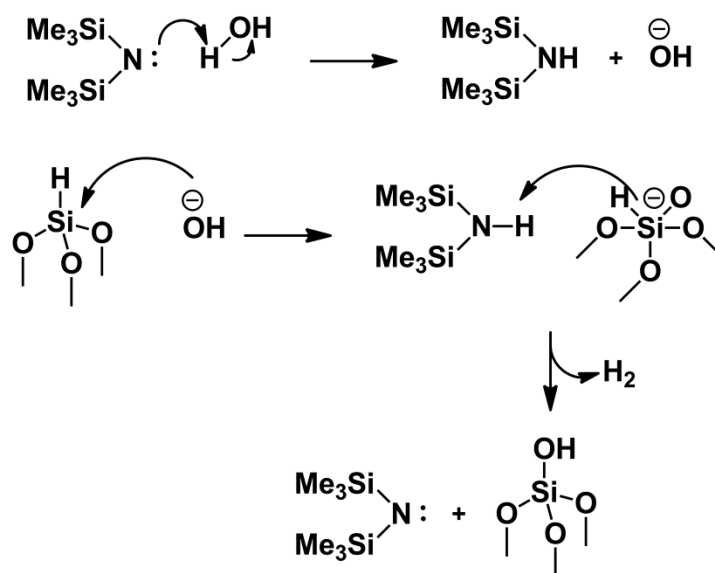


**Fig. 2.2** Backscattered SEM images of composites 3a (a), 4a (b), 7a (c), 8a (d), 11a (e), and 12a (f); bright spots are microscopic Er clusters. EDX of 4a (g), 8a (h), and 12a (i) was collected by focusing the beam on the bright spots in the backscattered electron images. EDX suggests the presence of  $\text{ErCl}_3$  in sample 4a.

The solution properties of erbium tris(bis(trimethyl)silyl)amide (i.e., ErA) are expected to afford more effective solution mixing with HSQ than that

observed for  $\text{ErCl}_3$ . In principle, this should lead to more efficient sensitization and minimization of UC influences, still the influence of gelling caused by the addition of ErA to the MIBK solution of HSQ is unclear. While the specific reaction leading to the gel formation is the subject of ongoing investigation, it is interesting to note that addition of hexamethyldisilazane (HMDS), the ligand in ErA at the concentrations currently employed, does not induce crosslinking. Examples of amine induced silanol polymerization are present in the literature.<sup>42-44</sup> It is reasonable to propose that Si-H moieties in HSQ are oxidized to yield silanols via amine based catalysis (Scheme 2.1). Silanols can subsequently polymerize causing gelation in the presence of ErA.



**Scheme 2.1** Proposed amine based catalysis of Si-H moieties in HSQ. Resulting silanols can crosslink via condensation releasing water.

While gel formation precludes application of ErA in thin film preparation, a study of the resulting material provides valuable information regarding the

influence of dispersion of Er throughout the resulting Si-NC/SiO<sub>2</sub> bulk composite. In contrast to ErCl<sub>3</sub> derived samples (i.e., 1a-4a), backscattered SEM images (Figure 2.2c) show no evidence of erbium rich domains at 0.1 at.% Er (i.e., sample number 7a) and only minor clustering at 0.5 at.% (i.e., sample number 8a, Figure 2.2d). These observations indicate that intimate solution-phase mixing facilitates uniform Er dispersion in the composite matrix. We also observed that the basicity of the rare earth ligand dictates the crosslinking of the HSQ solution and the properties of the resulting composite. Other erbium precursors with basic ligands such as erbium 8-hydroxyquinolate (Sigma Aldrich) cause gelling of the HSQ solution in a similar fashion to ErA. ErCl<sub>3</sub> can also crosslink the HSQ solution but only at very high concentrations (> 5 at.%).

When HSQ is mixed with Er<sup>3+</sup> precursors containing basic ligands the evolution of gas precedes gelation. In order to determine the nature of the gas being evolved, we carried out a low temperature NMR study. Solid HSQ was dissolved in deuterated toluene in an NMR tube. The solution was immediately dipped in liquid nitrogen until frozen. Once solid, a small amount of ErA was added to the NMR tube and placed in a 400 MHz NMR at 80 °C and warmed up slowly. A broad peak at approximately 4.26 ppm corresponding to Si-H is clearly visible at temperatures below -60 °C (Figure 2.3.a,b). When the temperature rises to -40 °C, a small peak starts to appear at 4.5 ppm characteristic of H<sub>2(g)</sub>. As the temperature rises, the Si-H peak decreases in intensity while the H<sub>2(g)</sub> peak increases (Figure 2.3c,d).

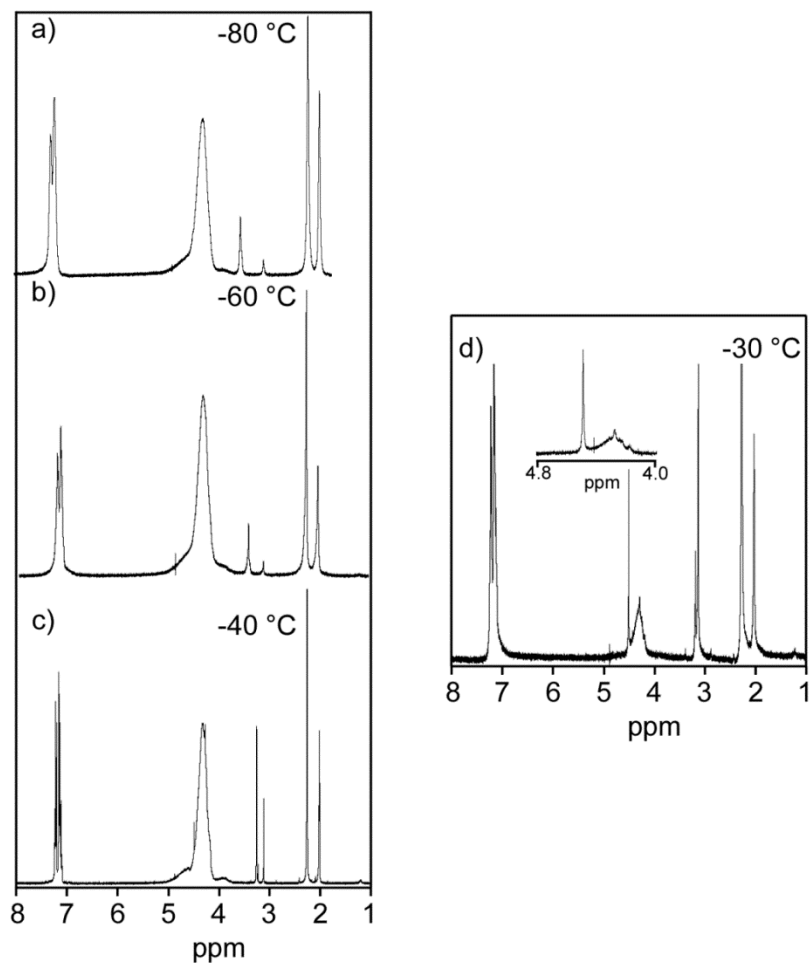


**Fig. 2.3** NMR of HSQ mixed with ErA at -80 °C (a), -60 °C (b), -40 °C (c), -30 °C (d). Inset on (d) shows the mixture at -30 °C for a few minutes. At -40 °C a small peak can be seen at 4.5 ppm characteristic of  $H_{2(g)}$ . At -30°C a clear decrease in the Si-H peak (4.26 ppm) is observed while the  $H_{2(g)}$  signal increases.

Erbium octanoate (ErOct) was chosen as an alternative precursor that balances solubility and reactivity. Examination of the ErOct derived composite using SEM shows similar Er clustering trends to those observed for ErA. Clearly, the similar solution compatibility of ErOct and HSQ allow for intimate precursor mixing and minimal microscopic precipitation/clustering in the final Si-NC/SiO<sub>2</sub> composite for the concentrations investigated. ErOct is synthesized by reaction of ErA and octanoic acid. The product was characterized using IR spectroscopy which clearly shows the disappearance of the spectral signature of octanoic acid (i.e., OH stretching at ca. 3400 cm<sup>-1</sup> and C=O stretch at ca. 1700 cm<sup>-1</sup>) and the appearance of a doublet between 1400 – 1600 cm<sup>-1</sup> attributable to C-O symmetric and asymmetric stretches (Figure 2.4).<sup>45</sup> Electropray mass spectrometry afforded a peak corresponding to 597 g/mol confirming the product is ErOct.

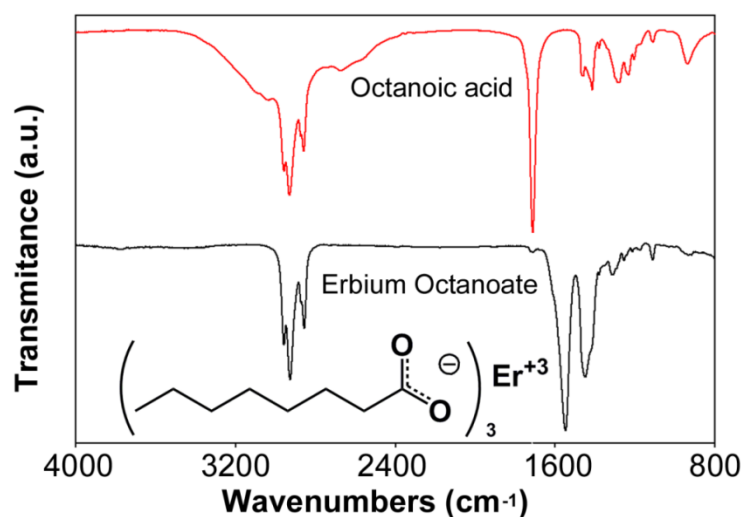


**Fig. 2.4** IR spectra showing the disappearance of the OH stretch (~ 3200 cm<sup>-1</sup>) and the appearance of the C-O symmetric and asymmetric stretches upon acid coordination.

X-ray powder diffraction (XRD) provides a direct probe of crystalline silicon nanodomains within the present composites. Figure 2.5 shows diffraction patterns obtained for composites 4a, 8a, 12a, and 13a. XRD patterns containing lower  $\text{Er}^{3+}$  concentrations are not shown but display similar results as those composites of higher concentrations. Samples 4a, 8a, 12a, and reference sample 13a show an intense reflection centered at approximately  $20^\circ$  that arises from the amorphous silica-like matrix.<sup>34</sup> In addition, reflections at  $28^\circ$ ,  $48^\circ$ , and  $57^\circ$  readily attributed to nanocrystalline silicon are present in the XRD patterns for 4a and 13a (reflection of 4a may not be clear due to stacking, for a single image see supplementary information). Reflections arising from Si-NCs are just baseline resolved and broader for 8a and 12a. This suggests Si-NCs are smaller and/or fewer in number in doped composites consistent with the blueshift noted in the PL spectra (Figure 2.1b). The origin of these differences is not obvious, however loss of the silicon hydride moiety during ErA induced crosslinking may limit necessary disproportionation reactions and highlights the importance of precursor chemical compatibility. It is unclear what hinders formation of Si-NCs in ErOct doped composites, however we have made similar observations for other carbon-based dopants; this is the subject of a more general ongoing investigation. Another feature present in the composite XRD pattern of sample 4a is low intensity reflections arising from crystalline  $\text{ErCl}_3$  consistent with dopant precipitation (*vide supra*).

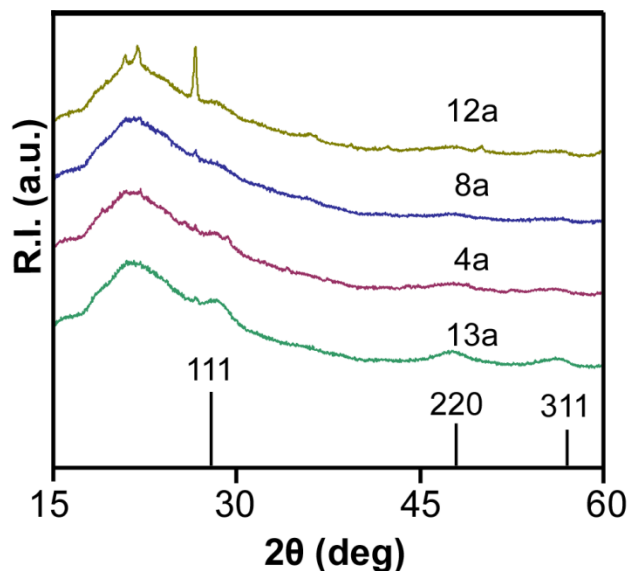


**Fig. 2.5** XRD patterns of samples 4a, 8a, 12a, and 13a. The 111, 220 and 311 reflections are clear in the control sample and visible in sample 4a, other composites show small or undetectable peaks. Samples were run on a silicon  $\langle 100 \rangle$  holder.

X-ray photoelectron spectroscopy (XPS) provides valuable information regarding both non-crystalline and crystalline silicon nanodomains through evaluation of the Si oxidation state. XP spectra of 4a, 8a, 12a, and 13a are shown in Figure 2.6. All spectra were calibrated to the C1s emission at 284.8 eV and intensities were normalized to the highest intensity peak, namely the Si (IV) emission, to allow direct comparison of Si(0) content. It is clear that the relative concentrations of Si(0) and Si(IV) are constant (i.e., within 0.1 at.%) for 4a and 13a.

The XP spectra of 8a and 12a are more complex; the intensity and energy of the Si(0) based emission differ from the other composites investigated here. In addition, the “Si(IV)” emission of 8a is shifted to lower binding energy relative to 4a, 13a. The location and intensity of the Si(0) emission may be understood when considering non-crystalline Si(0) nanodomains detectable in very low concentrations using XRD analysis (*vide supra*) and using HF etching/PL studies (*vide infra*); domains of this type exhibit variable binding energies.<sup>46</sup> Consistent with this explanation, a shift to lower binding energy for the Si(IV) emission (i.e., greater sub-oxide character) is expected because of the less well defined Si(0) and Si(IV) regions. It is clear the ErA induced crosslinking of HSQ produced a more structurally complex precursor that limits Si(0) concentration and hinders Si-NC formation and growth.

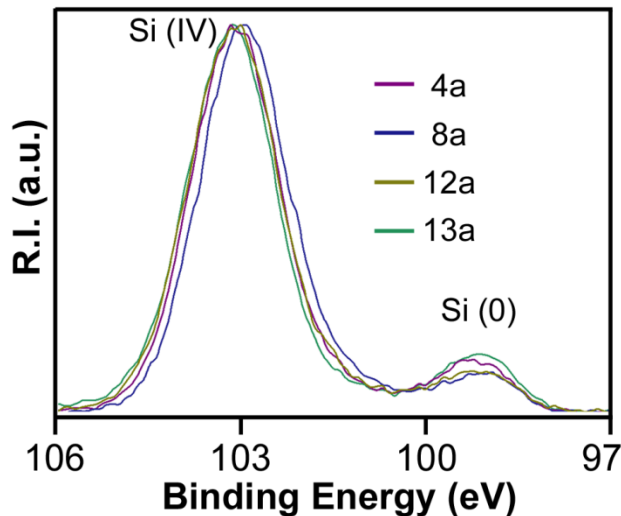


**Fig. 2.6** XP spectra of samples 4a, 8a, 12a, and 13a. Spectra were normalized to the highest intensity Si(IV) peak. Samples 8a and 12a have lower Si (0) intensity compared to samples 4a and 13a. ErA (8a) sample displays more suboxide character than all other samples.

An important aspect of preparing Er doped silicon rich oxides (SROs) via sol-gel mediated synthesis is the availability of large sample sizes.<sup>34,47</sup> This alone offers a unique opportunity to explore the Er environment. It is generally accepted for analogous Er-doped materials prepared using physical methods, that erbium is confined to the silica matrix.<sup>29,48</sup> Still, examples of freestanding nanoparticles displaying erbium emission exist.<sup>30</sup> The large quantities of material available from the presented synthetic approach allow for indirect probing of the Er location (i.e., oxide or nanocrystals) in the composite via straightforward HF etching and photoluminescence spectroscopy. We have established HF etching as an effective method for liberating freestanding Si from their oxide matrix.<sup>34</sup> In this regard, it is reasonable to suggest that HF etching will effectively isolate Si-

NCs from any oxide embedded Er and prevent sensitization. Photoluminescence spectroscopy offers direct monitoring of the sensitization process.

Samples 4a, 8a, and 12a were exposed to a water:ethanol:49%HF solution. Generally, upon initial exposure, the silica-like matrix is dissolved to yield freestanding hydride surface terminated Si-NCs. The dimensions of liberated Si-NCs decrease with extended HF exposure as a result of slow etching of the Si surface; this causes a slight blue shift in the Si-NC based luminescence maximum in accordance with quantum confinement. All samples were etched under identical conditions and their PL was monitored throughout the etching process. Etching a control composite containing no erbium ions (i.e., 13a) shows a dramatic decrease in PL intensity for the band centred at 840 nm (See Figure 2.7a). The initial loss of emission intensity may be explained by the formation of non-radiative defects on the liberated NC surfaces with HF etching. As the etching proceeds, these defects are passivated by hydride moieties and a new emission band appears consistent with nanocrystals with a size ranging between 2.5 – 4 nm.<sup>34,46,49</sup>

Monitoring the Si-NC and Er based emission bands of 4a, 8a and 12a provides valuable insight into the location of the Er<sup>3+</sup> ions within the composites as well as indirect information regarding the Si nanodomains. In all cases, exposing Er doped composites to HF leads to complete loss of Er-based emission, confirming sensitization is occurring and close proximity of the Er ions to oxide embedded nanodomains is crucial to the energy transfer mechanism. The

evolution of the Si-NC emission band of 4a shows a similar trend to that observed for 13a, as etching proceeds the Si-NC is quenched and subsequently reappears at higher energy. In addition, Figure 2.7a shows the high energy peak has lower intensity than the low energy oxide embedded Si-NC component, in contrast with Figure 2.7b which shows an opposite trend. We attributed this observation to the presence of sensitized erbium ions. In sample 4a (Figure 2.7b) some of the excitons that are formed in the Si-NC upon laser excitation recombine non-radiatively to excite the  $\text{Er}^{3+}$  ions, causing a decrease in the Si-NC luminescence. As the matrix is etched away, the erbium ions are no longer sensitized and the intensity of the silicon nanocrystals increases. To our knowledge, this is the first direct chemical evidence of the location of the active  $\text{Er}^{3+}$  site and of the sensitization process. The Si based PL of 8a and 12a evolves very differently: in both cases it is completely quenched upon etching and does not reappear with extended exposure to HF. We propose this arises because the Si nanodomains in ErA and ErOct derived composites are not crystalline and are etched away rapidly upon exposure to HF. This is consistent with the presented XPS analyses that confirm the presence of Si(0) and XRD that show reflections of only negligible intensity arising from Si.

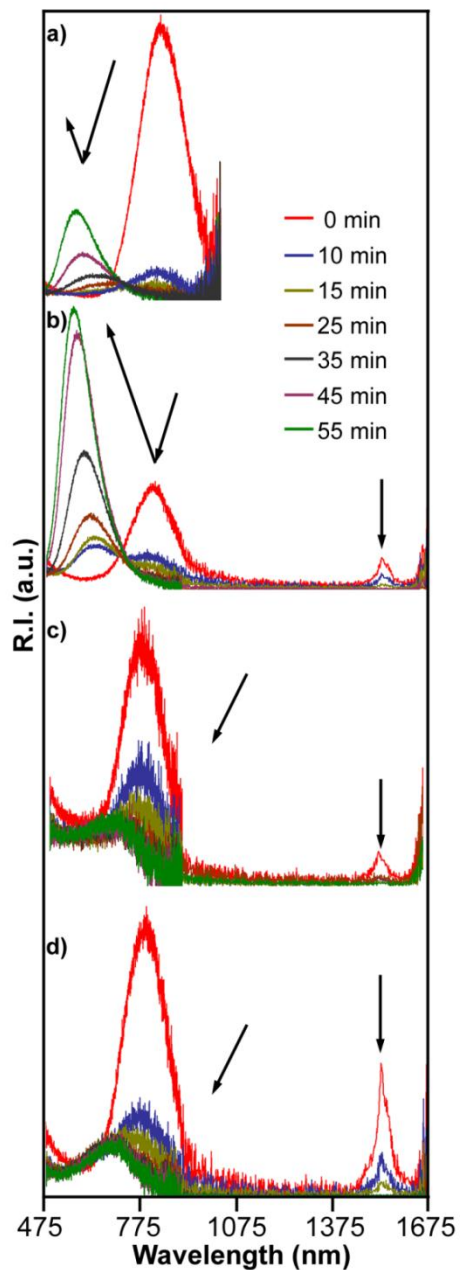


**Fig. 2.7** *In situ* HF etching of samples 13a (a), 4a (b), 8a (c), and 12a (d). Intensity changes upon etching are shown by the arrows. Erbium emission disappears after 15 minutes of etching, similar to the time it takes to remove the SiO<sub>2</sub> matrix in sample 13a (a). Comparison of the Si-NC luminescence intensity in (a) and (b) shows some of the NC energy is being transferred into the Er<sup>3+</sup>.

## 2.4. Conclusion

We have demonstrated that preparation of Er-doped composites containing Si nanodomains is readily prepared via thermal processing of hydrogen silsesquioxane and three different erbium precursors (i.e., ErCl<sub>3</sub>, ErA, and ErOct). Furthermore, we have found that the addition of dopant precursors and their properties (e.g., solubility and reactivity) dramatically influence the doping efficiency and crystallinity of the silicon nanodomains. All Er-doped composites show emission in the desired transparency window of SiO<sub>2</sub>-based fiber optics and removal of the oxide matrix via HF etching clearly demonstrates chemically that the sensitization process is active. This new found dopant-based control of nanodomain crystallinity and further tailoring of composites could lead to new, practical emissive materials based upon other luminescent centers.

## 2.5. References

- (1) Gambling, W. A. *IEEE J. Sel. Top. Quantum Electron.* **2000**, *6*, 1084.
- (2) *Optical Fiber Telecommunications V B: systems and networks*; 5th Edition ed., 2008.
- (3) Becker, P. C. O., N.A.; Simpson, J.R. *Erbium-Doped Fiber Amplifiers Fundamentals and Technology*; Academic Press: San Diego, 1999.
- (4) Kenyon, A. J. *Prog. Quantum Electron.* **2002**, *26*, 225.
- (5) Polman, A. *J. Appl. Phys.* **1997**, *82*, 1.
- (6) Priolo, F.; Franzo, G.; Coffa, S.; Carnera, A. *Phys. Rev. B* **1998**, *57*, 4443.
- (7) Monguzzi, A.; Trioni, M. I.; Tubino, R.; Milani, A.; Brambilla, L.; Castiglioni, C. *Synth. Met.* **2009**, *159*, 2410.
- (8) Polman, A. *Physica B* **2001**, *300*, 78.
- (9) Thyagarajan, K. G., A. *Fiber Optic Essential*; John Wiley & Sons: Hoboken, New Jersey, 2007.
- (10) Mears, R. J.; Baker, S. R. *Opt. Quantum Electron.* **1992**, *24*, 517.
- (11) Kenyon, A. J. *Semicond. Sci. Technol.* **2005**, *20*, R65.
- (12) Ishii, M.; Komuro, S.; Morikawa, T.; Aoyagi, Y. *J. Appl. Phys.* **2001**, *89*, 3679.
- (13) Adler, D. L.; Jacobson, D. C.; Eaglesham, D. J.; Marcus, M. A.; Benton, J. L.; Poate, J. M.; Citrin, P. H. *Appl. Phys. Lett.* **1992**, *61*, 2181.
- (14) Kovalev, D.; Diener, J.; Heckler, H.; Polisski, G.; Kunzner, N.; Koch, F. *Phys. Rev. B* **2000**, *61*, 4485.
- (15) Kik, P. G.; Polman, A. *J. Appl. Phys.* **2000**, *88*, 1992.
- (16) Fujii, M.; Yoshida, M.; Hayashi, S.; Yamamoto, K. *J. Appl. Phys.* **1998**, *84*, 4525.
- (17) Fujii, M.; Yoshida, M.; Kanzawa, Y.; Hayashi, S.; Yamamoto, K. *Appl. Phys. Lett.* **1997**, *71*, 1198.
- (18) Chryssou, C. E.; Kenyon, A. J.; Iwayama, T. S.; Pitt, C. W.; Hole, D. E. *Appl. Phys. Lett.* **1999**, *75*, 2011.
- (19) Franzo, G.; Vinciguerra, V.; Priolo, F. *Appl. Phys. A-Mater. Sci. Process.* **1999**, *69*, 3.
- (20) Franzo, G.; Boninelli, S.; Pacifici, D.; Priolo, F.; Iacona, F.; Bongiorno, C. *Appl. Phys. Lett.* **2003**, *82*, 3871.
- (21) Noe, P.; Okuno, H.; Jager, J. B.; Delamadeleine, E.; Demichel, O.; Rouviere, J. L.; Calvo, V.; Maurizio, C.; D'Acapito, F. *Nanotechnology* **2009**, *20*, 8.
- (22) Lenz, F.; DeCorby, R.; Meldrum, A. *Phys. Status Solidi A-Appl. Mat.* **2009**, *206*, 989.
- (23) Gourbilleau, F.; Dufour, C.; Madelon, R.; Rizk, R. *J. Lumines.* **2007**, *126*, 581.
- (24) Meldrum, A.; Hryciw, A.; MacDonald, A. N.; Blois, C.; Clement, T.; DeCorby, R.; Wang, J.; Li, Q. *J. Lumines.* **2006**, *121*, 199.

- (25) Kik, P. G.; Brongersma, M. L.; Polman, A. *Appl. Phys. Lett.* **2000**, *76*, 2325.
- (26) Izeddin, I.; Moskalenko, A. S.; Yassievich, I. N.; Fujii, M.; Gregorkiewicz, T. *Phys. Rev. Lett.* **2006**, *97*, 4.
- (27) Fujii, M.; Imakita, K.; Watanabe, K.; Hayashi, S. *J. Appl. Phys.* **2004**, *95*, 272.
- (28) Fujii, M.; Nakamura, T.; Miura, S.; Inui, M.; Hayashi, S. *Phys. Status Solidi A-Appl. Mat.* **2008**, *205*, 47.
- (29) Choy, K.; Lenz, F.; Liang, X. X.; Marsiglio, F.; Meldrum, A. *Appl. Phys. Lett.* **2008**, *93*, 3.
- (30) Ji, J. M.; Senter, R. A.; Tessler, L. R.; Back, D.; Winter, C. H.; Coffey, J. L. *Nanotechnology* **2004**, *15*, 643.
- (31) St John, J.; Coffey, J. L.; Chen, Y. D.; Pinizzotto, R. F. *J. Am. Chem. Soc.* **1999**, *121*, 1888.
- (32) Priolo, F.; Franzo, G.; Iacona, F.; Pacifici, D.; Vinciguerra, V. *Mater. Sci. Eng. B-Solid State Mater. Adv. Technol.* **2001**, *81*, 9.
- (33) Heng, C. L.; Chelomentsev, E.; Zalloum, O. H. Y.; Wojcik, J.; Mascher, P. *J. Vac. Sci. Technol. A* **2009**, *27*, 101.
- (34) Hessel, C. M.; Henderson, E. J.; Veinot, J. G. C. *Chem. Mat.* **2006**, *18*, 6139.
- (35) Hessel, C. M.; Summers, M. A.; Meldrum, A.; Malac, M.; Veinot, J. G. C. *Adv. Mater.* **2007**, *19*, 3513.
- (36) Rodriguez, J. R.; Veinot, J. G. C.; Bianucci, P.; Meldrum, A. *Appl. Phys. Lett.* **2008**, *92*, 131119.
- (37)
- (38) Bianucci, P.; Rodriguez, J. R.; Clements, C. M.; Veinot, J. G. C.; Meldrum, A. *J. Appl. Phys.* **2009**, *105*, 5.
- (39) Jaiswal, S. L.; Simpson, J. T.; Withrow, S. P.; White, C. W.; Norris, P. M. *Appl. Phys. A-Mater. Sci. Process.* **2003**, *77*, 57.
- (40) Panicia, M.; Koehl, S. *IEEE Spectr.* **2005**, *42*, 38.
- (41) Lu, T.; Yang, L.; van Loon, R. V. A.; Polman, A.; Vahala, K. J. *Opt. Lett.* **2009**, *34*, 482.
- (42) Mizutani, T.; Nagase, H.; Ogoshi, H. *Chem. Lett.* **1998**, 133.
- (43) Robinson, D. B.; Rognlien, J. L.; Bauer, C. A.; Simmons, B. A. *J. Mater. Chem.* **2007**, *17*, 2113.
- (44) Coradin, T.; Durupthy, O.; Livage, J. *Langmuir* **2002**, *18*, 2331.
- (45) Silverstein, R. M. W., F. X. *Spectrometric Identification of Organic Compounds*; 6th Edition ed.; John Wiley & Sons, Inc. , 1996.
- (46) Hessel, C. M.; Henderson, E. J.; Veinot, J. G. C. *J. Phys. Chem. C* **2007**, *111*, 6956.
- (47) Henderson, E. J.; Kelly, J. A.; Veinot, J. G. C. *Chem. Mat.* **2009**, *21*, 5426.
- (48) Domashevskaya, E. P.; Terekhov, V. A.; Kashkarov, V. M.; Manukovskii, E. Y.; Turishchev, S. Y.; Molodtsov, S. L.; Vyalykh, D. V.; Khokhlov, A. F.; Mashin, A. I.; Shengurov, V. G.; Svetlov, S. P.; Chalkov, V. Y. *Phys. Solid State* **2004**, *46*, 345.

(49) Holmes, J. D.; Ziegler, K. J.; Doty, R. C.; Pell, L. E.; Johnston, K. P.; Korgel, B. A. *J. Am. Chem. Soc.* **2001**, *123*, 3743.

# Chapter 3:

## Patterning of Silicon and Germanium Nanostructures

*A portion of this chapter has been accepted for publication:*

*Rodriguez Núñez, J. R.; Johnson, M.; Veinot, J. G. C. MRS Conference  
Proceedings*

### 3.1. Introduction

Semiconductor nanocrystals are of great interest partly because of their quantum confined luminescence.<sup>1,2</sup> Research into direct bandgap quantum dots (QDs) consisting of II-VI and III-V semiconductors has led to advances in synthetic methodologies and characterization techniques that facilitate understanding and manipulating the unique optical and material properties of 0-dimensional nanostructures.<sup>2-4</sup> Many applications have been suggested for QDs including, solar cell sensitizers, cellular probes, emissive materials suitable for lasers, among others.<sup>5-7</sup> While II-VI and III-V QDs laid much of the ground work for, and in many respects still lead the semiconductor nanocrystal field, the toxicity associated with heavy metals found in these systems is of great concern.<sup>8-</sup><sup>10</sup> Group IV semiconductors (i.e., silicon and germanium) are non-toxic and are thus generating increased interest as materials suitable for day-to-day consumer applications.<sup>11-16</sup> For example, luminescent silicon nanocrystals (Si-NCs) have been suggested as ideal light sources for optoelectronic computing applications because of their compatibility with existing silicon technologies.<sup>17</sup> The bulk bandgap of germanium of 0.67 eV (lying in the tissue transparent wavelength range) makes this material a promising candidate for cell labelling and photodynamic therapy.<sup>18</sup> Solvent dispersions of Ge-NCs have already been used as inks to deposit Ge thin films that could afford convenient ways to prepare printed electronic devices.<sup>19</sup>

Many suggested applications require nanoparticle (NP) patterning. For example, the development of silicon-based solid-state memory devices requires nanoparticles to be embedded in a gate dielectric layer.<sup>20</sup> If the nanocrystals are arranged appropriately, a device characterized by low-voltage operation with improved scalability and data retention properties can be realized.<sup>21,22</sup> The smaller bandgap of Ge-NCs may provide improved data retention and increase write/erase speeds in solid-state oxide-embedded Ge-NC (OE-GE-NC) non-volatile memory.<sup>23-25</sup> If these applications are to be realized, controllable patterning of Ge structures must first be developed.

Many techniques have been developed for patterning micro and nanostructures. Among them, lithography justifiably remains the technology of choice for existing industrial applications. The continued demand for smaller and faster electronic device structures will eventually require features at the limits of standard photolithography.<sup>26,27</sup> To answer the call for sub-50 nm features, other techniques such as e-beam lithography (EBL), and dip-pen nanolithography (DPN) have been developed and studied throughout the literature.<sup>28,29</sup> Although these physical patterning methods routinely give sub-50 nm patterns, the cost and speed benchmarks suggested by The International Technology Roadmap for Semiconductors (ITRS) may prove too demanding.<sup>30</sup> Block copolymer (BCP) templating has been studied as a low cost alternative to create structures in the nanometer dimension.<sup>31,32</sup> Although it does not offer the flexibility to pattern every desirable structure (i.e., writing characters on a surface achievable using EBL or DPN), it can access geometries such as dots, wires, and rods.<sup>32</sup> Self-

organizing diblock copolymer films have been described by the IBM Nanotechnology Research division as a “low cost, efficient means to engineer nanometer-scale structures over large wafer areas”.<sup>33</sup> The industrial importance of BCP patterning is evidenced by the integration of a polymer self-assembly process into a semiconductor fabrication facility at IBM Thomas J. Watson Research Center in New York. Non-lithographic patterning of metal nanoparticles using diblock copolymers has been demonstrated.<sup>34,35</sup> Patterning of semiconductor nanoparticles has been primarily performed using compound semiconductors of Group II-VI and III-V.<sup>36-38</sup>

Patterning of Group IV semiconductor nanoparticles is rarely reported in the literature. An important demonstration of this type of patterning came from our research group using hydrogen silsesquioxane (HSQ, a reported Si-NC precursor) and EBL.<sup>39</sup> Patterns of oxide embedded silicon nanocrystals (OE-Si-NCs) with dimensions as low as 7 nm were obtained.<sup>39</sup> These patterns exhibited heights of at least a few hundred nm and require expensive equipment used by highly trained personnel. Literature concerning BCP patterning of silicon and germanium nanostructures is limited at best, with the most notable examples being the formation of pit arrays by HF etching of a silicon substrate shown by Buriak et al. and patterning of insulating SiO<sub>2</sub>.<sup>40-43</sup> The lack of reports outlining patterning of Group IV semiconductor nanostructures using BCPs may result from limitations associated with the physical methods commonly used to prepare Si and Ge NPs (e.g., ion implantation, laser ablation, etc.);<sup>44-46</sup> these procedures are not compatible with BCP patterning. At first glance, colloidal methods to

prepare Si and Ge NPs appear promising for non-lithographic BCP patterning.<sup>47,48</sup> However the impact of the high temperatures and reactive nanoparticle precursors on BCP ordering can be unpredictable. Since 2006, the Veinot group has reported various methods for preparing Si and Ge NCs using sol-gel derived precursors.<sup>49-</sup><sup>52</sup> These synthetic methods use acid catalysis to yield silicon or germanium rich oxides (SROs, GROs) that can be thermally processed to produce crystalline silicon or germanium nanocrystals embedded in an oxide matrix. It is reasonable to suggest that BCPs will afford a convenient avenue for patterning group IV nanostructures if hydrolysis and condensation can be catalyzed by one of the blocks.

In the following chapter, a method for patterning silicon and germanium nanostructures using BCP templating is described. The BCP of choice for this study is commercially available polystyrene-*b*-poly-4-vinylpyridine (PS-*b*-P4VP). Upon dissolution in *m*-xylene, the immiscible blocks segregate; however, the covalent link between the two chemically dissimilar blocks forces nanoscale self-assembly. Scheme 3.1 shows self-assembly into a micelle, although other geometries are possible.<sup>53,54</sup> The PS domain forms a corona (the solubilized outer layer) and the P4VP unit the core (the compact inner layer).<sup>55</sup> The pyridine functionalities in the micelle can promote base-catalyzed crosslinking of the silicon and germanium precursors. This process leads to localized reactivity and patterned sol-gel arrays that can be thermally processed to yield Si- and Ge-based patterned nanostructures. Two precursors with different reactivities were utilized to highlight the versatility of this patterning technique: commercially available

hydrogen silsesquioxane (HSQ) and tetraethoxygermane (TEOG). After pyridine-mediated crosslinking, these structures can be thermally processed to produce silica features containing silicon nanoparticles, germania nanoparticles ( $\text{GeO}_2$ -NP), and germanium nanoparticles (Ge-NP) depending on precursors and processing conditions.

## 3.2. Experimental Details

### 3.2.1. Material preparation

#### 3.2.1.1. Solution preparation

##### 3.2.1.1.1. PS-b-P4VP and PS-b-PMMA

PS-b-P4VP and PS-b-PMMA polymers were purchased from Polymer Source Inc. Molecular weights for PS-b-P4VP polymers are shown in Table 3.1, molecular weight of PS-b-PMMA: 123000-b-35000. 0.5% *w/w* solutions were prepared using anhydrous *m*-xylene ( $\geq 99\%$ ) from Sigma Aldrich. The mixture was sonicated until a homogeneous cloudy solution was obtained and then stirred at 80 °C for at least 24 hours and left capped at ambient conditions for another 24 hours. Afterwards, the vials containing the BCP solution were covered with a Kimwipe and exposed to ambient conditions for at least one week to allow ambient water to wet the solutions.

**Table 3.1** Molecular weights of PS-b-P4VP polymers used for patterning of Group IV semiconductor nanostructures.

BCP	Molecular Weight, $M_n$ (PS-b-P4VP)	P.D.I. ( $M_w/M_n$ )
1	20000-b-17000	1.08
2	57500-b-18500	1.14
3	122000-b-22000	1.15
4	365000-b-34000	1.11

#### **3.2.1.1.2. Hydrogen Silsesquioxane (HSQ) solutions**

HSQ solution in methyl isobutyl ketone (MIBK) was obtained from Dow Corning Corporation under the tradename FOx XX (where XX denotes the weight percent). Solid HSQ can be obtained by solvent removal using standard Schlenk techniques. Solutions of 0.5% *w/w* HSQ in anhydrous *m*-xylene ( $\geq 99\%$  Sigma Aldrich) were prepared inside a glovebox ( $< 10$  ppm H<sub>2</sub>O and O<sub>2</sub>). Particulate was removed from the resulting clear solution using a 450  $\mu\text{m}$  PTFE filter.

#### **3.2.1.1.3. Tetraethoxygermane solutions**

Tetraethoxygermane was purchased from Gelest as a clear colourless liquid. 0.5% *w/w* TEOG : *m*-xylene mixtures were prepared in a glovebox ( $< 10$  ppm H<sub>2</sub>O and O<sub>2</sub>) and treated similarly to HSQ solutions.

#### **3.2.1.2. Patterning of silicon and germanium nanostructures**

HSQ/TEOG and BCP solutions were mixed in a vial under ambient conditions in the quantities outlined in Table 3.2. The solution was shaken for at least 1 minute before spin coating at 3000 rpm for 20 s. Silicon substrates have been used for Atomic Force Microscopy (AFM), Scanning Electron Microscopy (SEM) and Auger-Emission Spectroscopy (AES). Highly Ordered Pyrolytic Graphite (HOPG, SPI Supplies) was used as a substrate for XPS experiments.

**Table 3.2** Solutions used to produce OE-Si-NP and germanium patterns

<b>BCP</b>	<b>Volume 0.5% HSQ or TEOG (<math>\mu\text{L}</math>)</b>	<b>Volume 0.5% BCP (<math>\mu\text{L}</math>)</b>
1	25 (HSQ)	100
2	100 (TEOG)	100
3	100 (HSQ)	100
4	100 (HSQ)	100

### **3.2.1.3. Thermal Processing of Silicon nanostructures**

Substrates spin coated with HSQ and BCP were heated to 1100 °C for 1 h (heating rate 18 °C/min) under a 5% H<sub>2</sub>/95% Ar atmosphere.

### **3.2.1.4. Thermal Processing of Ge nanostructures**

Two heating profiles were used to prepare GeO<sub>2</sub> and Ge nanostructures. GeO<sub>2</sub> features are obtained by spin coating substrates with TEOG and BCP and heating under ambient atmosphere to 400 °C for 1 h (heating rate 9 °C/min). To obtain elemental Ge features, substrates were spin coated with TEOG and BCP and heated to 400 °C under ambient conditions to remove the block copolymer material. Subsequently, the heating tube was flushed with 20% H<sub>2</sub>/80% Ar for five minutes and maintained in the same atmosphere under a static atmosphere for the remainder of the process. Patterns were heated at 470 °C and 500 °C for one hour to study the effect of processing temperature on the composition and dimensions. Substrates were subsequently cooled to room temperature.

### **3.2.2. Material Characterization**

#### **3.2.2.1. Atomic Force Microscopy (AFM)**

Height images of Si and Ge patterns on silicon and silica substrates were collected using a Dimension 3100 Atomic Force Microscope from Digital Instruments using tapping mode. All images were collected using silicon tips purchased from Nanoworld (thickness: 4.6  $\mu\text{m}$ , length: 160  $\mu\text{m}$ , width: 45  $\mu\text{m}$ , resonance frequency: 285 kHz, force constant: 42 N/m).

#### **3.2.2.2. X-ray photoelectron spectroscopy (XPS)**

The XPS measurements for the Si and Ge nanostructures on HOPG were performed on an AXIS-165 spectrometers (Kratos Analytical) at the Alberta Centre for Surface Engineering and Science (ACSES), University of Alberta. The base pressure in the analytical chamber was lower than  $3 \times 10^{-8}$  Pa. Monochromatic Al  $K\alpha$  source ( $h\nu = 1486.6$  eV) was used at a power of 210 W. The analysis spot was 400 x 700  $\mu\text{m}$ . The resolution of the instrument is 0.55 eV for Ag 3d and 0.70 eV for Au 4f peaks. Survey scans were collected for binding energy from 1100 to 0 eV with analyzer pass energy of 160 eV and a step of 0.35 eV. For the high-resolution spectra the pass-energy was 20 eV with a step of 0.1 eV. Electron flooding was required to compensate the sample charging during the analysis.

OE-Si-NC and  $\text{GeO}_2$  patterns are stable under ambient conditions while Ge patterns can be easily oxidized after preparation. For XPS measurements, the

heating tube with the patterned substrates after heating was placed inside a glove box. The substrates were then prepared for XPS measurements and only briefly exposed to ambient atmosphere before being placed under ultra-high vacuum in the XPS chamber.

### **3.2.2.3. Scanning Electron Microscopy (SEM) and Auger Electron Spectroscopy (AES)**

SEM samples of Si patterns were coated with chromium using an Edwards Xenosput XE 200 coater. Secondary electron images were collected using a JEOL 6301F field emission SEM.

The SEM and Auger measurements of Ge patterns were carried out using JAMP-9500F Auger microprobe (JEOL) at the Alberta Centre for Surface Engineering and Science, University of Alberta. The instrument is equipped with a Schottky field emitter that produces electron probe diameter of about 3 to 8 nm at the sample. The accelerating voltage and emission current for both, the SEM and Auger imaging were 15 kV and 8 nA, respectively. The working distance was 24 mm. The sample was rotated 30 degree away from the primary electron beam to face the electron energy analyzer. M5 lens with 0.6% energy resolution was used for the Auger spectroscopy and imaging.

The Auger peak of Ge LMM (1147 eV) was selected for the mapping. The intensity of each pixel in the Auger image was calculated by  $(P - B)/B$ , where P and B were the peak and background intensity, respectively. Such intensity definition helps to reduce the edge effect of islands and dots. An auto probe

tracking technique was used to compensate for possible drifting of the image during the analysis as a result of power instabilities.

#### **3.2.2.4. Thermal Gravimetric Analysis (TGA)**

A Perkin Elmer Pyris 1 Thermogravimetric Analyzer was used to determine the behaviour of the BCPs when heated to high temperatures. All block copolymers used in the present study were heated under air and under 5% H<sub>2</sub>/95% Ar from 25 °C to 900 °C at a rate of 10 °C/minute and the change in mass was monitored.

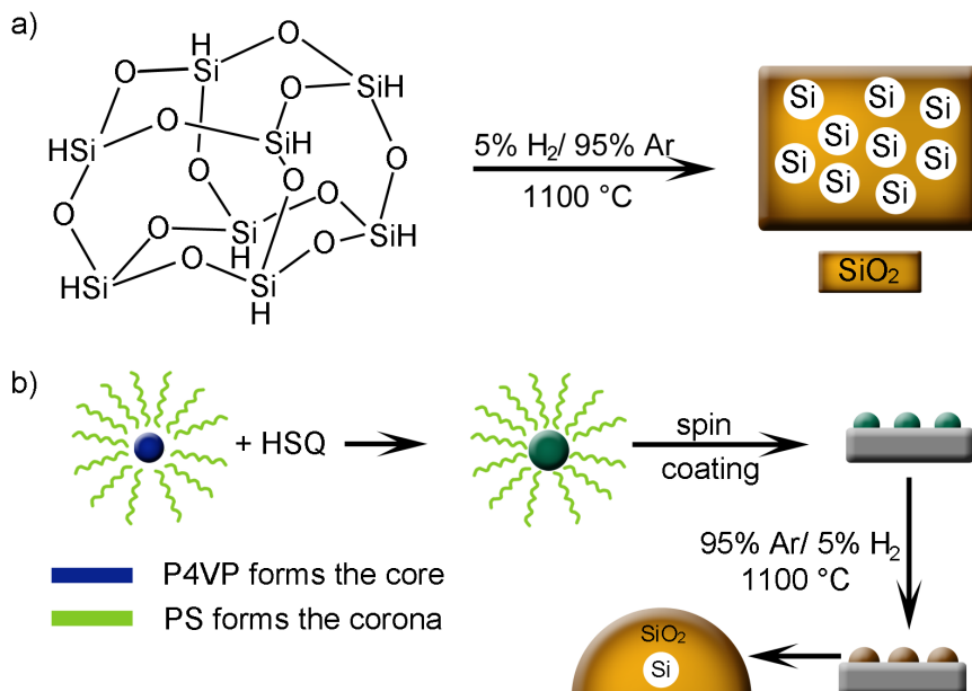
### **3.3. Results and Discussion**

#### **3.3.1. Patterning of Silicon Nanostructures**

There is considerable interest in structures with sub-100 nm dimensions because of the size dependent properties that occur at these dimensions. Two primary challenges become apparent: 1. preparing defect-free materials on the nanometer scale. 2. Achieving organized integration of these materials into a device. Physical methods (ion, implantation, laser ablation, magnetron sputtering) have been used by some, to produce well-characterized, defect-free, organized nanostructures.<sup>45,46,56</sup> Although these techniques have assisted the development of nanoscience, they remain costly and cumbersome to utilize. A bottom-up approach for creating nanostructures can yield materials with few defects, however, organizing them remains a challenge.<sup>47,57</sup> Non-lithographic techniques such as block-copolymer templating show potential for arranging nanostructures in ordered arrays necessary to bring many proposed nanomaterials applications to fruition.<sup>32</sup> BCPs have been used lithographically as masks but also non-lithographically to deposit nanoparticles and nanowires.<sup>58-60</sup> Curiously, there is a gap in the literature relating to BCP patterning of Group IV semiconductor nanostructures. Applications that utilize silicon and germanium nanoparticles are being intensely pursued due to their biocompatibility.<sup>13,14,18,61</sup> In addition, their size dependent bandgap (1.1 eV Si and 0.6 eV Ge in the bulk) spans the visible range and the low loss window of silica fiber optics, as well as the transparent

window of tissues, making them ideal candidates for biological, computing, and many optoelectronic applications.<sup>17,23,61</sup>

Our group employs thermal disproportionation of SROs to produce OE-Si-NCs. Commercially available HSQ, first synthesized by scarce water addition,<sup>62</sup> was initially marketed as an adhesive material and is currently marketed as a spin-on dielectric due to its gap-fill properties and solution processability.<sup>63</sup> HSQ can also be used to produce OE-Si-NCs upon thermal processing under slightly reducing atmosphere (Scheme 3.1.a).<sup>50</sup> In Chapter 2, it was discussed that HSQ solutions gel upon exposure to an amide containing Er<sup>3+</sup> precursor.<sup>64</sup> During this study it was discovered that HSQ gelation occurred when commercially available FOx solutions (HSQ dissolved in MIBK) were exposed to pyridine or ammonia gas. While a decrease in the Si-H signal was observed in FTIR and NMR spectra when HSQ is exposed to ErA, no apparent decrease of Si-H is observed upon exposure to NH<sub>3(g)</sub>. The luminescence of the thermally processed composites did not appear to be affected by NH<sub>3(g)</sub> induced reaction. Based on these observations, it is reasonable that nitrogen bases crosslink HSQ via oxidized Si-H moieties in the form of Si-OH present in the commercially available HSQ solution. PS-P4VP was chosen as a templating BCP expecting the pyridyl moiety will crosslink hydrogen silsesquioxane (Scheme 3.1.b).



**Scheme 3.1** a) Commercially available HSQ yields OE-Si-NCs upon thermal processing. b) PS-P4VP self-assembles into micelles which can crosslink HSQ. Upon thermal processing, the features are expected to contain Si-NPs embedded in a silica matrix.

The roles of the PS and P4VP domains for block-copolymer templating are well established.<sup>55,65</sup> In general, the molecular weight (MW) of the PS unit governs the core-core spacing between the pyridine domains. The MW of the P4VP unit controls the diameter of the deposited structures. This can be observed in AFM images of PS-*b*-P4VP BCPs spin-coated on silicon wafers (Figure 3.1). Solutions of HSQ and BCPs of different MWs were mixed and then spin coated on silicon substrates. The resulting coated silicon substrates were heated to 1100 °C under slightly reducing conditions to passivate defects in the NCs and remove the templating block copolymer. During crystal formation, the crystallinity of the

silicon nanodomains may be compromised by the presence of residual carbon. Nevertheless, non-crystalline silicon nanoparticles can still be luminescent and thus be useful for a variety of optoelectronic applications.<sup>66,67</sup>

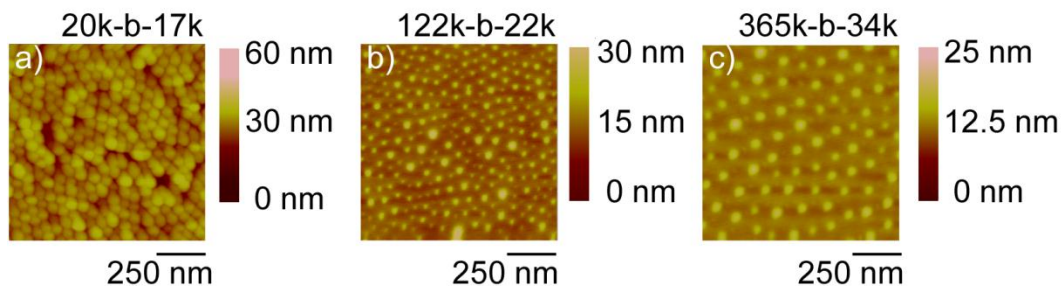


**Fig 3.1** AFM images of all PS-P4VP polymers used to pattern silicon nanoparticles. The features observed are due to the P4VP block segregating. The particle-to-particle spacing is directly proportional to the PS MW.

Upon thermally processing the silicon substrates, spin coated mixtures of HSQ and BCP 1, 3, and 4 (see Tables 3.1 and 3.2) surface patterns were obtained (Figure 3.2). Images obtained from thermally processing only BCP 4 (3.2.a) or HSQ (3.2.b) show no discernible pattern on the substrate after thermal processing. Figures 3.2.c,d,e,f show features on Si derived from thermally processed HSQ/BCP (BCP 1, 3, and 4, respectively) mixtures. Using AFM, the height, diameter, and particle-to-particle spacing were measured (Table 3.3). Dimensions measured by AFM afford height/diameter ratios ranging from 0.01 to 0.05 depending upon the BCP used. Based upon this ratio, these structures may be considered “nanodiscs”. The effect of MW is shown in Figures 3.2.d,e,f. As expected, increasing the MW of the PS-block increased the spacing between

discs. There was no measurable space when using 20k PS-block and the spacing increased to 57 nm (122k), and 103 nm (365k). The influence of the P4VP at first glance appeared erratic. The disc diameter decreased from 17k to 22k (Figure 3.2.d,e) and then increased from 22k to 34k (Figure 3.2.e,f and Table 3.3). An increase in diameter was expected with larger P4VP MW as observed when going from BCP 3 to BCP 4. The large features obtained using BCP 1 however, cannot be solely explained by the MW of P4VP. Two effects are possible in the case of BCP 1: 1) the small spacing between P4VP units in BCP 1 promotes gelation over several PVP domains, causing an increase in diameter; and/or 2) two or more features blend together during thermal processing, leading to an apparent increase in feature size.

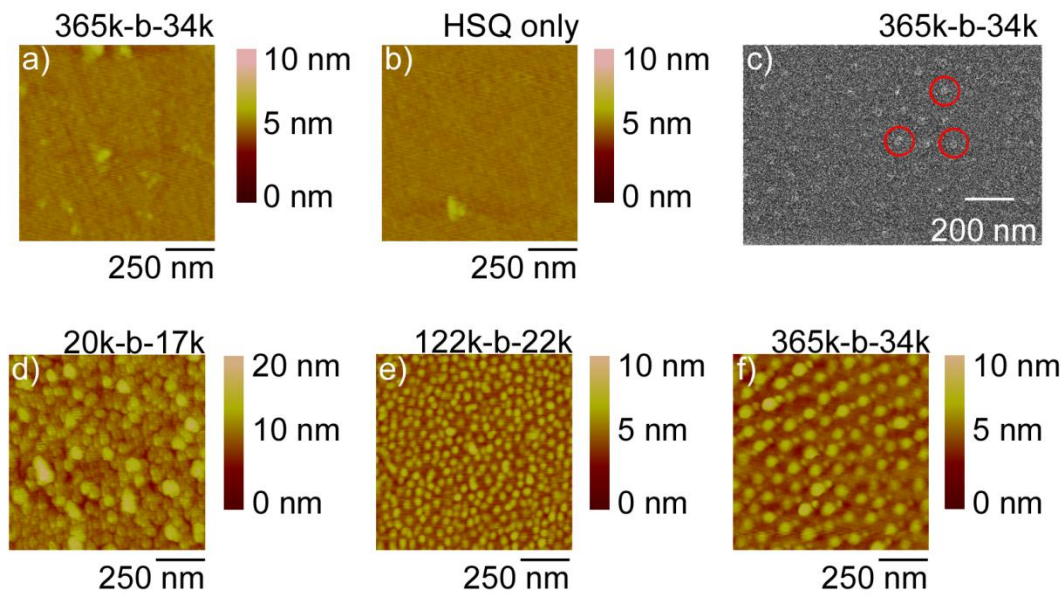


**Fig. 3.2** a) AFM of BCP 4 on Si, heated to 1100 °C in the absence of HSQ, b) HSQ spin coated on Si heated to 1100 °C in the absence of BCP, c) SEM of a pattern resulting from spin coating HSQ with BCP 4 after heating to 1100 °C, d) AFM of OE-Si-NPs patterns on Si with BCP 1, e) BCP 3, f) BCP 4.

**Table 3.3** Particle to particle spacing, particle diameter, and particle height of the resulting OE-Si-NP patterns

	<b>20k-b-17k</b>	<b>122k-b-22k</b>	<b>365k-b-34k</b>
Particle-to-particle spacing (nm)*	**	$29 \pm 4$	$52 \pm 6$
Diameter (nm)	**	$58 \pm 7$	$96 \pm 13$
Height (nm)	~2-3	$2 \pm 1$	$2 \pm 1$

\* Measured from particle center to particle center for accuracy.

\*\* Unable to measure due to small particle to particle spacing.

To determine the fate of the BCPs upon heating, thermal gravimetric analysis (TGA) was performed under air and under 5% H<sub>2</sub>/95% Ar. TGA of BCPs in air (Fig 3.3.a) will be discussed in Section 3.3.2 (Patterning of Ge nanostructures). TGA in 5% H<sub>2</sub>/95% Ar (Fig. 3.3.b) shows weight loss of the BCP samples at approximately 350 °C reaching 100% weight loss by 450 °C. This data suggests patterns derived from BCP/HSQ mixtures heated to 1100 °C will be primarily silicon and silica (after BCP evaporation).

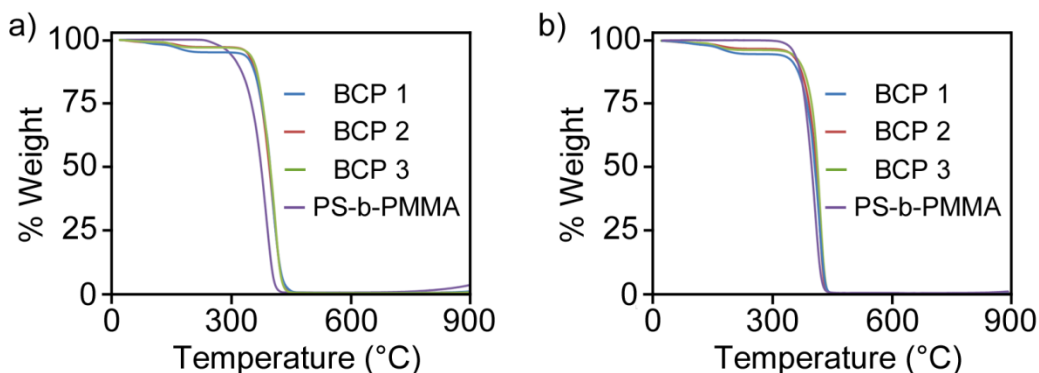


**Fig. 3.3** a) TGA of block copolymers heated under air and b) under 5 % H<sub>2</sub>/95 % Ar.

AFM images of patterns derived from HSQ and BCP 1 and 3 mixtures before and after heating give insight into the diameter increase observed for BCP 1 patterns and general pattern uniformity. Films of BCP 1/HSQ before heating were not uniform over large areas (Figure 3.4a and inset). Some areas have patterns while other areas do not have any features (only the silicon surface). This non-uniformity is common to spin coated polymers as they form liquid solid-interfaces.<sup>68</sup> Given the high density of reaction sites (low PS MW), regions of

high HSQ concentration can be removed during spin coating resulting in the formation of droplets that reduce the free energy of the system; this process is known as dewetting.<sup>69</sup> Large interfacial tension between the polar liquid film (high surface tension), and the non-polar substrate (low surface tension), leads to spontaneous removal of liquid, as the film thins. This process reduces liquid/substrate contact. Upon thermal processing, BCP 1/HSQ these droplets form islands containing patterns surrounded by areas with no features (Figure 3.4.b). It is worth noting that films derived from BCP 1/HSQ before heating show a feature diameter similar to BCP 1 without HSQ (Figure 3.4.a and 3.1.a). The diameter appears to increase (Figure 3.2.d) only after thermal processing, discounting the hypothesis that high density of crosslinking sites in BCP 1 is the only cause of feature diameter increase. Because there is no space between the features, it is possible that during thermal processing a quasi-liquid state is formed causing two or more features to blend together. As MW of PS is increased, the possibility of high density HSQ region formation decreases. Thus, when using BCP 4, the diameter is expected to remain the same and the pattern is should be uniform before and after heating. Figure 3.4 c,d confirms this hypothesis. Long range order is observed and the features do not appear to change drastically upon thermal processing.

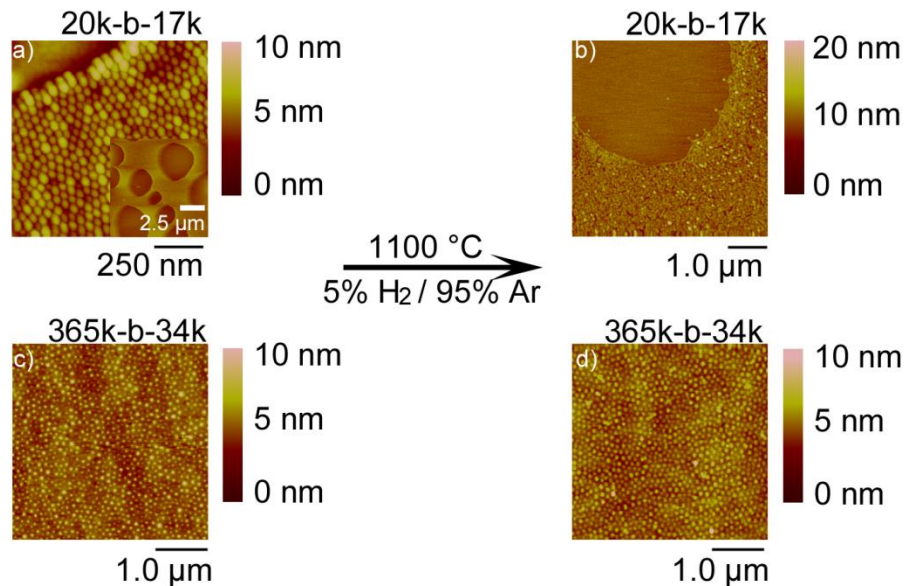


**Fig. 3.4** a) AFM images of BCP 1/HSQ features before heating (inset shows formation of islands) and b) after heating. c) AFM images of BCP 4/HSQ features before heating and b) after heating.

To characterize the composition of the patterns, a mixture of HSQ and BCP 3 was spin-coated on highly ordered pyrolytic graphite (HOPG) and heated to 1100 °C under 5% H<sub>2(g)</sub>. X-ray photoelectron spectroscopy (XPS) of the patterned HOPG substrate was obtained. A representative XP spectrum that shows two distinctive emissions is shown in Figure 3.5. After calibrating to the C1s emission (284.8 eV), the emissions are centered at 103.8 eV (characteristic of silicon oxides (Si (IV) 2p<sub>3/2</sub>)), and at 99.6 eV (characteristic of native silicon (Si (0) 2p<sub>3/2</sub>)). These values coincide with the binding energies reported for oxide embedded silicon nanocrystals derived from HSQ after heating to 1100 °C for 2 or more hours.<sup>70</sup> This Si(0) binding energy can be correlated to nanoparticle size for nanocrystalline systems; as the nanocrystal size increases the Si(0) binding

energy shifts to lower values until it converges at the energy of bulk silicon (98.7 eV).<sup>70</sup> Unfortunately, at this point, the crystallinity of the Si(0) particles is unclear, thus a correlation with size is not possible. If the particles are spherical, the height of the polymer will constrain the diameter of the features to less than 3 nm.

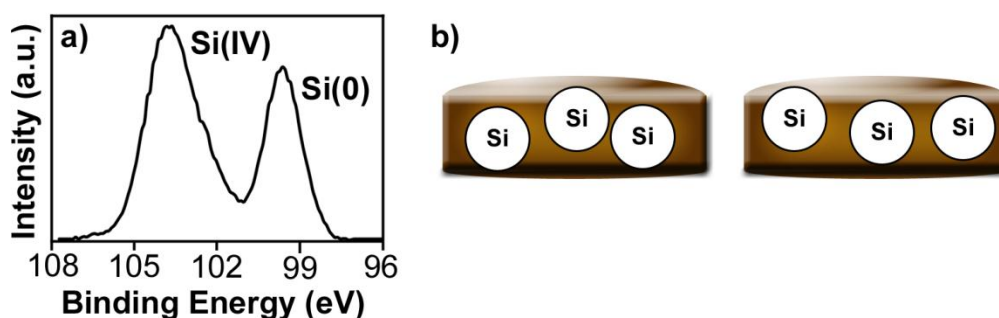


**Fig. 3.5** a) XP spectrum obtained from an HOPG substrate patterned with BCP 3 and HSQ after heating. b) Expected structure and composition of patterned features.

One aspect of nanodiscs of OE-Si-NPs that makes them particularly interesting is the limited number of nanocrystals in each feature. In addition, control over nanodisc diameter and spacing could allow investigation of interactions between NPs (e.g., tunnelling or energy transfer).<sup>71</sup> Photoluminescence (PL) measurements were attempted using a 325 nm He/Cd laser as an excitation source and light was collected using a fiber optic attached to a detector (See chapters 2 and 4 for a complete description of the PL setup). Unfortunately, no measurable PL was obtained. Given the low luminescence intensity that is expected from a film 2-3 nm in height, this observation is not

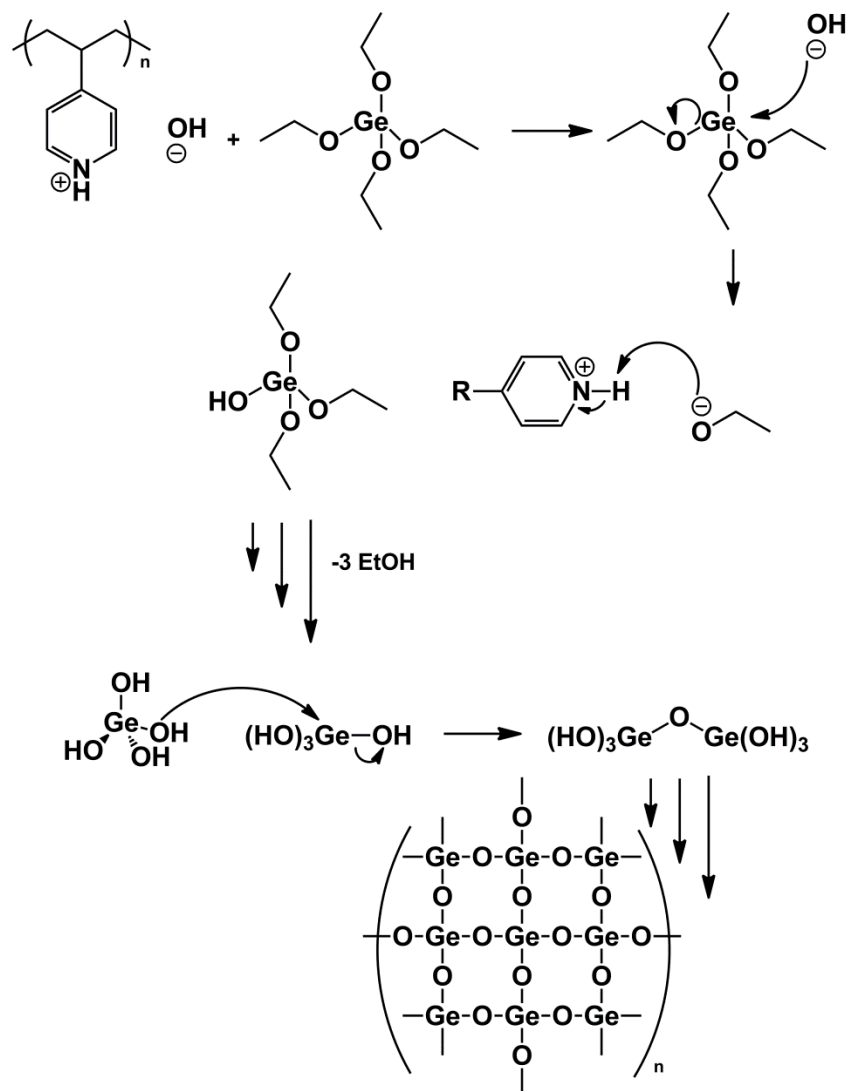
surprising. Other techniques such as Near-Field Optical Microscopy (NSOM) are being investigated to measure photoluminescence of the patterns.

### 3.3.2. Patterning of Germanium Nanostructures

Sol-gel reactions are commonly utilized to make nanostructures due to the exquisite tunability of this synthetic method. Titania nanotubes, SiC nanocrystals, and many other structures have been synthesized using sol-gel chemistry.<sup>51,72</sup> Coupling the versatility of this synthetic technique with a method to pattern the obtained structures could have important technological consequences. The following section will outline a method to produce and pattern sol-gel derived GeO<sub>2</sub> nanostructures. These structures can then be transformed into Ge under thermally reducing conditions. Tetraethoxygermane was chosen as a GeO<sub>2</sub> precursor. Solutions of tetraethoxygermane in m-xylene were mixed with BCP solutions of PS-b-P4VP, in which the pyridyl moieties are expected to catalyze crosslinking of TEOG via hydrolysis and condensation yielding an extended polymer with GeO<sub>2</sub> stoichiometry. A mechanistic study of hydrolysis and condensation of trimethylethoxysilane (TMES) using different amines as catalysts was reported in 2005 by Delak and Sahai, giving credence to the choice of pyridine-containing polymers for sol-gel reactions.<sup>73</sup> The authors observed the rate of hydrolysis and condensation increases as the number of nitrogen atoms increases in a polyamine ( $k_{\text{hyd/con}}$  tetraethylenepentamine >  $k_{\text{hyd/con}}$  1,4-diaminobutane). They also noted that basicity is inversely proportional to the rate

of hydrolysis and condensation ( $k_{\text{hyd/con}}$  pyridine,  $\text{pKa } 5.63 > k_{\text{hyd/con}}$  piperidine,  $\text{pKa } 11.24$ ).<sup>73</sup> These observations underline the high rates expected from P4VP.

Block copolymer solutions are exposed to ambient conditions prior to patterning experiments to allow water from the atmosphere to localize in the P4VP domain. Pyridine can abstract a proton from water producing  $\text{OH}^-$ , which can react with TEOG forming Ge-OH and ethanol (upon proton removal from pyridine). Once  $\text{Ge}(\text{OH})_4$  is formed, condensation proceeds releasing catalytic  $\text{OH}^-$  (See Scheme 3.2).



**Scheme 3.2** Suggested crosslinking mechanism for TEOG crosslinking in the presence of P4VP.

The effect of processing temperature on feature dimensions was studied using BCP 3/TEOG heated to 350 and 500 °C (Figure 3.6). In these samples, the feature diameter and height appeared to depend upon processing temperature. At 350 °C (Fig. 3.6.a.), the features were wider and higher. When the substrates were heated to 500 °C (Fig. 3.6.b) the particle-to-particle spacing increased and

the diameter decreased. It is possible that the  $\text{GeO}_2$  features partially evaporate at temperatures higher than  $350\text{ }^\circ\text{C}$ . Although Figure 3.3.a shows BCPs were not removed completely at  $350\text{ }^\circ\text{C}$ , the temperature fluctuation during heating ( $\pm 5\text{-}10\text{ }^\circ\text{C}$ ) and the prolonged heating, removed most of the polymer (Fig. 3.6.c). A representative AFM image from BCP 3 heated to  $350\text{ }^\circ\text{C}$  is shown in Figure 3.6.c. This image suggests that the features observed at temperatures higher than  $350\text{ }^\circ\text{C}$ , made from BCP3/TEOG do not contain any block copolymer.

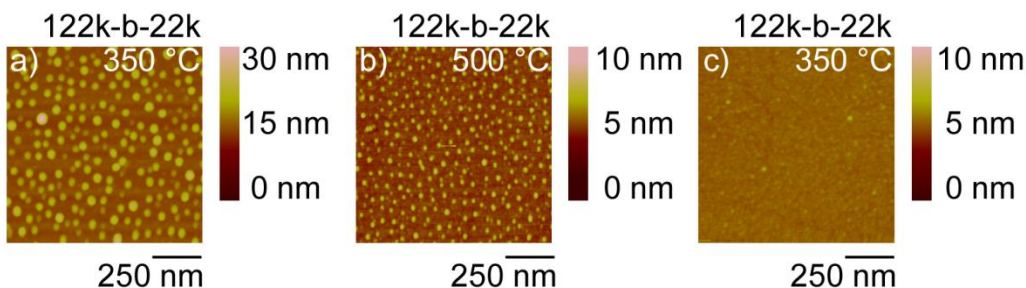


**Fig. 3.6** a) BCP 3/TEOG patterns heated to  $350\text{ }^\circ\text{C}$  and b)  $500\text{ }^\circ\text{C}$ . c) BCP 3 heated to  $350\text{ }^\circ\text{C}$  without TEOG.

In order to ensure complete formation of a polymer with  $\text{GeO}_2$  stoichiometry and removal of any trace BCP, a two-step heating method was performed. First, patterned substrates were heated to  $400\text{ }^\circ\text{C}$  under ambient conditions to ensure formation of  $\text{GeO}_2$  and removal of the block-copolymer. The substrate temperature was maintained at  $400\text{ }^\circ\text{C}$  for 15 minutes and then rapidly ( $\sim 2$  minutes) heated to  $470\text{ }^\circ\text{C}$  or  $500\text{ }^\circ\text{C}$  under a flow of 20%  $\text{H}_2/80\%$  Ar gas. XP spectra and AFM images of the resulting substrates are shown in Figure 3.7. After heating under ambient conditions to  $400\text{ }^\circ\text{C}$  (Fig. 3.7.d) the features had an average diameter of  $56\text{ nm}$  and height of  $\sim 8\text{ nm}$  (Table 3.4). After heating to  $470$

°C a substantial decrease in height and small decrease in diameter were observed. If hydrolysis and condensation did not proceed to completion, the evaporation of uncondensed, low molecular weight germanium oxide polymer could provide an explanation for the decrease in size observed between 400 °C and 470 °C. The substrates were heated under static reducing conditions to address issues arising from pattern evaporation at high temperatures. It is also possible that collapse of the structure during heating can cause the observed changes. Above 470 °C, the height and diameter do not change appreciably. A representative secondary electron SEM image of a sample prepared using BCP 2 and TEOG heated to 470 °C is shown in Figure 3.7.c. The image clearly shows the small features similar to those observed by AFM. The composition of the surface was studied using XPS. A representative XP spectrum of a substrate heated to 470 °C (Fig. 3.7.a) shows two peaks, one at 30.2 eV characteristic of Ge<sup>(0)</sup> and another one at 33.4 eV arising from oxidized germanium Ge. Once the sample was heated to 500 °C all of the oxide was reduced to Ge<sup>(0)</sup> as evidenced by the XP spectrum in Figure 3.7.b. The small oxide emission observed is attributed to ambient exposure of sample during XPS sample preparation.

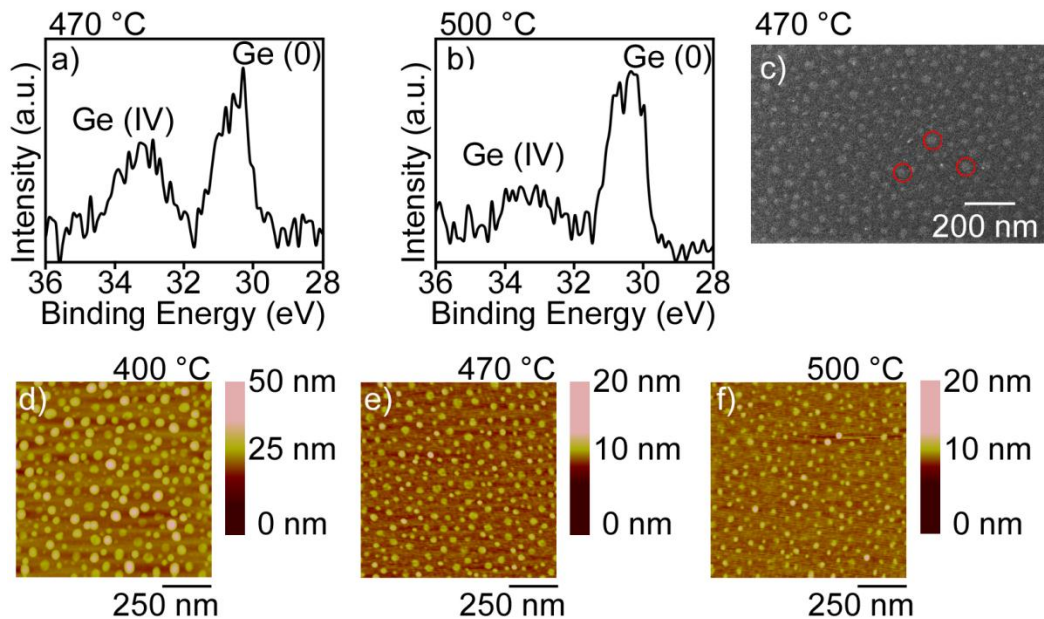


**Fig. 3.7** XPS spectra of substrates patterned with BCP 2 and TEOG after heating to a) 470 °C and to b) 500 °C and their corresponding AFM images (e and f, respectively). c) Characteristic SEM image of a patterned substrate using BCP2/TEOG on Si heated to 470 °C. d) Characteristic AFM image of a substrate patterned using BCP 2 and TEOG heated to 400 °C.

**Table 3.4** Particle height and diameter of patterns heated to 400 °C, 470 °C, and 500 °C.

	400 °C	470 °C	500 °C
Particle Height (nm)	$8 \pm 2$	$2 \pm 1$	$2 \pm 1$
Particle Diameter (nm)	$56 \pm 9$	$49 \pm 8$	$48 \pm 9$

In order to obtain information about the composition of single features, Auger-electron spectroscopy was utilized (AES). The features of a sample heated to 470 °C were too small and no signal was obtained from point measurements or mapping. AES of patterns heated to 400 °C have features that are four times higher (See Table 3.4) and were expected to be better candidates for AES measurements. A secondary SEM image of a BCP2/TEOG pattern on silicon is shown in Figure 3.8.a. Mapping of the pattern in Figure 3.8.a resulted in no measurable signal. Point measurements were performed in three areas of the sample (Figure 3.8.a,b): point 1 on a large bright feature observable via SEM, point 2 on a nanodisc, and point 3, in an area where no discs are present. Figure 3.8.c shows a clear peak at ~1140 eV characteristic of Ge from point 1 (green trace) and other minor peaks at approximately 1040 eV also attributable to Ge. The second point (blue trace) shows a very weak peak at 1140 eV confirming that the patterns routinely observed contain Ge. Point 3 has no detectable Ge signal (red trace). From the XPS and AES data obtained it is reasonable that the nanodiscs observed after heating to 500 °C contain elemental Ge. These structures are being further investigated by our group as islands for galvanic displacement of metals to form semiconductor-metal heterostructures which may have interesting conductive properties.<sup>35</sup>

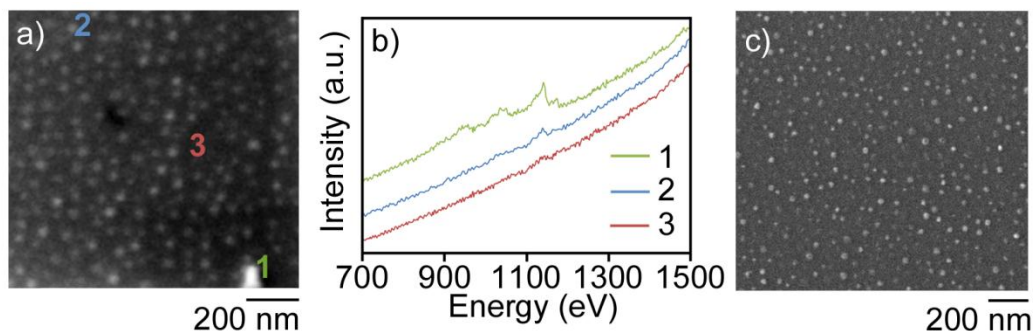


**Fig. 3.8** a) Secondary electron SEM image showing patterns obtained from heating a sample of TEOG and BCP 2 to 400 °C. b) AES point measurements of the areas shown in a). c) High resolution SEM confirming the presence of features on the substrate.

The chemical makeup (i.e., functional groups) of the BCP used is pivotal to the formation of Ge nanostructures. The general presented mechanism highlights the need for a base (or an acid) to catalyze the sol-gel crosslinking of TEOG. To confirm the importance of the block functionalities, patterning was attempted using a BCP that cannot catalyze hydrolysis and condensation. It is well known that diblock polystyrene-*b*-polymethyl(methacrylate) (PS-*b*-PMMA, Fig. 3.9.b) self-assembles to form micelles in non-polar solvents (e.g., xylene). Upon spin coating, these polymers can produce features similar to those obtained using PS-*b*-P4VP (Figure 3.9.c). When a substrate patterned using PS-*b*-PMMA was heated to 500 °C using the two step heating method no pattern was observed (Figure 3.9.d). Similarly, no pattern was obtained (Figure 3.9.e) when a PS-*b*-PMMA/TEOG mixture is spin coated and heated to 500 °C using the two step method (heating under air to 400 °C followed by heating under reducing

conditions at 500 °C). This observation highlights the importance of the BCP used on patterning and at first it appears to limit this patterning method. It may be however possible to use PS-*b*-PMMA diblock-copolymers by adding a “loading step”. In this step, an added base or acid localized in the polar PMMA cores may be able to catalyze hydrolysis and condensation of sol-gel precursors. Our group is currently studying PS-*b*-PMMA micelles loaded with HCl<sub>(aq)</sub> as nanoreactors for TEOG crosslinking.

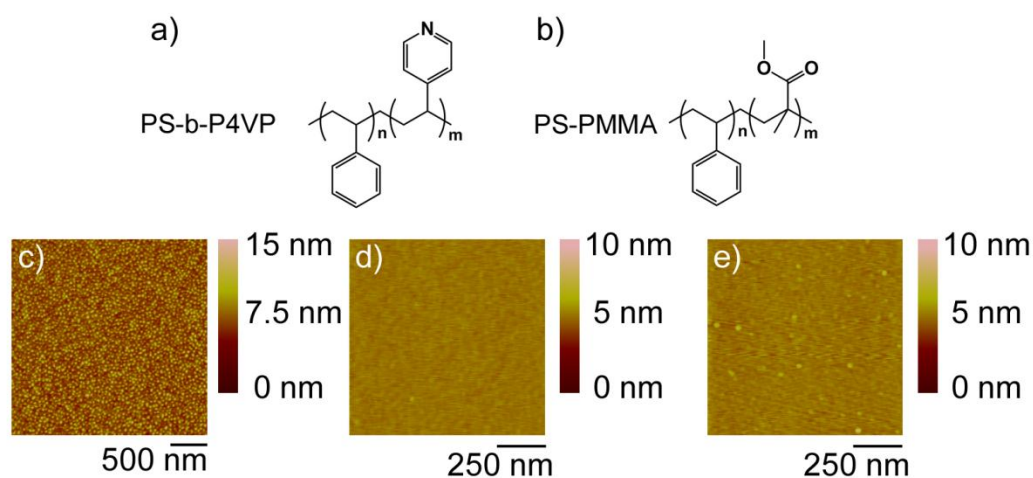


**Fig. 3.9** Structure of a) PS-P4VP and b) PS-PMMA, the pyridyl moiety can act as a catalytic base in sol gel polymerization. c) Patterned substrate using PS-PMMA, d) Resulting surface after two step heating PS-*b*-PMMA patterned substrate. e) Representative AFM image of a substrate patterned using TEOG/PS-*b*-PMMA heated using two-step process.

### 3.4. Conclusions

In this chapter a proof-of-concept method for patterning oxide-embedded silicon nanoparticles, germania nanodiscs and germanium nanodiscs is reported. BCPs containing P4VP are key to this templating method as they serve to crosslink HSQ and to catalyze sol-gel hydrolysis and condensation of TEOG.

OE-Si-NPs are patterned using PS-b-P4VP and HSQ. As was reported in Chapter 2, amines are observed to crosslink HSQ. Pyridyl moieties in P4VP act as nano-reactors which crosslink hydrogen silsesquioxane. After thermal processing, HSQ disproportionates to form nanodiscs made of Si-NPs in a silica matrix as characterized by XPS and AFM. The optical properties of the pattern could not be assessed due to the small dimension of the features (height < 3 nm, width ~50-100 nm).

Germanium patterns were obtained using the P4VP nanoreactors to catalyze the hydrolysis and condensation of TEOG. Pyridine is a known catalyst for sol-gel reactions of silanes and the mechanism was thoroughly studied by Delak and Sahai.<sup>73</sup> Upon hydrolysis and condensation of TEOG in the presence of catalytic P4VP a polymer of oxidized germanium is obtained. Heating causes a drastic decrease in feature height and diameter, providing a method to alter feature size by simply adjusting the temperature. In order to remove the polymer fully and promote crosslinking of TEOG, a two-step heating method was introduced. First, the patterned substrate was heated to 400 °C under ambient atmosphere and then heated to 470 °C or 500 °C under reducing static atmosphere of 20% H<sub>2</sub>/80%

Ar. The oxidized germanium features are reduced to elemental Ge by this treatment. At 470 °C some oxidized germanium was still present. However, once the temperature reaches 500 °C, all of the oxide was reduced. Point measurements using AES on patterns derived from BCP/TEOG heated to 400 °C confirmed the presence of Ge nanodiscs. Using PS-b-PMMA to template Ge structures highlights the importance of the basic pyridyl moieties, as no patterns are observed after heating to 500 °C

The demonstrated patterning method can be beneficial when trying to develop solid-state memory devices that require nanostructures to be patterned in a regular order. Characterization of the optical properties of Si-NCs patterns may also provide an insight into particle-particle interaction. Measurement of luminescence may be obtained using sensitive techniques such as near-field scanning optical microscopy. Determining the crystallinity of Ge and Si nanostructures may also be of interest to elucidate their optical properties. Crystallinity can also be studied using selected-area electron diffraction (SAED) of microtomed samples in a transmission electron microscope (TEM).

### 3.5. References

- (1) Nirmal, M.; Brus, L. *Acc. Chem. Res.* **1999**, *32*, 407.
- (2) Alivisatos, A. P. *J. Phys. Chem.* **1996**, *100*, 13226.
- (3) Sugawara, H.; Ishikawa, M.; Hatakoshi, G. *Applied Physics Letters* **1991**, *58*, 1010.
- (4) Dabbousi, B. O.; Rodriguez-Viejo, J.; Mikulec, F. V.; Heine, J. R.; Mattoussi, H.; Ober, R.; Jensen, K. F.; Bawendi, M. G. *Journal of Physical Chemistry B* **1997**, *101*, 9463.
- (5) Alivisatos, A. P.; Gu, W.; Larabell, C. In *Annu. Rev. Biomed. Eng.* 2005; Vol. 7, p 55.
- (6) Kazes, M.; Lewis, D. Y.; Banin, U. *Adv. Funct. Mater.* **2004**, *14*, 957.
- (7) Minot, E. D.; Kelkensberg, F.; Van Kouwen, M.; Van Dam, J. A.; Kouwenhoven, L. P.; Zwiller, V.; Borgström, M. T.; Wunnicke, O.; Verheijen, M. A.; Bakkers, E. P. A. M. *Nano Lett.* **2007**, *7*, 367.
- (8) Lewinski, N.; Colvin, V.; Drezek, R. *Small* **2008**, *4*, 26.
- (9) Sinha, P.; Kriegner, C. J.; Schew, W. A.; Kaczmar, S. W.; Traister, M.; Wilson, D. J. *Energy Policy* **2008**, *36*, 381.
- (10) Deaves, M. *Manuf. Eng.* **2004**, *83*, 12.
- (11) Slawson, R. M.; Van Dyke, M. I.; Lee, H.; Trevors, J. T. *Plasmid* **1992**, *27*, 72.
- (12) Fan, J.; Chu, P. K. *Small* **2010**, *6*, 2080.
- (13) Anglin, E. J.; Cheng, L.; Freeman, W. R.; Sailor, M. J. *Adv. Drug. Deliv. Rev.* **2008**, *60*, 1266.
- (14) Park, J. H.; Gu, L.; Von Maltzahn, G.; Ruoslahti, E.; Bhatia, S. N.; Sailor, M. J. *Nat. Mater.* **2009**, *8*, 331.
- (15) Alsharif, N. H.; Berger, C. E. M.; Varanasi, S. S.; Chao, Y.; Horrocks, B. R.; Datta, H. K. *Small* **2009**, *5*, 221.
- (16) Ruizendaal, L.; Bhattacharjee, S.; Pournazari, K.; Rosso-Vasic, M.; De Haan, L. H. J.; Alink, G. M.; Marcelis, A. T. M.; Zuilhof, H. *Nanotoxicology* **2009**, *3*, 339.
- (17) Paniccia, M.; Koehl, S. *IEEE Spectrum* **2005**, *42*, 30.
- (18) Lambert, T. N.; Andrews, N. L.; Gerung, H.; Boyle, T. J.; Oliver, J. M.; Wilson, B. S.; Han, S. M. *Small* **2007**, *3*, 691.
- (19) Holman, Z. C.; Kortshagen, U. R. *Nano Lett.* **2011**, *11*, 2133.
- (20) Guarini, K. W.; Black, C. T.; Zhang, Y.; Babich, I. V.; Sikorski, E. M.; Gignac, L. M. In *Technical Digest - International Electron Devices Meeting*, p 541.
- (21) De Blauwe, J. *IEEE T. Nanotechnol.* **2002**, *1*, 72.
- (22) King, Y. C.; King, T. J.; Hu, C. *IEEE T. Electron Dev.* **2001**, *48*, 696.
- (23) Kanoun, M.; Buseret, C.; Poncet, A.; Souifi, A.; Baron, T.; Gautier, E. *Solid State Electron.* **2006**, *50*, 1310.

- (24) Batra, Y.; Kabiraj, D.; Kanjilal, D. *Solid State Commun.* **2007**, *143*, 213.
- (25) Kanjilal, A.; Hansen, J. L.; Gaiduk, P.; Larsen, A. N.; Cherkashin, N.; Claverie, A.; Normand, P.; Kapelanakis, E.; Skarlatos, D.; Tsoukalas, D. *Appl. Phys. Lett.* **2003**, *82*, 1212.
- (26) Ito, T.; Okazaki, S. *Nature* **2000**, *406*, 1027.
- (27) Harriott, L. R. *P. IEEE* **2001**, *89*, 366.
- (28) Broers, A. N. *IBM J. Res. Dev.* **1988**, *32*, 502.
- (29) Piner, R. D.; Zhu, J.; Xu, F.; Hong, S.; Mirkin, C. A. *Science* **1999**, *283*, 661.
- (30) Arden, W. M. *Curr. Opin. Solid State Mater. Sci.* **2002**, *6*, 371.
- (31) Darling, S. B. *Prog. Polym. Sci.* **2007**, *32*, 1152.
- (32) Hamley, I. W. *Nanotechnology* **2003**, *14*, R39.
- (33) Black, C. T.; Ruiz, R.; Breyta, G.; Cheng, J. Y.; Colburn, M. E.; Guarini, K. W.; Kim, H. C.; Zhang, Y. *IBM J. Res. Dev.* **2007**, *51*, 605.
- (34) Hwang, Y. K.; Lee, J. M.; Sathaye, S. D.; Cho, G.; Hwang, J. S.; Chang, J. S. *J. Nanosci. Nanotechnol.* **2006**, *6*, 1850.
- (35) Aizawa, M.; Buriak, J. M. *Chem. Mater.* **2007**, *19*, 5090.
- (36) Seo, I.; Lee, D. J.; Hu, Q.; Kwon, C. W.; Lim, K.; Lee, S. H.; Kim, H. M.; Kim, Y. S.; Lee, H. H.; Ryu, D. Y.; Kim, K. B.; Yoon, T. S. *Electrochem. Solid-State Lett.* **2010**, *13*, K19.
- (37) Wang, C. W.; Moffitt, M. G. *Chem. Mater.* **2005**, *17*, 3871.
- (38) Park, J. H.; Kirch, J.; Mawst, L. J.; Liu, C. C.; Nealey, P. F.; Kuech, T. F. *Appl. Phys. Lett.* **2009**, *95*.
- (39) Hessel, C. M.; Summers, M. A.; Meldrum, A.; Malac, M.; Veinot, J. G. C. *Adv. Mater.* **2007**, *19*, 3513.
- (40) Wei, W.; Xu, H.; Qu, X.; Ji, X.; Jiang, W.; Yang, Z. *Macromol. Rapid Commun.* **2007**, *28*, 1122.
- (41) Zhang, X.; Qiao, Y.; Xu, L.; Buriak, J. M. *ACS Nano* **2011**, *5*, 5015.
- (42) Yinghong, Q.; Dong, W.; Buriak, J. M. *Nano Lett.* **2007**, *7*, 464.
- (43) Tseng, W. H.; Chen, C. K.; Chiang, Y. W.; Ho, R. M.; Akasaka, S.; Hasegawa, H. *J. Am. Chem. Soc.* **2009**, *131*, 1356.
- (44) Heinig, K. H.; Schmidt, B.; Markwitz, A.; Grötzschel, R.; Strobel, M.; Oswald, S. *Nucl. Instrumen. Meth. B* **1999**, *148*, 969.
- (45) Meldrum, A.; Haglund Jr, R. F.; Boatner, L. A.; White, C. W. *Adv. Mater.* **2001**, *13*, 1431.
- (46) Gourbilleau, F.; Portier, X.; Ternon, C.; Voivenel, P.; Madelon, R.; Rizk, R. *Appl. Phys. Lett.* **2001**, *78*, 3058.
- (47) Pettigrew, K. A.; Liu, Q.; Power, P. P.; Kauzlarich, S. M. *Chem. Mater.* **2003**, *15*, 4005.
- (48) Lee, D. C.; Pietryga, J. M.; Robel, I.; Werder, D. J.; Schaller, R. D.; Klimov, V. I. *J. Am. Chem. Soc.* **2009**, *131*, 3436.
- (49) Henderson, E. J.; Kelly, J. A.; Veinot, J. G. C. *Chem. Mater.* **2009**, *21*, 5426.

- (50) Hessel, C. M.; Henderson, E. J.; Veinot, J. G. C. *Chem. Mater.* **2006**, *18*, 6139.
- (51) Kelly, J. A.; Henderson, E. J.; Veinot, J. G. C. *Chem. Commun.* **2010**, 46, 8704.
- (52) Henderson, E. J.; Hessel, C. M.; Veinot, J. G. C. *J. Am. Chem. Soc.* **2008**, *130*, 3624.
- (53) Ruokolainen, J.; Saariaho, M.; Ikkala, O.; Ten Brinke, G.; Thomas, E. L.; Torkkeli, M.; Serimaa, R. *Macromolecules* **1999**, *32*, 1152.
- (54) Cho, J.; Hong, J.; Char, K.; Caruso, F. *J. Am. Chem. Soc.* **2006**, *128*, 9935.
- (55) Aizawa, M.; Buriak, J. M. *J. Am. Chem. Soc.* **2005**, *127*, 8932.
- (56) Orii, T.; Hirasawa, M.; Seto, T. *Appl. Phys. Lett.* **2003**, *83*, 3395.
- (57) Zhang, X.; Neiner, D.; Wang, S.; Louie, A. Y.; Kauzlarich, S. M. *Nanotechnology* **2007**, *18*.
- (58) Chai, J.; Buriak, J. M. *ACS Nano* **2008**, *2*, 489.
- (59) Zhang, J.; Gao, Y.; Hanrath, T.; Korgel, B. A.; Buriak, J. M. *Chem. Commun.* **2007**, 1438.
- (60) Park, M.; Harrison, C.; Chaikin, P. M.; Register, R. A.; Adamson, D. H. *Science* **1997**, *276*, 1401.
- (61) Erogbogbo, F.; Yong, K. T.; Roy, I.; Xu, G. X.; Prasad, P. N.; Swihart, M. T. *ACS Nano* **2008**, *2*, 873.
- (62) Frye, C. L.; Collins, W. T. *J. Am. Chem. Soc.* **1970**, *92*, 5586.
- (63) Loboda, M. J.; Grove, C. M.; Schneider, R. F. *J. Electrochem. Soc.* **1998**, *145*, 2861.
- (64) Rodríguez, J.; Veinot, J. G. C. *J. Mater. Chem.* **2011**, *21*, 1713.
- (65) Bang, J.; Jeong, U.; Ryu, D. Y.; Russell, T. P.; Hawker, C. *Adv. Mater.* **2009**, *21*, 4769.
- (66) Meldrum, A.; Hryciw, A.; MacDonald, A. N.; Blois, C.; Clement, T.; DeCorby, R.; Wang, J.; Li, Q. *J. Lumin.* **2006**, *121*, 199.
- (67) Meldrum, A.; Hryciw, A.; MacDonald, A. N.; Blois, C.; Marsh, K.; Wang, J.; Li, Q. *J. Vac. Sci. Technol. A* **2006**, *24*, 713.
- (68) Yerushalmi-Rozen, R.; Kerle, T.; Klein, J. *Science* **1999**, 285, 1254.
- (69) Merabia, S.; Avalos, J. B. *Phys. Rev. Lett.* **2008**, *101*.
- (70) Hessel, C. M.; Henderson, E. J.; Veinot, J. G. C. *J. Phys. Chem. C* **2007**, *111*, 6956.
- (71) V. A. Belyakov, V. A.; V. A. Burdov, V. A.; Lockwood, R.; Meldrum, A. *Adv. Opt. Tech.* **2008**, 2008, 1.
- (72) Li, Y.; White, T. J.; Lim, S. H. *J. Solid State Chem.* **2004**, *177*, 1372.
- (73) Delak, K. M.; Sahai, N. *Chem. Mater.* **2005**, *17*, 3221.

**Chapter 4:**

**Photoassisted Etching**

**of**

**Oxide-Embedded**

**Silicon Nanocrystals**

*A version of this chapter has been submitted for publication:*

*Rodriguez Núñez, J. R.; Kelly, J. A.; Henderson, E.; Veinot, J. G. C.; Chemistry of  
Materials*

#### 4.1. Introduction

Semiconductor nanoparticles have been intensively studied in the past two decades in an effort to understand their fundamental properties and to develop novel applications.<sup>1-4</sup> Synthesis of Group II-VI or III-V nanostructures can yield significant quantities of crystalline, highly monodisperse products.<sup>5,6</sup> Furthermore the direct band-gap character of these materials paved the way for the elucidation of unique size related optical characteristics observed in the nano-regime.<sup>1,7-9</sup> Although these structures can be used in optoelectronics, their toxicity is of great concern for drug delivery and *in-vivo* sensing.<sup>10-12</sup> The biocompatibility,<sup>13,14</sup> cost,<sup>15</sup> and availability<sup>15</sup> of Group IV semiconductor nanomaterials such as Si, Ge, SiGe, and SiC is a major driving force in the development of methods to prepare large quantities of nanoparticles with controllable physical and chemical characteristics.<sup>16-21</sup>

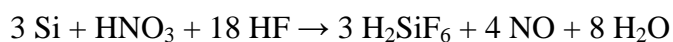
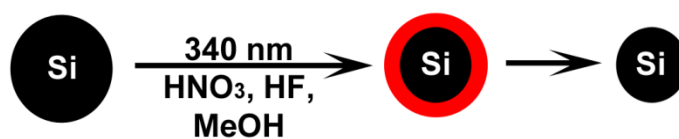
Many synthetic methods have been developed to produce silicon nanocrystals, ranging from aerosol pyrolysis, reduction of silicon halides, and thermal disproportionation of silicon rich oxides (SROs), among others.<sup>19,22-24</sup> SROs or suboxides can be obtained commercially (e.g., hydrogen silsesquioxane from Dow Corning) or by hydrolysis and condensation of silicon halides or alkoxydes.<sup>23-26</sup> Upon thermal treatment, suboxides disproportionate to form silicon nanocrystals in a silica matrix.<sup>23-26</sup> Our group has developed methods that yield gram quantities of oxide-embedded silicon nanocrystals (OE-Si-NCs) by thermolysis of SROs.<sup>25,26</sup> The matrix is routinely removed using HF<sub>(aq)</sub> yielding

free-standing silicon nanocrystals (FS-Si-NCs) which can then be further functionalized via hydrosilylation for a variety of applications.<sup>25,27</sup>

The biocompatibility of Si-NCs along with the high quantum yield (some reports are as high as 60%) make them ideal candidates for *in-vivo* sensing.<sup>14,28-31</sup> Furthermore their compatibility with current silicon technology puts Si-NCs on the forefront of quantum dots in the field of computing photonics.<sup>32</sup> These applications will benefit if the nanocrystal luminescence maxima can be controlled and the linewidth narrowed.<sup>33,34</sup> Ideally, NC size and size distribution will be the main determining factor of the optical response, however, in practice controlling the nanoparticle defect density can be just as critical.<sup>35-40</sup> In addition to defects, NC-NC interactions such as tunneling can also affect the optical response.<sup>41</sup>

General, luminescence from Si-NCs across the visible and near-IR regions has been demonstrated by increasing the processing temperature (producing larger crystals) or by HF etching (producing smaller crystals).<sup>25</sup> For example, our group reported that exposing OE-Si-NCs to a mixture of water, HF, and ethanol, the oxide matrix is dissolved away, further exposure to the etching mixture causes FS-Si-NCs to decrease in size as they are etched by the fluoride ions.<sup>25</sup> As quantum confinement theory predicts the luminescence of the FS-Si-NCs blue-shifts with decreasing particle size (increased HF exposure over time). This observation is not unique to our system: Swihart has reported similar observations for particles formed by laser assisted thermal decomposition of silanes to a

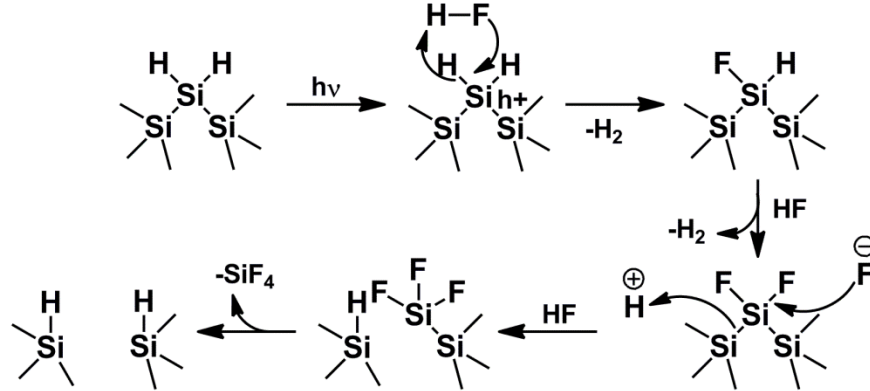
$\text{HNO}_{3(\text{aq})}/\text{HF}_{(\text{aq})}$  mixture.<sup>22</sup> Etching of silicon nanocrystals using nitric and hydrofluoric acid is widely used and understood; the nitric acid oxidizes the silicon surface, which is subsequently etched away via  $\text{HF}_{(\text{aq})}$ . Reipa, *et al.* reported light mediated oxidation of Si nanocrystals using UV radiation in the presence of nitric acid, the oxidized surface can then be etched with hydrofluoric acid (Scheme 1).<sup>42</sup>



**Scheme 4.1.** Etching mechanism based on oxidation of silicon surface.

An oxidizing agent (nitric acid in this case) is necessary for this process to occur. Once the oxide surface is formed it can be etched away via HF acid.

Literature published in the 1990s that describe anodic etching of silicon to form porous silicon (p-Si) highlights two possible silicon etching mechanisms: the first uses an oxidizing agent (Scheme 1) and follows the steps described above, the second is exciton mediated.<sup>43-45</sup> In the latter, a hole migrates to the silicon surface and is then attacked by HF, producing a Si-F bond on the surface (Scheme 2).<sup>45</sup> Fluorine withdraws electron density from the silicon atom making it more electrophilic and more susceptible to further fluoride attack.



**Scheme 4.2** Exciton mediated etching mechanism of silicon surfaces using hydrofluoric acid.

It is reasonable that these two mechanisms implicated in the formation of p-Si are also at play during Si-NC etching, however, to the best of our knowledge, no methods used to etch Si-NCs exploit the exciton mediated mechanism. Finding a method to etch silicon nanocrystals using light-generated excitons should provide a pathway to control the crystallite size and optical properties. As shown in Figure 4.1, it is expected that an exciton-mediated etching will provide size selection of the particles solely on the basis of the energy of the incident radiation on the sample. Consider the black nanocrystals (A) in Figure 4.1: if they are irradiated with red light (of energy equal to the red bandgap) the particles of size A will be etched to a minimum of size B (red particles of red bandgap). Once the particles reach a size corresponding to red bandgap, there will be insufficient energy in the incident light to induce a bandgap transition. If the red sized particles are then exposed to green light (of energy equal to the green bandgap) the process will continue and particles will achieve a minimum size C (green). Controlling the luminescence in this manner will affect the photoluminescence

(PL) bandwidth which is dependent on homogeneous and inhomogeneous broadening.<sup>46</sup> Size dispersity is a common and important source of inhomogeneous broadening.<sup>46,47</sup> In addition, exciton mediated etching should yield materials with luminescence breadth partially dependent on the linewidth of the excitation source, and thus will offer a method to control the PL bandwidth.

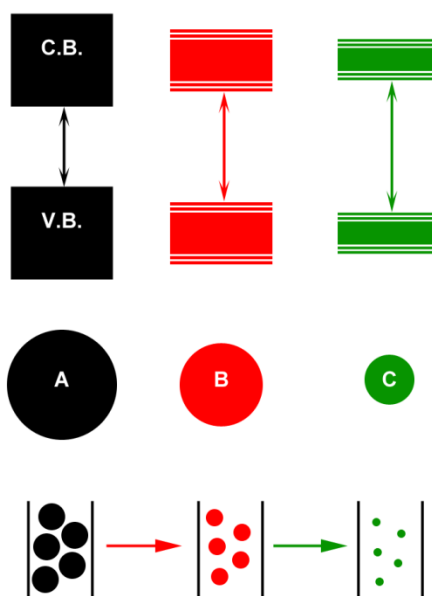


**Fig. 4.1** Schematic of the size control expected using exciton mediated etching of silicon nanocrystals.

In this chapter a novel method for controlling Si-NC luminescence using an exciton mediated HF etching process is reported. In order for photoetching to take place, the oxidative method has to be turned off. This is achieved by etching under strongly acidic conditions that prevent oxidation of the NCs by water. The effect of pH, oxidation ability of the conjugate base, and linewidth of the

irradiating source is presented. Lastly, the effect of photoetching in crystal size using Small-Angle X-ray scattering is discussed.

## **4.2. Experimental Details**

### **4.2.1. Material preparation**

#### **4.2.1.1. Composite preparation**

OE-Si-NCs were prepared by thermally processing hydrogen silsesquioxane at 1100 °C under 5% H<sub>2</sub> 95% Ar atmosphere. The resulting brown composite was manually ground using mortar and pestle. To ensure uniform grain distribution the ground composite is placed in a wrist-action-shaker with silica beads for at least 6 hours. A thorough characterization of the oxide embedded particles can be found elsewhere.<sup>25</sup>

#### **4.2.1.2. Etching of OE-Si-NCs using HCl<sub>(aq)</sub>, HNO<sub>3(aq)</sub>, and H<sub>2</sub>SO<sub>4(aq)</sub>**

In a typical experiment, approximately 0.10 g ± 0.02 g of composite was weighed in a polyethylene beaker. 75 µL of concentrated acid (HCl<sub>(aq)</sub> (Anachemia), HNO<sub>3(aq)</sub> (Caledon), or H<sub>2</sub>SO<sub>4(aq)</sub> (Fisher Scientific)) and 3 mL of 49% HF<sub>(aq)</sub> (J.T. Baker) are added to the beaker. The mixture was stirred using a 1 inch magnetic stir bar for 5 minutes before adding 1.5 mL of ethanol to aid with surface wetting upon matrix removal. The etching mixtures were exposed to monochromatic light of different wavelengths (conditions shown in Table 4.1) using a CM 110 Compact 1/8m monochromator from Spectral Products. The etching mixtures change colour from yellow to white during etching. The rate of the colour change is dependent on the irradiation wavelength, etching time, and strong acid present. Unless stated otherwise, etching was performed inside a

specially designed etching box which prevents ambient light from reaching the etching mixture and allows illumination from the light source only.

The light source wavelength was calibrated using a USB 2000+ spectrometer with a range from 350 nm to 1100 nm. The power of the light source was kept constant at approximately 70 mW.

**Table 4.1** Conditions of samples etched using different acids.

Sample	Light Conditions	Acid used
1	Dark	HCl <sub>(aq)</sub>
2	700 nm	HCl <sub>(aq)</sub>
3	600 nm	HCl <sub>(aq)</sub>
4	500 nm	HCl <sub>(aq)</sub>
5	Ambient*	HCl <sub>(aq)</sub>
6	Dark	HNO <sub>3(aq)</sub>
7	Dark	H <sub>2</sub> SO <sub>4(aq)</sub>
8	600 nm	H <sub>2</sub> SO <sub>4(aq)</sub>

\*Ambient etching was performed in a fumehood, outside of the dark etching box with all the laboratory fluorescent lights turned on.

#### 4.2.1.3. Laser etching of OE-Si-NCs

A mixture of  $0.10 \pm 0.02$  g of composite, 75  $\mu$ L HCl, 3 mL HF (J.T. Baker) and 1.5 mL of ethanol were stirred under laser irradiation. The 647 and 568 nm lines of a variable wavelength Ar<sup>+</sup> ion laser (Innova Coherent 60 C) were

used, starting with the lowest energy and switching to a higher energy every 4 hours during the course of the experiment.

#### **4.2.1.4. Functionalization of OE-Si-NCs**

Freestanding silicon nanocrystals etched under dark and ambient conditions, and using the 568 nm line of an Ar<sup>+</sup> ion laser were extracted into toluene (Caledon). The toluene extracts were transferred into centrifuge tubes and centrifuged at 3,000 rpm. The toluene was decanted, and the precipitated Si-NCs were redispersed in 10 mL freshly purified 1-dodecene and transferred to a Schlenk flask equipped with a stir bar under an argon atmosphere. The reaction mixture was degassed by three cycles of evacuation and purging with argon and placed in a silicon oil bath heated at 190°C for at least 15 h. The reaction mixture typically turned from turbid to transparent in the first 3 h of heating.

Following photochemical functionalization, the reaction mixtures were transferred into centrifuge tubes and spun at 3,000 rpm to precipitate any unreacted NCs. The supernatant from each reaction was filtered through a 250 nm PTFE syringe filter into a 50 mL centrifuge tube and precipitated by the addition of 37.5 mL of a 3:1 ethanol/methanol mixture and centrifugation (25,900 G for 20 min). Three additional purification by centrifugation cycles were performed using toluene and methanol as the solvent/antisolvent.

## **4.2.2. Material Characterization**

### **4.2.2.1. Photoluminescence (PL) Spectroscopy**

FS-Si-NCs were extracted into toluene and their PL was measured using the 325 nm line of a He/Cd laser as an excitation source. The spectrometer's spectral response was corrected using a standard blackbody radiator. Luminescence between 350 nm and 1100 nm was detected using a USB2000 spectrometer from Ocean Optics. Laser light was filtered out using a 430 nm coloured glass, long pass filter purchased from Thor Labs.

As described below, the PL of laser etched samples was collected *in situ* (i.e., in the HF etching mixture) to alleviate the issue of oxide defect luminescence. In the case of laser etching, the Ar<sup>+</sup> laser is blocked during PL measurements and the solution is briefly (<5 s) exposed to 325 nm He/Cd laser irradiation for data collection.

### **4.2.2.2. Small Angle X-ray scattering**

SAXS was performed on dilute dispersion of silicon nanocrystals in toluene sealed in a boron-rich silicate capillary (Charles Supper, 2 mm outer diameter, 80 mm length, 10 µm wall thickness). Measurements were performed using a Bruker NanoStar with a rotating copper anode X-ray generator ( $\lambda = 1.54$  Å) operating at 5.5 kW. The scattered photons were collected on a 2D multiwire gas-filled detector (Bruker HiStar) and the scattering angle was calibrated using a silver behenate (CH<sub>3</sub>(CH<sub>2</sub>)<sub>20</sub>COOAg) standard. Radial integrations of scattering

intensity were performed using Bruker GADDS software. Experimental data was corrected for background scattering. Data were fit to a spherical particle model<sup>48</sup> with a Gaussian size distribution using the Irena package for Igor Pro.<sup>49</sup>

### 4.3. Results and Discussion

Si-NCs are attractive materials for biological and optoelectronic applications due to their low toxicity and compatibility with current silicon-based technologies.<sup>30,32,37</sup> The development of a continuous-wave Silicon Raman laser in 2005 by Intel scientists underlines the importance of silicon as a photonic material.<sup>50</sup> Most of the suggested applications associated with Si nanostructures require control of the optical properties and a thorough understanding of what influences their luminescent behaviour.

Control of the optical properties of Si-NCs generally entails tailoring particle size.<sup>22,25</sup> Methods to control Si-NC particle size include but are not limited to modifying the silicon:oxygen ratio in suboxide precursors, altering processing temperature, using Si/SiO<sub>2</sub> superlattices, velocity selection of silicon aerosols.<sup>25,51-54</sup> These methods afford size distributions of 15-20% relative standard deviation, far from the 5% reported for colloidal CdSe nanocrystals.<sup>6,55</sup> As a result of the size distribution the full width at half maximum of Si-NCs is generally larger than 150 nm (> 0.42 eV).<sup>46</sup> Another method for controlling Si-NC particle size and subsequently the luminescence employs HF etching.<sup>22,25,42</sup> The Swihart group has reported using HNO<sub>3(aq)</sub>:HF<sub>(aq)</sub> mixtures to control particle size.<sup>22</sup> Under the reported conditions, the etching process relies upon chemical oxidation of the silicon surface with 10-40% HNO<sub>3(aq)</sub> followed by etching of the oxide using HF<sub>(aq)</sub>. This process leads a blueshift in the luminescence maximum of approximately 300 nm attributable to a decrease in particle size.

An alternate etching approach is based on the formation of an electron-hole pair (i.e., an exciton) in the nanocrystal. This is believed to be one of the dominating methods in the formation of porous silicon via anodized etching.<sup>45</sup> According to the proposed mechanism a hole migrates to the Si NC surface rendering the silicon atom electrophilic and susceptible to attack by fluoride ions. Once bonded to an F atom, the Si becomes more electrophilic due to the polarity of the Si-F bond. Repeated nucleophilic addition of F to Si occurs until  $\text{SiF}_{4(g)}$  is liberated.<sup>45</sup> This etching route is expected to proceed at a lower rate than the silicon oxidation pathway since it requires a hole to be localized at the surface for sufficient time to allow fluoride attack (the proposed rate determining step).

In the experiments discussed below, a mixture of  $\text{HCl}_{(aq)}$ ,  $\text{HF}_{(aq)}$  was used to etch the oxide matrix and decrease the nanocrystal size. It has been reported that the etching rate of silica is increased when acid is present due to the formation of a good leaving group.<sup>56</sup> In highly acidic media, hydrochloric acid protonates the silica matrix forming  $\equiv\text{Si-O-H}_2$  species, water can then be removed via an elimination reaction involving  $\text{HF}_2^-$  or  $\text{H}_2\text{F}_2$  yielding Si-F species.<sup>56</sup> IR spectra (Figure 4.2) of FS-Si-NCs extracted into toluene shows the effect of exposing OE-Si-NC composites to the etching mixture (HCl, and HF) for 1 min, 5 min, and 10 min. After only one minute a strong Si-H peak ( $2100\text{ cm}^{-1}$ ) is observed and only trace oxide is measured ( $1100\text{ cm}^{-1}$ ). Addition of ethanol after 5 minutes does not appear to increase the presence of oxide in the sample.

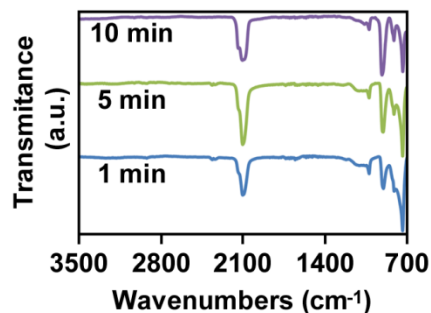


**Fig. 4.2** IR spectra of FS-Si-NCs etched using and  $\text{HF}_{(\text{aq})}$ ,  $\text{HCl}_{(\text{aq})}$ , EtOH mixture under ambient light (sample 5) for 1, 5, and 10 minutes. Ethanol is added after 5 minutes.

#### 4.3.1. Optical properties

In a typical experiment  $\text{HCl}_{(\text{aq})}$  and  $\text{HF}_{(\text{aq})}$  are used to remove the silica matrix. Upon formation of FS-Si-NCs (~ 5 minutes as shown in Figure 4.2), ethanol was added to aid silicon etching by enabling surface wetting. The etching mixture was exposed to light of a predetermined wavelength for the duration of the experiment, from here on this procedure will be referred to as “photoetching”. If samples are solely photoetched, the irradiation wavelength will determine the NC bandgap and thus the luminescence maximum, therefore, the PL of particles etched under no irradiation should exhibit no change in the PL maximum and the particles irradiated should display PL maximum close to the irradiation wavelength. An aliquot of the FS-Si-NCs was extracted into toluene every hour from the etching mixture and the PL monitored. Figure 4.3 shows the luminescence maximum of FS-Si-NCs is dependent on the radiation wavelength. PL of FS-Si-NCs suspended in toluene does not shift meaningfully when etched

in the dark (Figure 4.3.a). When OE-Si-NCs are exposed to the etching mixture under 700 nm light and 600 nm light (at a constant power), the PL of the FS-Si-NCs peaks at shift to  $\sim 700$  and  $\sim 600$  nm, respectively (Figure 4.3.b,c). When the NCs are etched using 500 nm light the PL maxima was more variable, never shifting below 600 nm, similar to samples etched under ambient light (Fig. 4.3.d,e)

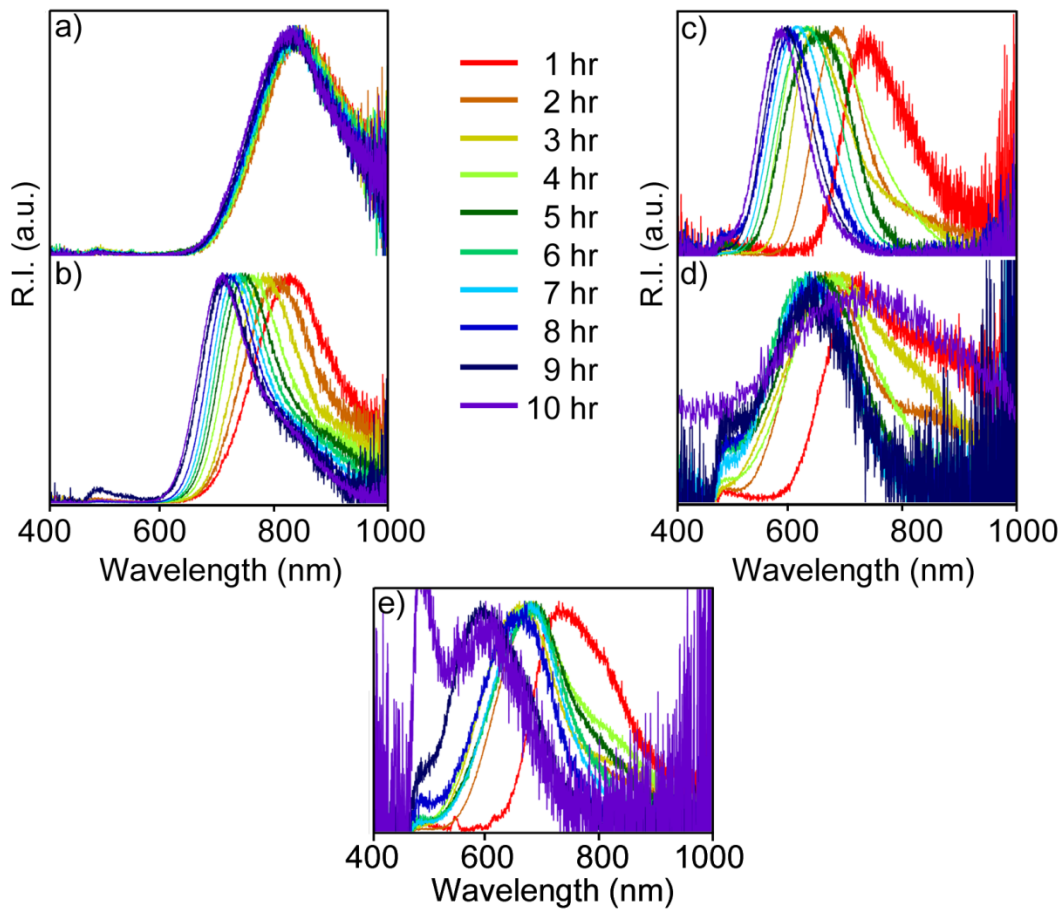


**Fig 4.3** PL spectra of toluene extracted FS-Si-NCs etched using and HF, HCl, ethanol mixture (see samples 1-5 experimental section) when exposed to no light (a), 700 nm (b), 600 nm (c), 500 nm (d), and ambient light (e)

To further evaluate the optical behaviour of photoetched Si-NCs a plot of PL maxima vs. etching time in hours is shown in Figure 4.4.a. While the dark (no light) and 700 nm photoetched optically active particles behave as expected (i.e., no PL shift and monotonic blue shift of PL maximum, respectively) Si-NCs exposed to 600 nm, 500 nm, and ambient light do not. The composite photoetched using 600 nm light blue-shifts from ~730 nm to ~630 nm during the first four hours. After four hours the PL unexpectedly redshifts to ~650 nm. During the remaining 5 hours a monotonic blue-shift is observed to a minimum PL energy of 584 nm after 10 hours. The unexpected red-shift may arise from the “turning on” of silicon nanocrystals with ill-defined surface chemistry, or to oxidation of the nanoparticles in the toluene solution prior to measuring luminescence. During the etching process, some particles will have surface defects as they transition from being in an oxide matrix to being hydride terminated.<sup>57</sup> Irrespective of this red-shift, the continued blue shift of the PL maximum after 5 hours of etching accompanied by the slow shift in PL wavelength as it approaches 600 nm suggests the etch primarily proceeds by the exciton mediated mechanism.

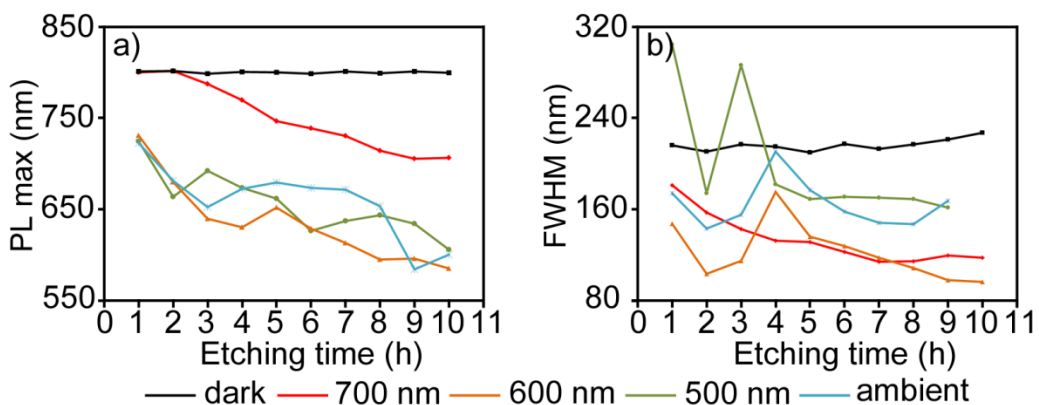


**Fig 4.4** (a) PL maximum of Si-NCs in toluene as a function of etching time etched under different irradiation conditions. The dark, 700 nm and 600 nm photoetched samples behave as expected, while the 500 nm and ambient light appear more erratic. (b) Full-width at half maximum as a function of etching time. The high energy photoetched particles display a noticeable spike of the FWHM.

The higher energy, 500 nm and ambient etches, behave differently than their lower energy counterparts. Two effects may be responsible for the observed red-shift, namely breaking of bonds in the nanocrystal and Si=O defects. Bond breaking upon exposing bulk, hydride terminated silicon to white light irradiation is known as the Staebler-Wronski effect.<sup>58,59</sup> Photoconductivity is observed to decrease significantly after prolonged illumination of hydride passivated silicon surfaces with intense light.<sup>58</sup> This observation has been attributed to a reversible increase of gap states where the electron-hole pair can recombine.<sup>60</sup> Gap states

are created upon the formation of an exciton near a weak Si-Si bond, the exciton can recombine non-radiatively releasing enough energy to break weak Si-Si bonds. This process creates dangling bonds. Si-NCs photoetched under 500 nm and ambient light, may experience bond breaking of Si-Si bonds located at the surface (high energy, weaker bonds). The broken bonds may yield surface radicals which could form Si-O bonds which will then be etched by HF affecting the luminescence of the resulting particles. This effect is expected to occur only during photoetching and not after toluene extraction (i.e. when no more  $\text{HF}_{(\text{aq})}$  present).

Wolkin et al. have studied the effect of Si=O bonds in the PL of Si-NCs formed within porous silicon.<sup>36</sup> Their study proposes that Si=O defects could be responsible for orange luminescence in small crystallites. In this model, at sizes above 3 nm, the luminescence is purely an interband transition. Once the NC size decreases below 3 nm, the energy of the Si=O localizes above the interband transition, due to the continuous shrinking of the bands as size decreases. Si=O bonds can be formed following extraction into toluene in order to passivate reactive defects in the nanocrystal, possibly formed by the extended irradiation. The PL maximum of the 500 nm light etch shows two regions where the PL red-shifts, namely after two hours and after six hours. These shifts may arise because of a “turning on” of nanocrystals that have ill defined surface during etching or to a high oxidation propensity for particles of a given size.

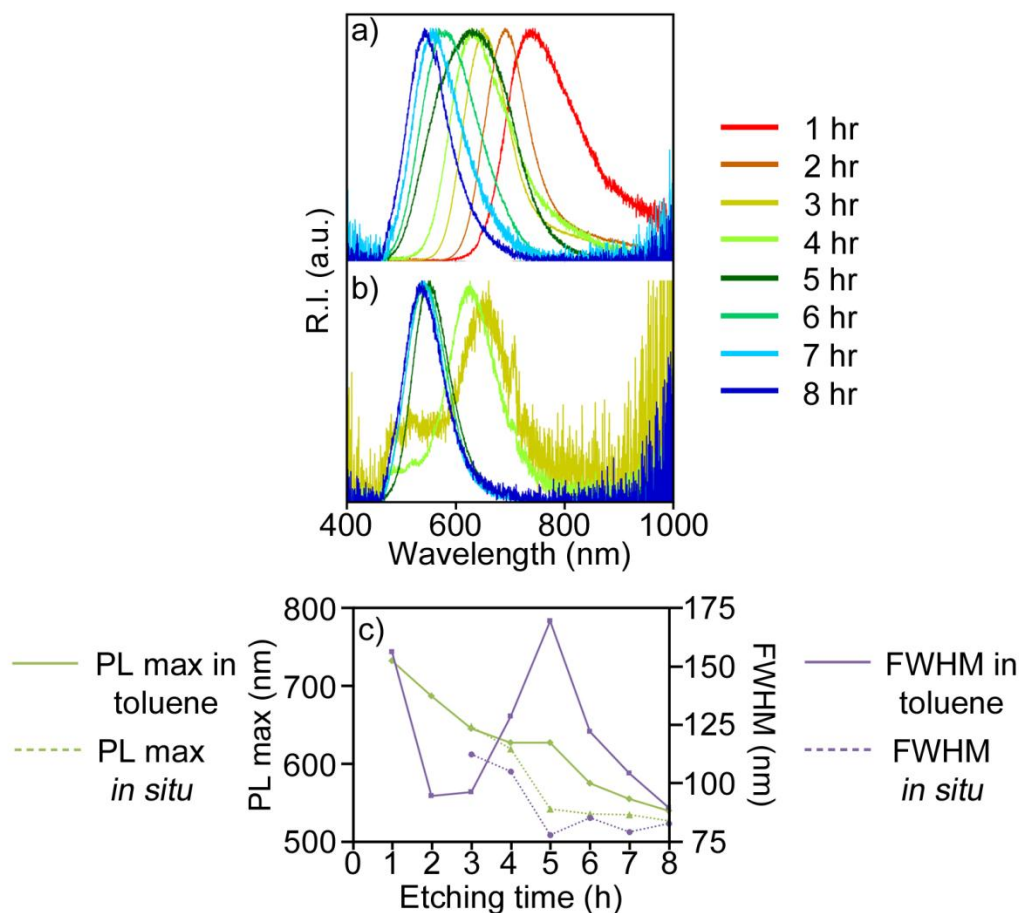
Monitoring the PL maximum in the ambient etch (Figure 4.4.a) for the period between 4 hours and 8 hours it is clear that no shift occurs. In this case, the luminescence is probably controlled by Si=O defects that give rise to the orange luminescence and are not dependent on particle size. PL after 8 hours is very low in intensity as is evidenced by the spectral noise in Fig 4.3.e. After 8 hours of etching probably only very small well passivated particles remain in the toluene solution controlling the luminescence.

Figure 4.4.b is a plot of the FWHM as a function of etching time and can yield information regarding the monodispersity of luminescent FS-Si-NCs, depending on the degree of inhomogeneous broadening of the etched samples. At first glance, it is evident the FWHM of the dark, 700 nm, and 600 nm photoetched samples is proportional to the excitation wavelength, furthermore the 500 nm, and ambient etch have essentially the same FWHM after 9 hours (FWHM at 9 hours could not be determined due to low signal-to-noise ratio). Looking at Figure 4.1, it is clear that if the starting particle distribution encompasses black, red, and green particles etching with red light will only affect the black particles producing a broader size distribution than if the etch was performed using green light. Upon closer inspection, it is observed that dark etch shows no noticeable change in FWHM even after 10 hours of exposure to  $\text{HCl}_{(\text{aq})}$  and  $\text{HF}_{(\text{aq})}$ . This observation is consistent with a photoetching mechanism where Si-NCs are not etched in the dark (ie. size distribution is unchanged). Etching using 700 nm irradiation shows an almost monotonic decrease in FWHM with time, consistent with the proposed photoetching mechanism.

In contrast, the FWHM in ambient, 600, and 500 nm light (Fig. 4.4.b) is less straightforward to understand. Initially, the FWHM of the FS-Si-NCs increases dramatically during the 2 hour to 5 hour range. This increase can be attributed to particles exhibiting luminescence of various origins such as quantum confinement, oxide states, and midgap states. Etching particles with 500 nm and ambient light may be responsible for bond breaking creating reactive surface species that upon reaction will yield particles with unpredictable luminescent properties responsible for the broad FWHM.

For the photoetching mechanism, the FWHM can be controlled by choosing a narrow band lightsource. A variable wavelength  $\text{Ar}^+$  laser was used to narrow the PL profile. Approximately 100 mg of OE-Si-NCs were etched using  $\text{HCl}_{(\text{aq})}$  and  $\text{HF}_{(\text{aq})}$  in a plastic vial while radiating the mixture with the 647 nm line (40 mW) for 4 hours. After 4 hours the radiation wavelength was switched to the 568 nm line for another 4 hours. Approximately 250  $\mu\text{L}$  of the etching mixture was extracted into toluene and the PL was measured at hourly intervals. The PL was collected in two different experiments, one extracting the etching mixture into toluene, and the other by collecting the PL *in situ* (free from oxidation effects in the etching mixture). The PL of the nanocrystals extracted into toluene etched using laser light is shown in Figure 4.5.a and displays the expected monotonic blue-shift as the etch progresses. Interestingly, the broadest PL occurs after five hours of etching i.e., one hour after switching the irradiating wavelength. Figure 4.5.b shows the *in situ* PL of the etched Si-NCs (PL for the first two hours is not measurable, low signal-to-noise ratio). The green traces in Figure 4.5.c show the

shift in PL max. as a function of etching time in toluene. From this plot it can be noted that after 4 hours the PL maximum is approximately the same for the particles in the HF etching mixture and toluene. This trend however is markedly different after 5 hours of etching (i.e., one hour after switching the radiating wavelength). The PL max. in toluene does not change appreciably between 4 and 5 hours of etching (~ 627 nm), however the PL max. in HF shifts by over 70 nm (from 619 nm to 542 nm). In addition, after 5 hours the *in situ* PL changes minimally (15 nm over 3 hours) while the PL of the toluene extracted particles shifts from 627 nm to 540 nm (87 nm) over the same period of time. It is possible that switching the radiating wavelength decreases the particle size to a dimension that is particularly unstable and prone to oxidation when exposed to toluene. With time, particles are etched to a size that is more stable and the photoluminescence in toluene and HF start to converge.



**Fig. 4.5** a) PL of etched silicon nanocrystals extracted into toluene displaying a blueshift with increasing etching time, nanocrystals were irradiated with the 647 nm line for the first four hours and then with the 568 nm line for the last four hours. b) PL of etched silicon nanocrystals *in situ* (in the etching mixture, without extracting into toluene) displaying a blueshift with increasing etching time. c) A plot of PL max (green traces) and FWHM (purple traces) as a function of etching time for nanocrystals extracted into toluene (solid line) and nanocrystals in the etching mixture (dashed).

In contrast to observations with Xe lamp induced etching, Figure 4.5.c shows the PL profile of liberated Si-NCs narrows when using laser irradiation. The narrowest FWHM obtained using the Xe light source after 8 hours of etching was 108 nm (for 600 nm irradiation), compared with 90 nm after etching with the 647 nm and the 568 nm laser lines for 8 hours (extracted into toluene). The narrowest FWHM (77 nm) was collected *in situ* after 5 hours of etching (4 hours with the 647 nm line and one hour with the 568 nm line). Keeping in mind the FWHM of single Si-NCs is approximately 40 nm (only due to homogeneous broadening)<sup>33</sup>, a FWHM of 77 nm for an ensemble of NCs is remarkable. Although there is narrowing of the PL when etching under laser light, both sources produce PL with comparable bandwidth. After five hours the PL in toluene becomes the broadest while the *in situ* measurement after the same time afforded the narrowest PL. This observation gives credence to the hypothesis that oxide free nanocrystals in HF are oxidized quickly upon exposure to toluene. Following extraction, the PL is controlled by quantum confined luminescence and by defect luminescence. Luminescence from these two sources increases the breadth of the PL band.

#### **4.3.2. Etching mechanism**

There are two generally accepted mechanisms involved in HF etching of silicon nanocrystals: a fast oxidative pathway and a slow exciton mediated route. The first, generally involves a strong oxidizing agent, such as nitric acid which oxidizes the silicon surface. The oxide can then be etched by HF. The exciton

mediated route requires the formation of a hole at a surface silicon atom. The electrophilic Silicon center can then be attacked by electronegative fluoride. The exciton mediated mechanism uses a mixture of 75  $\mu\text{L}$  of  $\text{HCl}_{(\text{aq})}$  and 3 mL of  $\text{HF}_{(\text{aq})}$  followed by addition of ethanol to proceed after matrix removal (5 mins, see Fig. 4.2). Ethanol and HF are ubiquitous in many etching recipes, they serve to wet the nanocrystal surface facilitating fluoride attack which forms gaseous  $\text{SiF}_{4(\text{g})}$ .<sup>61</sup> We propose that in order to activate the exciton mediated mechanism (i.e., turn off the fast oxidative pathway) all oxidizing species, such as water, must be removed or rendered inactive. Based on the previous discussion, it appears that HCl, provides a convenient way to “trap” the water present in 49%  $\text{HF}_{(\text{aq})}$ , thus preventing oxidization of the surface by water. In addition, the ideal acid must also possess an anion incapable of oxidizing the Si surface. In this regard, concentrated hydrochloric acid was chosen. The resulting optical properties of Si-NCs etched using  $\text{HCl}_{(\text{aq})}$  were described in detail above, however, the effect of using acids with different oxidizing powers may give insight on the photoetching mechanism. The effect of the oxidizing power of the conjugate base was studied using four etching mixtures:



The first method was described in Section 4.3.1. in detail, discussion of the remaining three mixtures will follow.

$\text{HNO}_3$  is a strong oxidizing agent; for this reason, a mixture of nitric and hydrofluoric acid is expected to etch Si-NCs in the dark. Exposure of Si-NCs to mixture 2 ( $\text{HNO}_3$ , HF, EtOH) in the dark, causes vigorous bubbling and production of a brown gas. This observation suggests reduction of  $\text{HNO}_{3(\text{aq})}$  into  $\text{NO}_{2(\text{g})}$  after byproduct exposure to ambient oxygen.<sup>62</sup> After one hour, the etching mixture is colourless and clear, in contrast with the yellow solutions obtained in previous experiments. As expected, no Si-NC PL is observable after one hour of etching.

The sulfate anion has an oxidizing power in between that of  $\text{NO}_3^-$  and  $\text{Cl}^-$ . As the sulfate anions oxidize the Si surface to a lesser extent than  $\text{NO}_3^-$ , it is expected that etching using mixture 3 ( $\text{H}_2\text{SO}_4$ , HF, EtOH) in the dark will cause a slight blueshift of the PL over time. Two etching experiments were performed using sulfuric acid, one in the dark and one at 600 nm. PL spectra were collected after extracting into toluene and the PL max and FWHM are plotted as a function of time (Fig. 4.6). The PL max of the NCs etched in the dark display a large blueshift of approximately 60 nm. This shift is large in comparison to the 2 nm blueshift observed when etching with the hydrochloric/hydrofluoric acid mixture. This increased shift was attributed to the oxidizing ability of the conjugate bases present upon dissociation of sulfuric acid and hydrogen sulfate. The 600 nm etch follows a similar trend to the particles etched with  $\text{HCl}_{(\text{aq})}$  under 600 nm

irradiation. This suggests that the exciton mediated pathway dominates using  $\text{H}_2\text{SO}_4$  and 600 nm irradiation. The FWHM of the dark etched particles does not change appreciably over time suggesting a similar etching rate for the large particles and small particles, expected for an oxidative etch. The FWHM of the 600 nm etched NCs decreases as expected for photoetched particles.

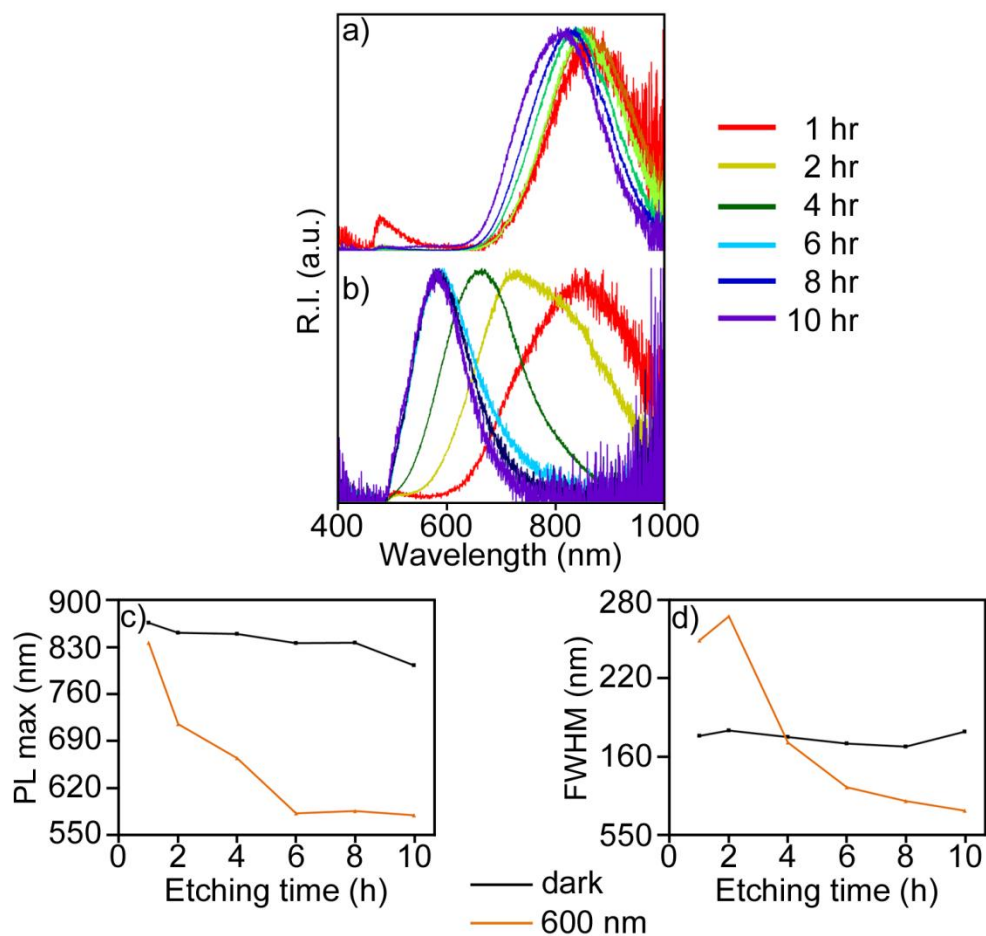


**Fig. 4.6** PL spectra of Si-NCs etched in the dark (a), and with 600 nm irradiation (b) using  $\text{H}_2\text{SO}_{4(\text{aq})}$ . Plot of PL max (c) and FWHM (d) as a function of time showing an intermediate behaviour between etching with  $\text{HNO}_{3(\text{aq})}$  and  $\text{HCl}_{(\text{aq})}$ .

To further investigate the role of the acidity, an etching experiment was performed in the dark using a 1:1:1 v/v/v mixture of  $\text{HF}_{(\text{aq})}:\text{EtOH}_{(\text{l})}:\text{H}_2\text{O}_{(\text{l})}$  using water at pH of 0.5, 1.0, 3.5, acidified using  $\text{HCl}_{(\text{aq})}$  and “neutral” (pH 6.6) deionized water. The effect of acidity on the PL of freestanding silicon nanocrystals is shown in Figure 4.7. It is clear that even under dark conditions and low pH (~0.5, similar to the calculated pH when photoetching using  $\text{HCl}_{(\text{aq})}$ ) the PL blue-shifts with etching time, thus it can be concluded that the photoetching mechanism is turned off even in highly acidic conditions. The origin of this behaviour may be attributed to the ability of water to oxidize silicon. At first glance, this hypothesis would suggest that addition of aqueous HCl and HF should oxidize the silicon surface. However, it is worth noting that the presence of solvated ions (from the strong acids used) will affect the ionic strength and activity coefficients of each ion in solution. This, in turn, may affect the ability of the nitrate, and sulfate anions to oxidize the silicon surface.

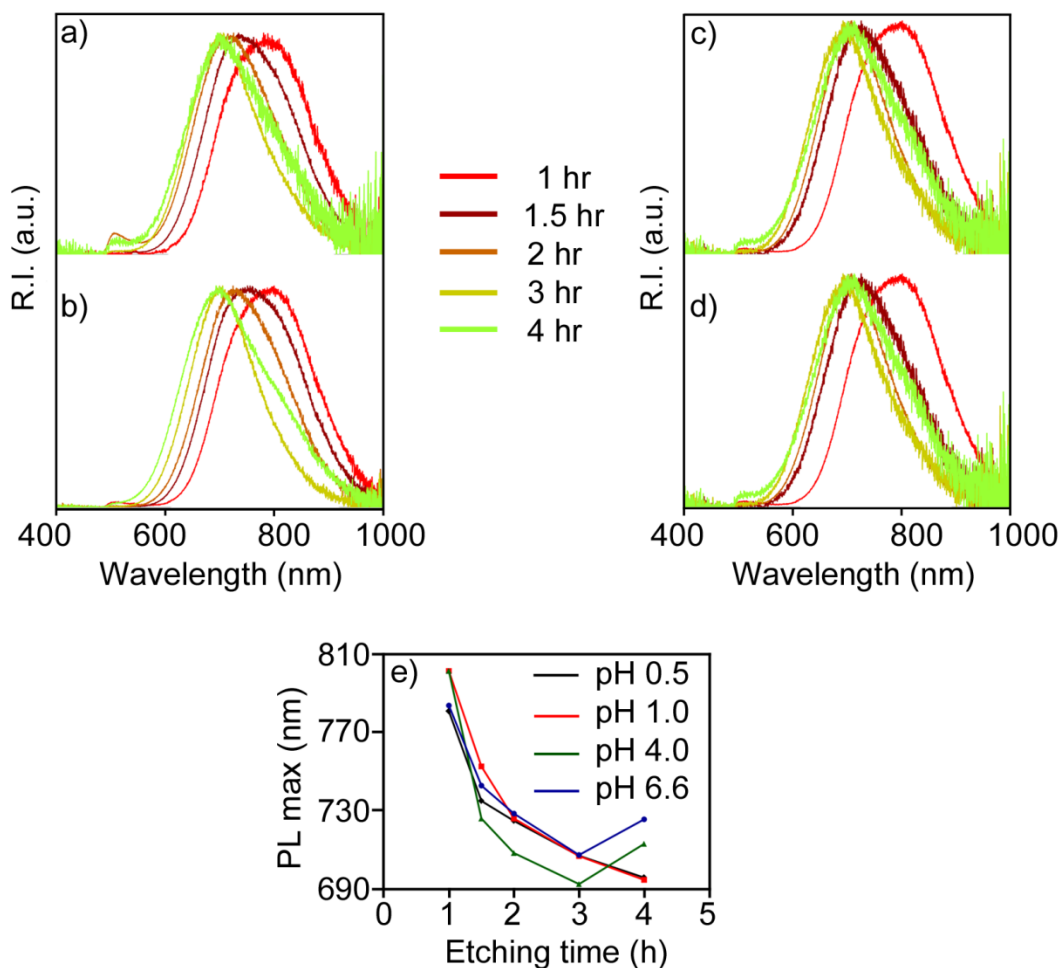


**Fig. 4.7** PL spectra of composites etched with water at pH 0.5 (a), 1.0 (b), 3.5 (c), and 6.6 (d). Plot of photoluminescence maxima as a function of time for different pH etching solutions (e).

These experiments confirm our hypothesis that two competing mechanisms, an oxidative pathway and an exciton mediated route are operating in the etching of Si-NCs. The oxidative pathway is the dominant process as long as an oxidizing agent is present in the etching mixture. The exciton-mediated, photoetching process is slower and will dominate only in the absence of oxidizing

agents and/or surface oxides. In the presence of a strong oxidizing agent such as nitric acid, the particles are etched away in the dark quickly. When sulfuric acid (a weaker oxidizing agent than  $\text{HNO}_{3(\text{aq})}$ ) is used the particles appear to be etched primarily by the exciton mediated mechanism, however the dark etch suggest some oxidative etching takes place. Particles exposed to water, ethanol and hydrofluoric acid can also be etched in the dark even at low pH due to water's oxidative nature.

### 4.3.3. Size distribution

Silicon composites etched using the exciton mediated mechanism display PL related to the irradiating wavelength for any  $\lambda \geq 568$  nm (See Figure 4.4 and 4.5). According to quantum confinement, the observed PL is related to the particle size, i.e. the larger the particle the lower the energy of luminescence and viceversa. The size of a nanoparticle can be calculated from the PL by the following approximation derived from the reduced mass model:<sup>63</sup>

$$e_g(R) = \sqrt{e_g^2 + \left(\frac{4.8 \text{ eV}^2 \text{ nm}^2}{R^2}\right)} \quad (6)$$

where  $e_g$  is the bandgap of bulk silicon in eV (1.1 eV),  $e_g(R)$  is the bandgap of the nanocrystal (can be calculated from the emission wavelength), and R the radius of the nanocrystal.

In order to assess the size distribution of the nanocrystals three samples were photoetched for 6 hours using the 568 nm line of an  $\text{Ar}^+$  laser, ambient light

and in the dark. Immediately after etching, the particles were functionalized via thermal hydrosilylation with dodecene. PL spectra were collected immediately before and after functionalization (Figure 4.8).

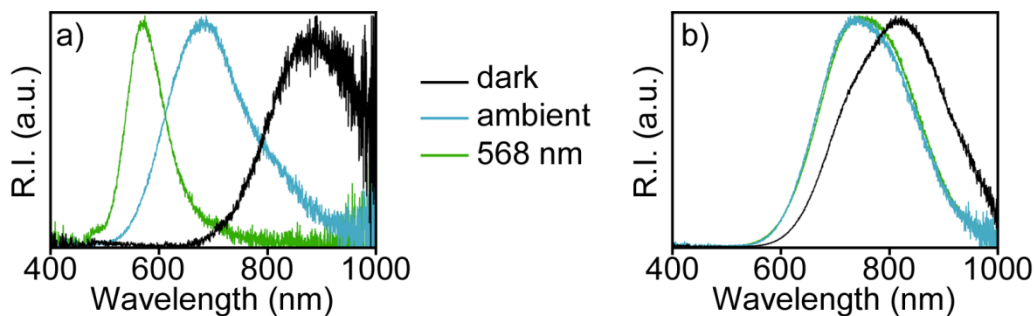


**Fig. 4.8** PL spectra of photoetched Si-NCs in the dark, ambient, and using 568 nm laser irradiation before (a) and after (b) functionalization.

**Table 4.2** PL max and FWHM of photoetched samples before and after functionalization

Conditions	PL max (nm)		FWHM (nm)	
	before functionalization	after functionalization	before functionalization	after functionalization
<b>Dark</b>	892	812	195	231
<b>ambient*</b>	687	737	179	204
<b>568 nm**</b>	574	759	83	205

\* The ambient PL may be due to defect luminescence.

\*\* PL was collected *in situ* in HF etching mixture.

The PL max and FWHM show stark contrast before and after functionalization. The highest energy PL is obtained for the 568 nm laser

photoetched sample, followed by the ambient and dark etched samples before functionalization. After functionalization the ambient and laser etched particles exhibit similar PL maxima, and the dark etched sample appears at lower energy. The FWHM can be a reflection of particle size distribution and it also changes after functionalization. In hydride terminated particles the lowest FWHM is that of the laser etched sample. The dark and ambient etched NCs have almost double FWHM prior to hydrosilylation. After dodecene functionalization, the ambient and laser etched samples show similar FWHM, and particles etched in the dark have the highest FWHM. Using (6), the radii of the particles etched under different conditions before (b.f.) and after functionalization (a.f.) can be approximated.

**Table 4.3** Calculated diameter from the PL spectra before functionalization (b.f) and after functionalization (a.f.) using the reduced mass approximation. Diameter and size distribution obtained from SAXS of dodecene functionalized particles

Conditions	D (nm)		SAXS	
	b. f.	a. f.	D (nm)	$\sigma$ (D) (nm)
<b>Dark</b>	5.15	4.13	5.0	1.2
<b>ambient*</b>	3.06	3.44	3.8	1.5
<b>568 nm**</b>	2.36	3.63	4.0	1.3

\* The ambient PL probably has a large component of defect luminescence expected for very small particles

\*\* PL was collected *in situ* in HF etching mixture (i.e. no oxide related PL).

The data summarized in table 4.2 and 4.3 shows a significant difference in PL max, FWHM, and particle size. Qualitatively, the size distribution of particles expected from Figure 4.8.a (before functionalization) is markedly different from that expected from Figure 4.8.b (after functionalization).

It is clear that a qualitative use of the PL to assess size distribution will limit the discussion to optically active particles resulting in conclusions that do not apply to the Si-NC population. For this reason, another technique must be used to elucidate the size properties of all the particles in the sample. Small angle X-ray scattering can give information about particle-size -distribution. Dodecene functionalized particles suspended in toluene were used for SAXS analysis and the average particle diameter and size distributions ( $\sigma$ ) are shown in Table 4.3.

These data indicate the size properties of the dark and laser etched samples are not as different as the hydride terminated PL suggests. Furthermore, the approximate size and size distributions obtained from SAXS are more in agreement with the qualitative conclusions drawn from PL of dodecene terminated particles.

The inconsistency between SAXS and PL allowed for a more thorough understanding of the photoetching mechanism. It is hypothesized that this inconsistency arises from defective nanoparticles (arising during thermal processing or etching). Defects can turn the PL off due to fast exciton quenching in the defect site. For the exciton mediated mechanism to take place the hole has to be localized on the surface until a fluoride anion can attack the silicon atom. This will only occur in optically active, defect-free particles. Since the size of the NCs (both optically active and dark) is not as different as the PL suggests, it is possible that after one hour annealing and silica matrix removal a large fraction of nanoparticles contain defects that turn off the PL thereby preventing exciton mediated etching from occurring. These defects can have deleterious effects in the quantum yield of the particles and might limit the usability of Si-NCs in photonic applications.

In an attempt to decrease the size distribution and to remove defects arising from matrix removal, a two-step etch was performed. First, the particles are exposed to a 1:1:1 v/v/v water, HF<sub>(aq)</sub>, and EtOH mixture for 30 minutes. This step removes the matrix and may passivate the surface of FS-Si-NCs. Following this step, 20 mL of HF<sub>(aq)</sub> and 3.5 mL of HCl<sub>(aq)</sub> are added to the etching mixture

to trap the water, decrease the pH, and maintain a relatively high HF:water ratio. The mixture is then exposed to a 660 nm diode laser. Two other control etches were performed using a 1) 1:1:1 v/v/v water, HF<sub>(aq)</sub>, and EtOH mixture for 2 hours (“water” etch) and a 2) photoetch using the standard HCl<sub>(aq)</sub> conditions under 660 nm irradiation (“acid” etch). The samples were then functionalized with dodecene, and the PL (Fig. 4.8) and SAXS collected.

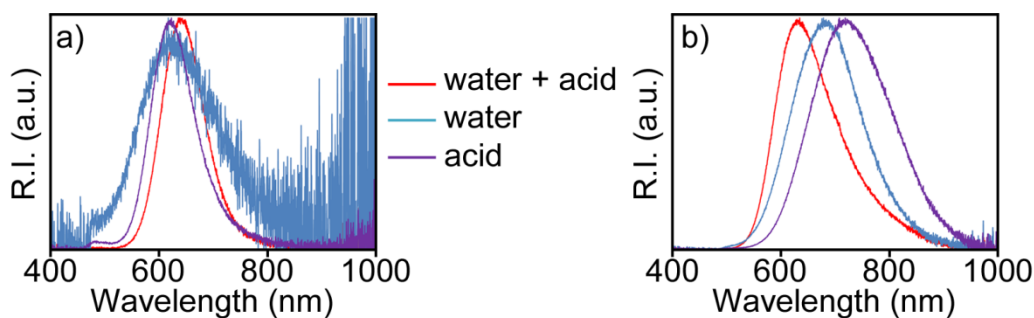


**Figure 4.9** PL before (a) and after (b) functionalization for samples etching using a two-step etch, a “water” etch, and an “acid” etch.

**Table 4.4** Calculated diameter and standard deviation of two-step, water, and acid only etched samples using the reduced mass approximation and SAXS.

Conditions	D (nm)		SAXS	
	b. f.	a. f.	D (nm)	$\sigma$ (D) (nm)
<b>two-step</b>	2.74	2.72	2.6	0.7
<b>water*</b>	2.61	3.01	1.6	0.8
<b>acid</b>	2.64	3.30	3.0	1.9

A shift in the calculated radius before and after functionalization for the “water” and “acid” etched samples is observed. Interestingly, only a negligible size change is noted for the two-step etched particles. Furthermore, the largest size increase occurs in the acid only etched sample, in agreement with our hypothesis that there exists a large population of dark particles in “acid” only etched samples after matrix removal. A broadening in the size distribution upon functionalization is observable for all samples. Diameter and size distribution extracted from SAXS show particle-size increases from “water” to “two-step” to “acid” etched nanocrystals. This is consistent with a higher etching rate occurring in the presence of an oxidizing agent (i.e. water). The size distribution of the two step etched samples is  $\sim 27\%$  according to SAXS. At first glance, this number appears very large, especially in light of the 4% size distribution obtained from CdSe NCs.<sup>55</sup> However, this variation is equivalent to only one or two unit cell layers in a spherical nanocrystal. In addition, the PL FWHM of the “two-step” etched particles is calculated to be 274 meV before functionalization and 385 meV after functionalization. Homogeneously broadened, single-particle Si-NC emission, exhibit a breadth of  $\sim 150$  meV at room temperature.<sup>33</sup> In this context, inhomogeneous broadening of Si-NCs of “two-step etched nanocrystals” before functionalization contributes less to the linewidth than homogeneous broadening.

#### 4.4. Conclusions

In this chapter a method to etch OE-Si-NCs using the exciton mediated mechanism is shown. This method requires the presence of two acids: a strong acid to “trap” water in the form of non nucleophilic  $\text{H}_3\text{O}^+$  and hydrofluoric acid to etch the silica matrix and the nanocrystals. Upon the formation of photogenerated excitons in the nanocrystal, a hole migrates to the particle surface making the silicon atom electrophilic and prone to fluoride attack. Following the formation of a Si-F bond, the electron density in the silicon atom decreases, polarizing the bond further and making silicon more electrophilic. Fluoride attack is repeated until gaseous  $\text{SiF}_{4(\text{g})}$  species are formed and removed from the etching mixture. The effect of the conjugate base during photoetching was studied using nitric, and sulfuric acid. It was demonstrated that the oxidizing ability of the conjugate base plays a key role and can “turn off” the exciton mediated mechanism in favour of the oxidation mechanism in the presence of nitric acid. Dark etching of silicon nanocrystals in the presence of water shows that even in high pH mixtures, water can inhibit photoetching by oxidizing silicon nanocrystals.

The linewidth of the excitation source is expected to control the FWHM of FS-Si-NCs. A narrow excitation source is expected to yield NCs with narrow optical properties. Etching using a Xe lamp and a laser source shows laser irradiation produces NCs with narrower PL, however the difference is not substantial. Furthermore particles in the HF mixture display narrower PL than

particles extracted into toluene suggesting oxidation creates an alternate pathway for luminescence that affects the PL bandwidth.

Generally, PL can be correlated to particle size due to quantum confinement effects. However, it appears that photoetching produces luminescence spectra that do not relate to particle size as measured by SAXS. These differences may be accounted for in terms of midgap states for samples etched under high energy light. However, this does not explain the differences in size and PL observed for particles etched with light of lower energy (i.e. >568 nm). These observations were attributed to a large population of dark NCs formed during thermal processing or matrix removal. Dark NCs will quench any excitons formed before HF attack takes place. In addition, these dark NCs will not appear in the PL spectra thus providing incorrect size distribution of the population. A two-step etching method was utilized to alleviate this issue. The first oxidative etching removes any defects present during matrix removal and leaves a well passivated surface. Afterwards, a high concentration of HCl and HF are added to turn off the oxidative mechanism and turn on the exciton mediated process. This method provides better agreement of size distribution between SAXS and PL spectra.

#### 4.5. References

- (1) Alivisatos, A. P. *Science* **1996**, *271*, 933.
- (2) Gao, X.; Cui, Y.; Levenson, R. M.; Chung, L. W. K.; Nie, S. *Nat. Biotechnol.* **2004**, *22*, 969.
- (3) Loss, D.; Divincenzo, D. P. *Phys. Rev. A: At., Mol., Opt., Phys.* **1998**, *57*, 120.
- (4) Michalet, X.; Pinaud, F. F.; Bentolila, L. A.; Tsay, J. M.; Doose, S.; Li, J. J.; Sundaresan, G.; Wu, A. M.; Gambhir, S. S.; Weiss, S. *Science* **2005**, *307*, 538.
- (5) Murray, C. B.; Norris, D. J.; Bawendi, M. G. *J. Am. Chem. Soc.* **1993**, *115*, 8706.
- (6) Peng, X.; Wickham, J.; Alivisatos, A. P. *J. Am. Chem. Soc.* **1998**, *120*, 5343.
- (7) Bawendi, M. G.; Steigerwald, M. L.; Brus, L. E. *Annu. Rev. Phys. Chem.* **1990**, *41*, 477.
- (8) Brus, L. *Applied Physics A Solids and Surfaces* **1991**, *53*, 465.
- (9) Nirmal, M.; Brus, L. E. 1997; Vol. 452, p 17.
- (10) Hardman, R. *Environ. Health Perspect.* **2006**, *114*, 165.
- (11) Deaves, M. *Manuf. Eng.* **2004**, *83*, 12.
- (12) Sinha, P.; Kriegner, C. J.; Schew, W. A.; Kaczmar, S. W.; Traister, M.; Wilson, D. J. *Energy Policy* **2008**, *36*, 381.
- (13) Ruizendaal, L.; Bhattacharjee, S.; Pournazari, K.; Rosso-Vasic, M.; De Haan, L. H. J.; Alink, G. M.; Marcelis, A. T. M.; Zuilhof, H. *Nanotoxicology* **2009**, *3*, 339.
- (14) Alsharif, N. H.; Berger, C. E. M.; Varanasi, S. S.; Chao, Y.; Horrocks, B. R.; Datta, H. K. *Small* **2009**, *5*, 221.
- (15) Huff, H. R. *Into the nano era*; Springer: Electronic reproduction, 2009.
- (16) Kelly, J. A.; Henderson, E. J.; Veinot, J. G. C. *Chem. Commun.* **2010**, *46*, 8704.
- (17) Henderson, E. J.; Hessel, C. M.; Veinot, J. G. C. *J. Am. Chem. Soc.* **2008**, *130*, 3624.
- (18) Henderson, E. J.; Veinot, J. G. C. *J. Am. Chem. Soc.* **2009**, *131*, 809.
- (19) Bley, R. A.; Kauzlarich, S. M. *J. Am. Chem. Soc.* **1996**, *118*, 12461.
- (20) Zhang, X.; Neiner, D.; Wang, S.; Louie, A. Y.; Kauzlarich, S. M. *Nanotechnology* **2007**, *18*.
- (21) Lee, D. C.; Pietryga, J. M.; Robel, I.; Werder, D. J.; Schaller, R. D.; Klimov, V. I. *J. Am. Chem. Soc.* **2009**, *131*, 3436.
- (22) Li, X.; He, Y.; Talukdar, S. S.; Swihart, M. T. *Langmuir* **2003**, *19*, 8490.
- (23) Das, G.; Ferraioli, L.; Bettotti, P.; De Angelis, F.; Mariotto, G.; Pavesi, L.; Di Fabrizio, E.; Soraru, G. D. *Thin Solid Films* **2008**, *516*, 6804.

- (24) Sorarù, G. D.; Modena, S.; Bettotti, P.; Das, G.; Mariotto, G.; Pavesi, L. *Appl. Phys. Lett.* **2003**, *83*, 749.
- (25) Hessel, C. M.; Henderson, E. J.; Veinot, J. G. C. *Chem. Mater.* **2006**, *18*, 6139.
- (26) Henderson, E. J.; Kelly, J. A.; Veinot, J. G. C. *Chem. Mater.* **2009**, *21*, 5426.
- (27) Kelly, J. A.; Veinot, J. G. C. *ACS Nano* **2010**, *4*, 4645.
- (28) Jurbergs, D.; Rogojina, E.; Mangolini, L.; Kortshagen, U. *Appl. Phys. Lett.* **2006**, *88*.
- (29) Wilson, W. L.; Szajowski, P. F.; Brus, L. E. *Science* **1993**, *262*, 1242.
- (30) Erogbogbo, F.; Yong, K. T.; Roy, I.; Xu, G. X.; Prasad, P. N.; Swihart, M. T. *ACS Nano* **2008**, *2*, 873.
- (31) Fan, J.; Chu, P. K. *Small* **2010**, *6*, 2080.
- (32) Paniccia, M.; Koehl, S. *IEEE Spectrum* **2005**, *42*, 30.
- (33) Valenta, J.; Juhasz, R.; Linnros, J. *Appl. Phys. Lett.* **2002**, *80*, 1070.
- (34) *Towards the First Silicon Laser*; Kluwek Academic Publishers: Trento, Italy, 2003.
- (35) Fauchet, P. M. *Mater. Today* **2005**, *8*, 26.
- (36) Wolkin, M. V.; Jorne, J.; Fauchet, P. M.; Allan, G.; Delerue, C. *Phys. Rev. Lett.* **1999**, *82*, 197.
- (37) Iwayama, T. S.; Hama, T.; Hole, D. E.; Boyd, I. W. *Vacuum* **2006**, *81*, 179.
- (38) Cheylan, S.; Elliman, R. G. *Appl. Phys. Lett.* **2001**, *78*, 1225.
- (39) Cheylan, S.; Elliman, R. G. *Appl. Phys. Lett.* **2001**, *78*, 1912.
- (40) Neufeld, E.; Wang, S.; Apetz, R.; Buchal, C.; Carius, R.; White, C. W.; Thomas, D. K. *Thin Solid Films* **1997**, *294*, 238.
- (41) Hessel, C. M.; Henderson, E. J.; Veinot, J. G. C. *J. Phys. Chem. C* **2007**, *111*, 6956.
- (42) Choi, J.; Wang, N. S.; Reipa, V. *Langmuir* **2007**, *23*, 3388.
- (43) Shih, S.; Jung, K. H.; Hsieh, T. Y.; Sarathy, J.; Campbell, J. C.; Kwong, D. L. *Appl. Phys. Lett.* **1992**, *60*, 1863.
- (44) Yamamoto, N.; Takai, H. *Thin Solid Films* **2001**, *388*, 138.
- (45) Lehmann, V.; Gösele, U. *Appl. Phys. Lett.* **1991**, *58*, 856.
- (46) V. A. Belyakov, V. A.; V. A. Burdov, V. A.; Lockwood, R.; Meldrum, A. *Adv. Opt. Tech.* **2008**, *2008*, 1.
- (47) Sattler, K. D. *Handbook of nanophysics. Nanoparticles and quantum dots*; Taylor & Francis: Electronic reproduction, 2009.
- (48) *Small Angle X-Ray Scattering* Academic Press: New York, USA, 1982.
- (49) Ilavsky, J.; Jemian, P. R. *J. Appl. Crystallogr.* **2009**, *42*, 347.
- (50) Rong, H.; Jones, R.; Liu, A.; Cohen, O.; Hak, D.; Fang, A.; Paniccia, M. *Nature* **2005**, *433*, 725.
- (51) Ehbrecht, M.; Kohn, B.; Huisken, F.; Laguna, M. A.; Paillard, V. *Phys. Rev. B* **1997**, *56*, 6958.

- (52) Zacharias, M.; Heitmann, J.; Scholz, R.; Kahler, U.; Schmidt, M.; Bläsing, J. *Appl. Phys. Lett.* **2002**, *80*, 661.
- (53) Kahler, U.; Hofmeister, H. *Appl. Phys. A: Mater. Sci. Process.* **2002**, *74*, 13.
- (54) Heitmann, J.; Müller, F.; Zacharias, M.; Gösele, U. *Adv. Mater.* **2005**, *17*, 795.
- (55) Talapin, D. V.; Rogach, A. L.; Kornowski, A.; Haase, M.; Weller, H. *Nano Lett.* **2001**, *1*, 207.
- (56) Knotter, D. M. *J. Am. Chem. Soc.* **2000**, *122*, 4345.
- (57) Ubara, H.; Imura, T.; Hiraki, A. *Solid State Commun.* **1984**, *50*, 673.
- (58) Staebler, D. L.; Wronski, C. R. *Appl. Phys. Lett.* **1977**, *31*, 292.
- (59) Gibson, J. M.; Treacy, M. M. J.; Voyles, P. M.; Jin, H. C.; Abelson, J. R. *Appl. Phys. Lett.* **1998**, *73*, 3093.
- (60) Fritzsche, H. *Ann. Rev. Mater. Res.* **2001**, *31*, 47.
- (61) Ohalloran, G. M.; Kuhl, M.; Trimp, P. J.; French, P. J. *Sensor Actuat. A-Phys.* **1997**, *61*, 415.
- (62) Steinert, M.; Acker, J.; Krause, M.; Oswald, S.; Wetzig, K. *J. Phys. Chem. B* **2006**, *110*, 11377.
- (63) Lockwood, R.; Meldrum, A. *Phys. Status Solidi A* **2009**, *206*, 965.

# Chapter 5:

## Coating of Cylindrical Microcavities with Oxide Embedded Silicon Nanocrystals

*A version of this chapter has been published:*

*Rodríguez Núñez, J. R.; Bianucci, P.; Meldrum, A.; Veinot, J. G.C. Appl. Phys.*

*Lett., 2008, 92, 131119.*

*Bianucci, P.; Rodríguez Núñez J. R.; Clements, C. M.; Veinot, J. G. C., Meldrum,*

*A. J. Appl. Phys., 2009, 105, 023108*

## 5.1. Introduction

The optical properties of silicon nanocrystals in porous silicon, oxide embedded silicon nanocrystals (OE-Si-NCs), and freestanding silicon nanocrystals have been widely investigated.<sup>1-4</sup> The luminescence appears to be related to the combined factors of cluster size, interface effects, and cluster-to-cluster energy transfer mechanisms.<sup>5-7</sup> These properties may lead to practical devices such as light-emitting diodes, waveguide amplifiers, and optical sensors.<sup>8-</sup><sup>10</sup> In addition, a major international push for a Si-NC laser exists.<sup>11</sup> For this and other applications (e.g., sensing), a narrow emission linewidth is desirable.<sup>12,13</sup> Different methods have been utilized to obtain luminescent structures with narrow emission, the two most common being erbium sensitization (see Chapter 2), and the coupling of luminescence to an optical cavity.<sup>14-16</sup> Confinement within a high-quality optical cavity can for instance be used to decrease the lasing threshold.<sup>12</sup> It is well known that the rate of spontaneous emission depends on the environment surrounding the emitting material.<sup>12</sup> The Purcell effect describes the modification of spontaneous emission rates of an given emitter in an optical cavity.<sup>17</sup> The mathematical solution of this problem introduces a quantity called the Purcell factor ( $F_P$ ).<sup>17</sup> This factor describes the effect of the cavity. When  $F_P > 1$  the spontaneous emission rate is increased, conversely, when  $F_P < 1$  emission is inhibited.<sup>17</sup> Rate enhancement is due to an increased density of optical states of the emitter at the cavity mode frequency.<sup>17</sup> In contrast, rate suppression occurs by the absence of photon modes in which the atom can emit.<sup>17</sup>

In this regard, when Si-NCs are placed in a microcavity, the emission rates of wavelengths matching the resonance wavelengths of the cavity are increased, conversely, the emission rates of off-resonance wavelengths suppressed.<sup>18,19</sup> In some cases, this is manifested by the appearance of sharp peaks in the PL spectrum at cavity resonance wavelengths superimposed over the normal broad PL spectrum.<sup>18,20</sup> An ideal cavity will confine the light indefinitely, without loss, yielding sharp resonance frequencies.<sup>12</sup> However, in real cavities, resonances are broadened due to inherent energy losses (e.g., radiation, scattering, or absorption losses). The  $Q$ -factor is a figure of merit that quantifies the losses of an optical cavity.<sup>21</sup> The  $Q$ -factor is calculated by the ratio of the mode wavelength and the full-width-at-half-maximum of the mode (1)<sup>21</sup>

$$Q = \frac{\lambda}{FWHM} \quad (1)$$

The higher the  $Q$ -factor, the lower the losses.<sup>21</sup>

A variety of cavity structures containing Si-NCs have been reported, including planar cavities, microdisks, and coated microspheres (Figure 5.1).<sup>15,18,20,22,23</sup> These studies reported cavity  $Q$ -factors ranging from several hundred for planar cavities up to 1200-1500 for coated microspheres.  $Q$ -factors of  $\sim 10^5$  have been found for SiO<sub>x</sub>-coated silica spheres, although the coupling of the nanocrystal fluorescence into these modes was not demonstrated.<sup>24</sup> Whispering-gallery-mode (WGM) resonators possess high  $Q$ -factors making them potential candidates for the development of a Si-NC laser.<sup>12</sup> Although these studies have shown promising results, the common physical methods used to

prepare cavity structures are relatively costly, time consuming, and require the use of advanced equipment. Furthermore, the line-of-sight techniques used for coating non-planar surfaces with Si is non-trivial. By comparison, hydrogen silsesquioxane (HSQ) is a versatile precursor for preparing oxide embedded or freestanding Si-NCs that sidestep the above issues almost entirely.<sup>25-27</sup> HSQ is routinely used as a spin-on dielectric, has excellent gap-fill, and is solution processable.<sup>28</sup> OE-Si-NCs can be prepared by heating HSQ at temperatures higher than 1100 °C.<sup>25,26</sup> Thus, taking into consideration the aforementioned properties, HSQ is an ideal precursor to coat non-planar microcavities with OE-Si-NCs.

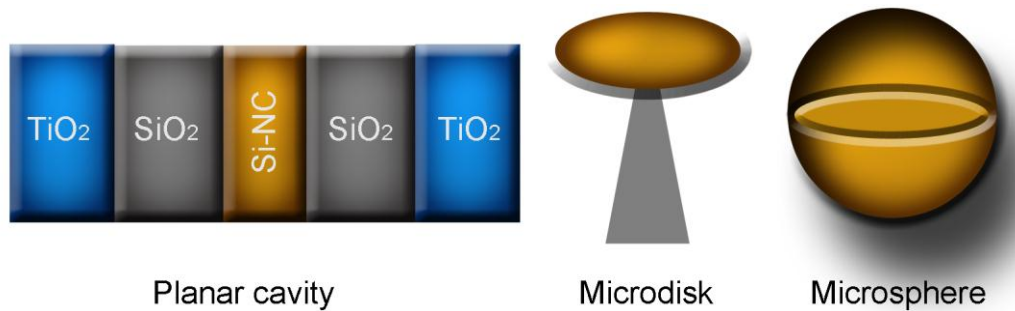


**Fig. 5.1** Schematic of planar, disk, and sphere microcavities. (Adapted from Ref. 22 and Ref. 12)

WGMs are optical resonance modes which propagate around circular or spherical optical cavities through total internal reflection (TIR).<sup>29</sup> WGMs can be described as ray trajectories where the angle of incidence on the cavity-medium interface is such that it experiences TIR. TIR reflects all of the incident energy and it occurs when light encounters a material with lower refractive index.<sup>30,31</sup>

This chapter outlines a method to coat non-planar microcavities (capillaries and fiber optics) with OE-Si-NCs. In the structures studied, a layer of Si-NCs is “sandwiched” between two media (air and silica). A preliminary report on the effect of changing the refractive index of the media surrounding fiber optics exhibiting WGMs is studied by dipping the fibers in a solution of varying concentrations of ethylene glycol and glucose.

## **5.2. Experimental Details**

### **5.2.1. Materials preparation**

The capillaries used for the present study were polyimide coated fused silica capillary tubes (Polymicro Technologies) with inner diameters (I.Ds) of 100, 50, and 25  $\mu\text{m}$ , and outer diameter of  $\sim 360 \mu\text{m}$ . The polymer coating was removed by placing the capillaries in boiling concentrated sulphuric acid followed by sequential rinsing with distilled water and “piranha” solution (i.e., 3:1  $\text{H}_2\text{SO}_4:\text{H}_2\text{O}_2$ ) for a minimum of 30 minutes. The capillaries were subsequently rinsed with distilled water, flame dried, and the interior loaded with a HSQ solution immediately using capillary forces.

Fiber optics were prepared by mechanically stripping and cleaving regular SMF-28 single-mode optical fibers with a cladding diameter of 125 nm. In order to form the exterior Si-NC coating, the fibers were initially cleaned with hot concentrated sulphuric acid, but in subsequent experiments isopropyl alcohol cleaning also gave satisfactory results.

### **5.2.2. Coating of Cylindrical microcavities with OE-Si-NCs**

HSQ dissolved in methyl-isobutylketone (MIBK) was purchased from Dow Corning Corp. (tradename FOx XX where XX relates to the weight percent of HSQ in solution). FOx 15 was drawn into capillaries of different inner diameters (25  $\mu\text{m}$ , 50  $\mu\text{m}$  and 100  $\mu\text{m}$ ) by capillary forces. The capillaries were heated in a tube furnace under a reducing atmosphere 95% Ar, 5%  $\text{H}_2$  from room temperature to 300  $^\circ\text{C}$  at 5  $^\circ\text{C}/\text{min}$  where they remained for 2 h. This allows for

complete solvent removal below the temperature where cage rearrangement occurs (see Chapter 1).<sup>26</sup> The temperature was subsequently increased to 1100 °C at a rate of 18 °C/min and maintained for 1 h. The capillaries were then cooled to room temperature at a rate of 2 °C/min. After thermal processing, the interior of the fibers possessed the characteristic orange/brown appearance of oxide-embedded Si-NC composite films. Red photoluminescence is observed after photoexcitation of these structures. The observed luminescence does not shift over a period of months, suggesting that the films are air stable after thermal processing.

Fiber optics were dipped in a solution of HSQ (FOx 16 was used in all the studies presented below although FOx 15 produces comparable results). The fibers were left in the solution for at least 30 s to ensure thorough wetting of the surface. After withdrawing from the solution, a thin film remained held on the fiber surface by surface tension. As the fibers were dried in the vertical position, some gradual variation in the coating thickness may occur along their length.<sup>27</sup> The coated fibers were then heated at an approximate rate of 15 °C/min to 1100 °C in a slightly reducing atmosphere (5% H<sub>2</sub> / 95% Ar), forming a film of OE-Si-NCs.

### **5.2.3. Materials Characterization**

#### **5.2.3.1. Photoluminescence Imaging and Spectroscopy**

Photoluminescence (PL) imaging and spectroscopy were performed using a Nikon TE2000 inverted microscope (with the 488 nm line of an Ar<sup>+</sup> laser as the excitation source). The fluorescence was collected perpendicular to the fiber axis (except when studying confinement along the z-axis) and was spectrally dispersed in a grating spectrometer with a manufacturer-quoted spectral resolution of 0.24 nm. PL spectra were corrected for the system spectral response with a standard blackbody light source of known color temperature. This setup provides both spatially and spectrally resolved images of the emitted PL. For ethylene glycol and glucose measurements the fiber was dipped into a water-based solution contained within a home-built cuvette fitted onto the microscope stage, enabling *in situ* measurement of the WGM structure with the NC coated fiber situated in a variety of different local environments.

#### **5.2.3.2. Scanning Electron Microscopy**

SEM was used to measure the film thickness of OE-Si-NCs coated capillaries and fiber optics. All samples were coated with chromium using an Edwards Xenosput XE 200 coater. Secondary electron images were collected using a JEOL 6301F field emission SEM.

#### **5.2.4. Capillary and Fiber Optic mode indexing**

A theoretical analysis was performed by Dr. Pablo Bianucci to model the mode spectra by using the capillary (fiber) inner diameter (diameter), film thickness, and refractive index as variable parameters. The mathematical detail of this model can be found in Appendix B.

### **5.3. Results and Discussion**

#### **5.3.1. Whispering-Gallery Modes in Capillaries**

Cavities coated with luminescent materials are of substantial interest because of their potential application in the development of lasers, sensors, and other applications.<sup>8-10,12,13</sup> Capillaries filled with a solution of CdSe/ZnS core-shell quantum dots lase upon optical excitation.<sup>32</sup> The development of a silicon-based laser has been intensively pursued by the international research community and was achieved by Rong et al. at Intel Corporation® in a contribution entitled “A continuous-wave Raman silicon laser”.<sup>33</sup> Mario Pannicia and Sean Koehl from Intel Corporation’s Photonics Technology Lab in Santa Clara, California suggest a silicon-based laser could revolutionize how computers operate.<sup>34</sup> Pannicia and Koehl strongly suggest that a Raman laser may be all that is needed to initiate a new era in computing. However, development of other methods for fabricating Si-based lasers can help move this area of photonics forward. Creation of a Si-based laser will be aided by the development of inexpensive, straightforward procedures that afford luminescent silicon materials coupled to microcavities. Although microcavities coated with OE-Si-NCs will likely impact the field of computing, it is expected they will have a more immediate impact in the development of inexpensive, portable sensors.<sup>35</sup> If the modal field extends outside the cavity, the peaks observed in the PL spectrum can shift in response to a change in medium refractive index.<sup>35</sup> Based upon this response, a sensor can be designed.

Capillaries and fiber optics are suitable structures for sensing applications and are compatible with numerous analytical techniques. For the present study, capillaries were coated by loading them with HSQ after cleaning. Following thermal processing, the interior of the capillaries was coated with a brown film that was readily observed in larger diameter capillaries (i.e., 100  $\mu\text{m}$  I.D.) (See: Figure 5.2). The coating is not uniform along the capillary walls. At the ends of the capillaries the film may be cracked and appears thicker (Figure 5.2.b). The film becomes smooth, uniform and crack free over large areas upon moving to the interior of the capillary. The OE-Si-NC films possess more defects when prepared in larger inner diameter capillaries.

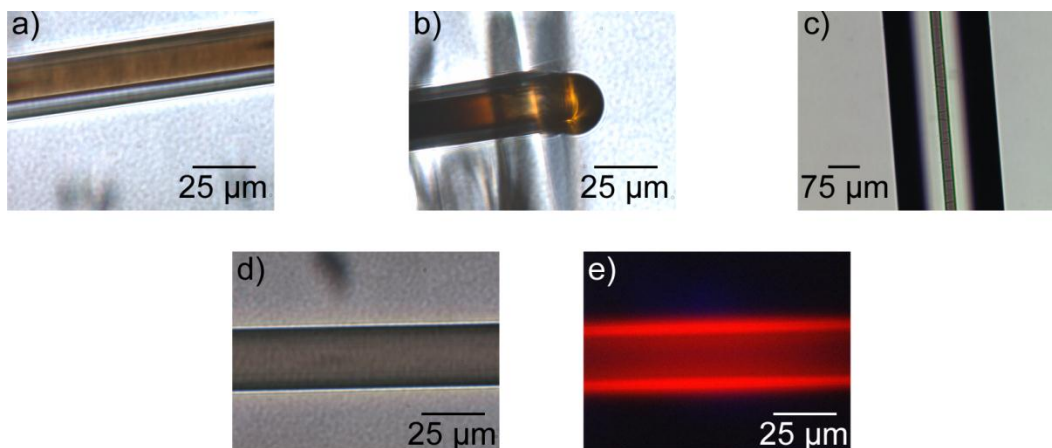


**Fig 5.2** a), b) Films of OE-Si-NCs in 25  $\mu\text{m}$  capillaries, the dark brown colour suggests the film is thick c) Defect-free films. d) 50x magnification of a section from c). Optical luminescence image of an OE-Si-NC film excited using the 488 nm line of an Ar<sup>+</sup> laser.

A 25  $\mu\text{m}$  I.D. capillary, cleaved in a region of uniform coating, revealed a film thickness of ca. 600 nm by SEM. Films in 50  $\mu\text{m}$  I.D. capillaries display more cracks and are approximately 1.5  $\mu\text{m}$  thick, based upon modeling of the WGM response obtained from these structures (*vide infra*). Optical microscopy of OE-Si-NC coated 100  $\mu\text{m}$  I.D. capillaries show many cracks, making further evaluation of the film thickness impossible. The cracks observed in the larger capillaries are attributed to delamination of the thick films, consistent with a report from Hessel et al.<sup>27</sup>

PL spectra of OE-Si-NC films were obtained by pumping the capillaries with the 488 nm line of an  $\text{Ar}^+$  laser interfaced to a fluorescence microscope. The film appeared in a cross sectional optical microscopy image as a well-defined red fluorescent ring coating the inner surface of the capillary (Figure 5.3.c). The red PL penetrates into the inner diameter of the lower-index capillary slightly consistent with the presence of guided and “leaky” modes extending along the film and the inner region of the capillary. The PL spectrum peaked at 810 nm, typical of ensembles of OE-Si-NCs. A weak mode structure was observed in the PL spectrum taken from this “end on” orientation (Figure 5.3.b). It may arise from the interference of guided or “leaky” modes within light propagating along the inner length of the capillary. The  $Q$ -factors for the modes shown in Figure 5.3 are uniformly low,  $\sim 100$ , and are therefore of relatively little interest for the formation of a high- $Q$  cavity structure needed for sensing or lasing applications.

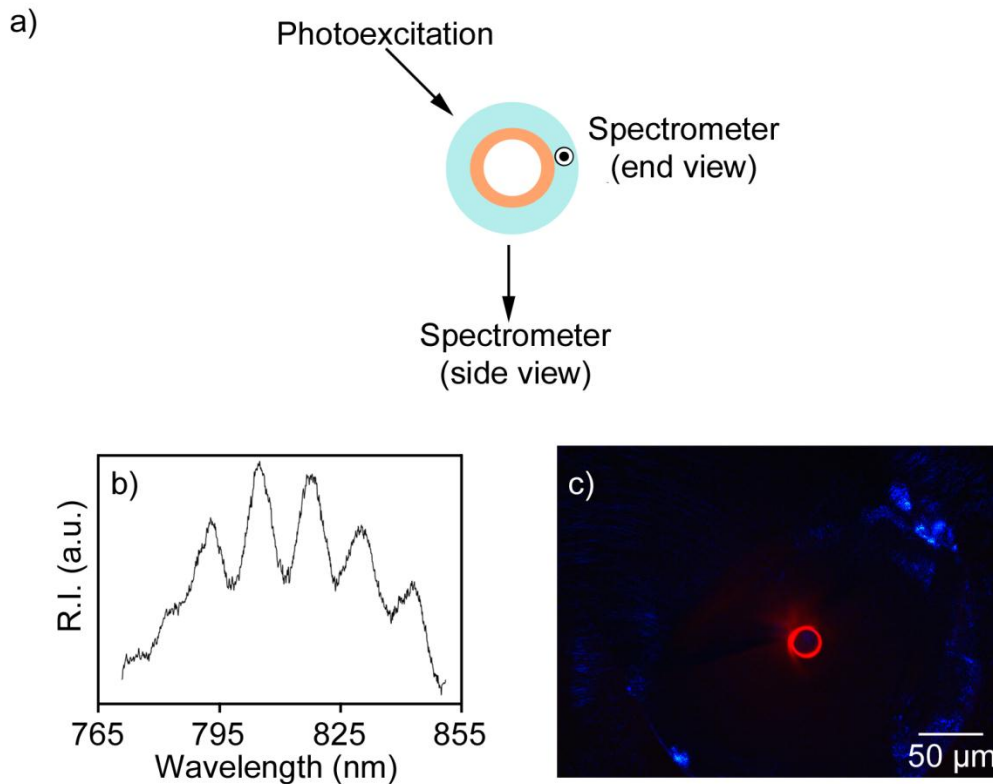


**Fig. 5.3** a) Schematic of the experiment. The capillary (light blue) coated with OE-Si-NCs (light orange) is excited from the side using the 488 nm line of an  $\text{Ar}^+$  laser. The PL is collected by a microscope lens located under the capillary. b) Representative PL spectrum taken from the end of a 25  $\mu\text{m}$  capillary. Low  $Q$ -factors (ca. 100) are obtained when upon collecting the light from the end of the capillary. c) Fluorescence image of the tip of a 25  $\mu\text{m}$  inner diameter capillary, in which the blue pump laser light defines the outer diameter of the capillary.

In contrast, imaging and spectroscopy of the Si-NC fluorescence collected perpendicular to the long axis of the capillaries show an extremely sharp, well-formed mode structure, consistent with the formation of WGMs (Figure 5.4.a).

The refractive index contrast between the higher-index OE-Si-NC film and its surrounding media (air and the fused silica capillary) clearly confines the Si-NC luminescence within the inner capillary radius as shown in Figures 5.2.e, and 5.3.c.

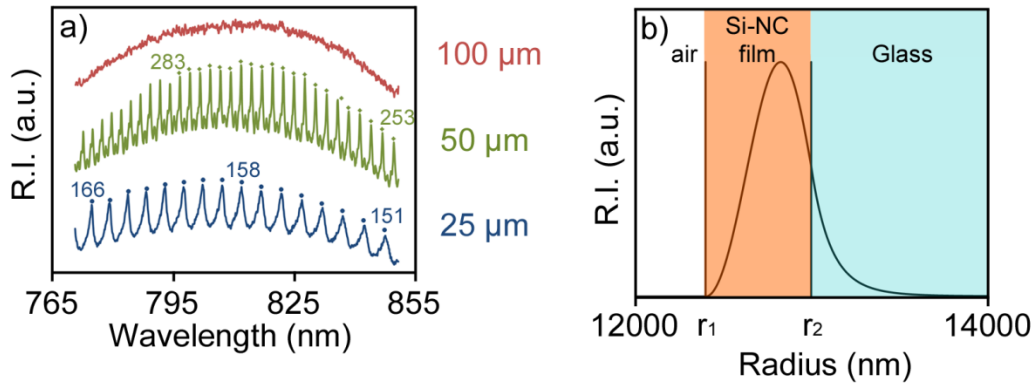


**Fig. 5.4** a) PL spectra of 100, 50, and 25 μm capillaries taken perpendicular to the axis. Dots above the spectra show modeling data (solving Eq. (1) and (2)) for first-order modes. c) Theoretical intensity profile (derived from Eq. 4) for the luminescence from a cylindrical WGM in a 25 μm inner-diameter capillary.

$Q$ -factors for the WGMs confined within the cylindrical optical cavity structures were evaluated for different cavity dimensions.  $Q$ -factors improved as modes became more defined, narrower, and more closely spaced as the I.D. increases from 25 μm to 50 μm. In addition, the spectrum for the 50 μm capillary showed well-defined first-order modes as well as higher-order radial modes of lower PL intensity consistent with the thicker film. These observations are

consistent with predicted behavior; as the inner diameter of the hollow fiber increases, the mode spacing decreases as described by equation 5:<sup>21</sup>

$$2\pi r = m(\lambda_n) \quad (5)$$

where  $r$  is the cavity radius,  $m$  is an integer representing the number of modes available for one wavelength,  $\lambda_n$  is a wavelength of light travelling within the cavity in a medium with refractive index  $\eta$ . Light of wavelength  $\lambda_n$  satisfying (5) will experience total constructive interference and will appear as a peak in the PL spectrum. As  $r$  increases,  $m$  must also increase. For this reason, as  $r$  increases, an increased number of modes will appear in the same spectral region resulting in decreased mode spacing. Thus, as the cavity radius increases the losses will decrease and the  $Q$ -factors increase.

Capillaries with inner diameters of 100  $\mu\text{m}$  showed no indication of WGMs, due to the extensive cracking observed in the film. To calculate the  $Q$ -factors, the PL background was subtracted from the 50 and 25  $\mu\text{m}$  spectra by using a baseline removal procedure (fitting PL to a Gaussian function to remove the background). The linewidths were measured in the resulting spectrum. The 1.3 nm FWHM of the 25  $\mu\text{m}$  capillary results in  $Q \sim 630$ , while the 0.3 nm FWHM (possibly instrument limited by the manufacturer-quoted ultimate spectrometer resolution of 0.2 nm) of the modes in the 50  $\mu\text{m}$  capillary gave a  $Q$ -factor of  $\sim 2500$ . These values are comparable to other  $Q$ -factors reported for the fluorescence of Si-NCs which range from 100 in planar cavities to 1500 for coated microspheres.

### **5.3.2. Whispering-Gallery Modes in Fiber Optics**

The success of coating the I.D. of capillaries with OE-Si-NCs is largely dependent on HSQ being drawn into the microcavity. Even though great care is taken to cleave the capillaries without damaging the opening, there are instances when no NC film is observed after thermal processing – this results from the ends of the capillary being closed off during the cleaving procedure. Other capillaries show films inside the cavity with orange photoluminescence (as opposed to the normal red PL) and do not exhibit WGMs. This observation may result from residual water, sulfuric acid, or hydrogen peroxide remaining inside the capillary after the cleaning procedure. Water can crosslink HSQ, affecting the silicon to oxygen ratio, which will in turn influence the optical properties. In addition, we have previously observed that thin films of HSQ prepared on “piranha cleaned” silicon substrates experience delamination upon thermal processing if the sulfuric acid/hydrogen peroxide mixture is not completely removed. Regardless of the origin of these defects, the success rate of the process to coat the inside of capillaries was approximately 50%.

A structure that could prove more successful in providing efficient optical cavities is a fiber optic because it does not require coating the interior surface of a tube, it is merely involves coating of an outer surface. The fabrication method described in Section 5.2.2 permitted the formation of a smooth, homogeneous OE-Si-NC layer on the outer surface of the silica fiber (Figure 5.5.a). The film was typically crack-free over distances a few hundreds of micrometers. In cross-section, the OE-Si-NC film is approximately 70 nm thick (Figure 5.5.b). This

observation gave credence to the hypothesis that the film thickness is the most important factor causing delamination in capillaries at the sizes studied. The OE-Si-NC films in these images appear smooth in optical and scanning electron microscopy suggesting that the surface roughness was at least smaller than 10 nm. Figure 5.5.c shows a transmitted-light image of a coated fiber with no laser excitation; the OE-Si-NC film appears as a yellow-brown coating. When pumped with the 488 nm line of an Ar<sup>+</sup> laser, a bright red PL associated with OE-Si-NC was observed (Figure 5.5.d). Control fibers were also annealed without HSQ; in those samples, no emission could be detected.

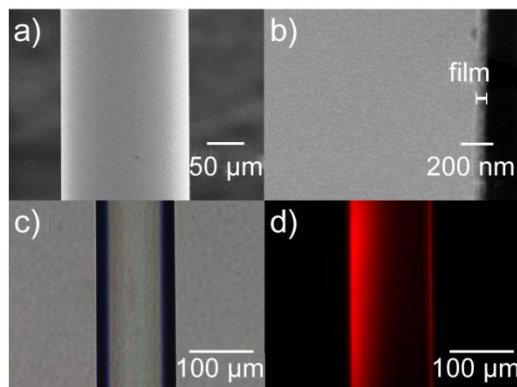


**Fig. 5.5** a) SEM image of a Si-NC-coated fiber, with a smooth, crack-free coating. b) Cross-sectional SEM image showing a 70-nm-thick NC film on the fiber surface. SEM images were obtained using a 5 keV beam in the secondary electron imaging mode. c) Optical microscope image of a 125- $\mu$ m-wide Si-NC-coated fiber. d) PL image of the fiber in c) excited by the 488 nm line of an Ar<sup>+</sup> laser incident from the left side of the image.

The spectral intensity profile is shown in Figure 5.6.a and b. It is clear the PL is brightest at the fiber boundaries. Figure 5.6.b also highlights the fact that the PL decays suddenly at the film-glass interface. The PL spectrum show a clearly defined mode structure superimposed on a background PL centered at 750 nm (Figure 5.6.c inset). A high resolution image of the peaks observed shows a FWHM of a fraction of a nanometer (nearly equal to the manufacturer-specified resolution of the detector, just as for the 50  $\mu\text{m}$  I.D. capillary) corresponding to  $Q$ -factors of approximately 2500 for the narrowest ones, among the highest reported to date for silicon NCs and for NC fluorescence.<sup>20</sup> The measured PL  $Q$ -factors are already considerably higher than observed for spherical cavities coated with CdSe NCs.<sup>36</sup> The high  $Q$ -factors reported here are partly the result of the smooth surface of the NC film which reduces scattering losses present in lithographically defined cavities with Si-NCs.<sup>18,37</sup> The agreement between the observed spectra and the calculated mode resonances is excellent (peak fitting for one mode is shown in Figure 5.6.c). The values obtained for film thickness are in agreement with the measured values from SEM. The refractive index obtained is consistent with literature values ( $n_{\text{film}} = 1.6$ ).<sup>22</sup> These observations indicate that the modes are indeed cylindrical WGMs.

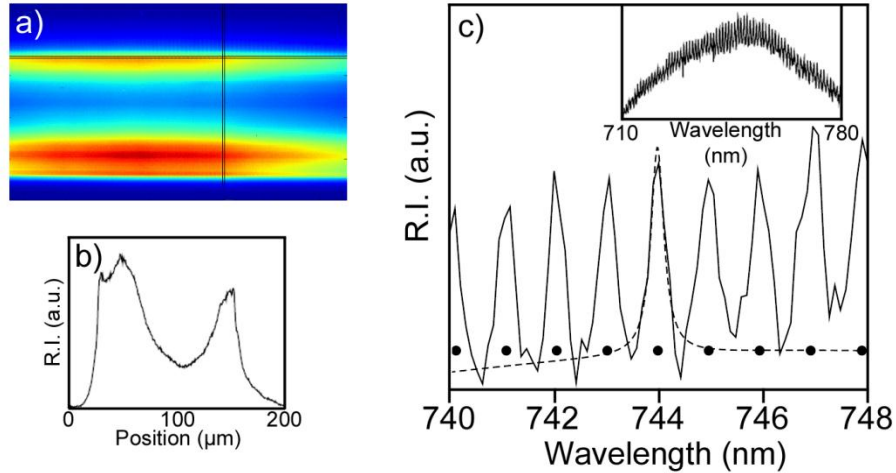


**Fig. 5.6.** a) Spectral image of a Si-NC-coated fiber, where intensity increases from blue to red. b) Spatial profile of the emission taken along the direction of the black line shown. c) Magnified view of a section of mode spectrum showing the WGM structure in more detail. The dashed line corresponds to a numerical fit using a single Lorentzian on top of a Gaussian background. The black circles represent calculated resonant solutions for radial index  $p=1$  for angular mode numbers  $l$  between 752 and 760. Inset shows a profile across the direction of intense PL of the image in a), the resonant peaks are clearly visible over a broad PL background.

For a fiber optic coated with OE-Si-NCs, the mode structure arises because of the confinement provided by the index contrast between the glass and the outside medium (e.g., air) (Figure 5.4.c and 5.6.a). Since the modal field extends outside the fiber, changes in the optical environment will induce a shift in the resonant frequencies. This effect forms the basis of WGM sensing or detection devices. The presence of the thin, high-index OE-Si-NC layer introduces a small red-shift in the cavity resonances compared to an uncoated

fiber as described by Teraoka et al., but does not adversely affect the capability of refractive index sensing.<sup>38</sup> In fact, the high-index coating may increase the overall sensitivity.<sup>39</sup> In general, the narrow linewidths of the WGM resonances permit sensitive measurements of the surrounding refractive index. There have been many reports of WGMs in cylindrical, spherical, and ring microcavities and their application to chemical and biological sensing.<sup>35,40</sup>

In order to demonstrate a proof-of-concept sensing capability for OE-Si-NC-coated fibers, an apparatus was built to enable the coated fibers to be dipped into test solutions while keeping them at a fixed focal position of the microscope. Mixtures of water and ethylene glycol (EG) or water and glucose were evaluated during these experiments. Figure 5.7 illustrates spectral shifts in the PL spectra of OE-Si-NC-coated fibers immersed in 2.5 mL of water. Small amounts of either EG (in 0.05 mL increments, Figure 5.7a) or a concentrated ( $\sim 2 \times 10^4$  mg/dL) glucose solution (in 0.1 mL increments, Figure 5.7b) were added to the water and the PL spectrum was collected. The addition of EG and glucose increases the refractive index of the mixture  $\eta_{\text{water}}=1.33$ ,  $\eta_{\text{EG}} = 1.4325$ , and  $\eta_{\text{glucose}} = 1.3552$  at the high concentrations in the stock solutions as shown by equation (6).<sup>41</sup> As a result of the increased refractive index ( $\eta$ ), a shift of the modes to longer wavelength is observed.

$$\eta_{\text{solution}} = \eta_{\text{water}} \times \text{fraction of water} + \eta_{\text{solute}} \times \text{fraction of solute} \quad (6)$$

Figure 5.7 shows the PL spectra of OE-Si-NC fibers in solutions with increasing solute concentration. WGM shifts were quantitatively extracted by

subtracting the background PL followed by fitting the mode peaks with Lorentzian curves. The precision in the measured shifts is expected to be limited by the spectral resolution of the detector, because the FWHM of the WGMs are approximately equal to the manufacturer-quoted spectrometer resolution. The figure insets show the shift in WGMs as a function of the solute concentration and the calculated refractive index of the mixture. There is a linear relationship between the observed shift in WGM resonance and the analyte concentration. Fitting the data gives slopes of  $0.026 \pm 0.005$  nm/%V<sub>EG</sub> and  $26 \pm 5$  nm/RIU for the EG and  $3.8 \pm 0.9 \times 10^{-4}$  nm/mg/dL and  $33 \pm 8$  nm/RIU for the glucose solutions. Calculated resonance wavelengths are also shown as a function of the refractive index of the solution dashed lines in the insets of Figure 5.7. Good agreement was obtained between experiment and theory for the glucose solution; for EG, the observed resonance shifts are slightly greater than those predicted by theory. This underestimation may result from the declining signal-to-noise ratio as the refractive index of the solution approached that of the fiber.

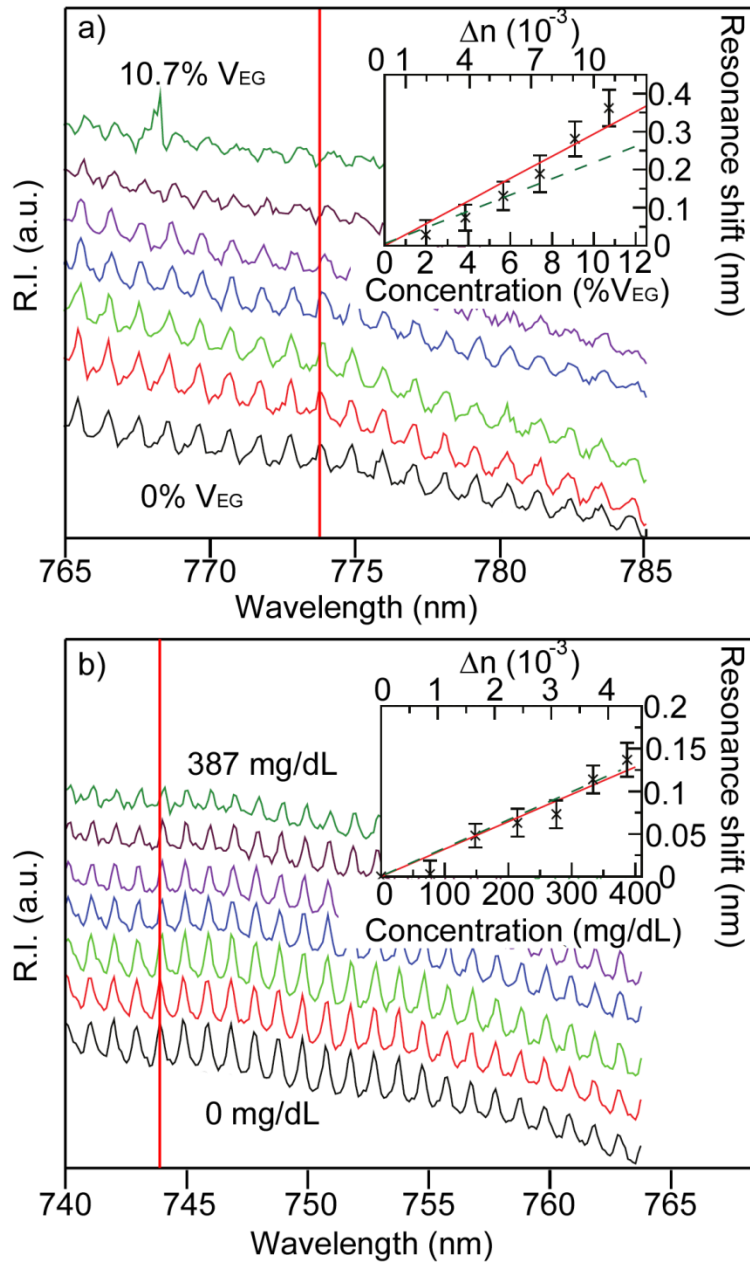


**Fig. 5.7** WGM spectra for different concentrations of a) EG and b) glucose in water. Insets: Resonance peak shift as a function of the concentration and the refractive index change for the peak marked with the red line. The solid and dashed lines are the best fit and calculated mode shifts, respectively.  $R^2$  values are better than 0.95 for both linear fits shown.

The demonstrated sensitivity to medium refractive index changes is approximately 33 nm/RIU, comparable to evanescent measurements of microsphere resonators,<sup>42</sup> but not currently as high as that reported in evanescent measurements of WGMs for HF-thinned capillaries.<sup>43,44</sup> The figure of merit for the present resolution-limited fluorescent configuration ( $\Delta\lambda_{\text{FWHM}}/(d\lambda/d\eta)$ ) is approximately  $7.2 \times 10^{-3}$  RIU, which is low in contrast to the  $10^{-7}$  RIU reported for evanescent measurements.<sup>45</sup>

The selectivity of this proof-of-concept sensor is questionable at best. The insets of Figure 5.7.a and b show that a similar resonance shift can be detected using different analytes. A more selective sensor can be designed by covalently binding a large molecule to the surface that selectively binds the analyte. This binding can cause a change in the refractive index changing the modal field. Specific sensors using similar methodology has been demonstrated in the literature.<sup>46,47</sup> However, the  $Q$ -factors in these cavities are low ( $< 100$ ). Coupling chemical functionalization with the high  $Q$  cavities obtained by coating capillaries or fiber optics with OE-Si-NCs can produce sensors that are highly sensitive and selective.

## 5.4. Conclusions

In summary, the experiments described in this chapter demonstrate a straightforward and inexpensive method to coat non-planar surfaces with a uniform film of OE-Si-NC. Photons produced in these structures, by photoexcitation of the NCs, experience confinement due to the refractive index contrast between the film and surrounding media. This confinement gives rise to WGMs observable in the PL spectra. In capillaries, the WGMs are narrow with  $Q$ -factors as high as 2500 for the 50  $\mu\text{m}$  inner diameter. Similar  $Q$ -factors were obtained for 125  $\mu\text{m}$  diameter fiber optics. Given that the measured mode widths are nearly equal to the quoted spectrometer resolution, it is possible that the actual  $Q$ -factors may be even higher. The high quality modes can be attributed in part to the smoothness and uniformity of the cylindrical films prepared by this method. This coating method can be readily extended to prepare other microcavity structures, both planar and non-planar.

A proof-of-concept refractometric sensing method was also demonstrated. This method relates the resonance shift with a change in concentration of ethylene glycol or glucose in water. The utilization of a high  $Q$ -factor optical cavity in which the fiber itself supplies both the fluorescence and the microcavity structure is different from previous fluorescence sensors. The figure of merit ( $\Delta\lambda_{\text{FWHM}}/(d\lambda/d\eta)$ ) of this measurement technique as implemented is currently low, but higher-resolution spectroscopy will likely increase it, while at the same time lowering the detection limits. Also, because the NCs are embedded in a silica

film they are well protected from the surrounding media, so that fluorescent devices made in this way are durable and, in principle, reusable.

Although the sensitivity of this proof-of-concept sensor can be improved, its selectivity remains questionable. Future work in this area may encompass using well-understood surface functionalization procedures for silica surfaces to covalently bind molecules to the film's surface.

## 5.5. References

- (1) Canham, L. T. *Appl. Phys. Lett.* **1990**, *57*, 1046.
- (2) Cullis, A. G.; Canham, L. T.; Calcott, P. D. J. *J. Appl. Phys.* **1997**, *82*, 909.
- (3) Meldrum, A.; Hryciw, A.; Buchanan, K. S.; Beltaos, A. M.; Glover, M.; Ryan, C. A.; Veinot, J. G. C. *Opt. Mater.* **2005**, *27*, 812.
- (4) Veinot, J. G. C. *Chem. Commun.* **2006**, 4160.
- (5) Heitmann, J.; Müller, F.; Zacharias, M.; Gösele, U. *Adv. Mater.* **2005**, *17*, 795.
- (6) Biteen, J. S.; Lewis, N. S.; Atwater, H. A.; Polman, A. *Appl. Phys. Lett.* **2004**, *84*, 5389.
- (7) Lockwood, R.; Hryciw, A.; Meldrum, A. *Appl. Phys. Lett.* **2006**, *89*.
- (8) Valenta, J.; Lalic, N.; Linnros, J. *Opt. Mater.* **2001**, *17*, 45.
- (9) Clement, T. J.; DeCorby, R. G.; Ponnampalam, N.; Allen, T. W.; Hryciw, A.; Meldrum, A. *Opt. Express* **2006**, *14*, 12151.
- (10) Tewary, A.; Dignonnet, M. J. F.; Sung, J. Y.; Shin, J. H.; Brongersma, M. L. *IEEE J. Sel. Top. Quant.* **2006**, *12*, 1476.
- (11) *Towards the First Silicon Laser*; Kluwer Academic Publishers: Dordrecht, The Netherlands, 2003; Vol. 93.
- (12) Vahala, K. J. *Nature* **2003**, *424*, 839.
- (13) Chan, S.; Li, Y.; Rothberg, L. J.; Miller, B. L.; Fauchet, P. M. *Mater. Sci. Eng., C* **2001**, *15*, 277.
- (14) Polman, A. *J. Appl. Phys.* **1997**, *82*, 1.
- (15) Iacona, F.; Franzò, G.; Moreira, E. C.; Priolo, F. *J. Appl. Phys.* **2001**, *89*, 8354.
- (16) Chan, S.; Fauchet, P. M. *Opt. Mater.* **2001**, *17*, 31.
- (17) Fox, M. *Quantum optics: an introduction*; Oxford University Press: Electronic reproduction, 2006.
- (18) Beltaos, A. M.; Meldrum, A. *J. Lumin.* **2007**, *126*, 607.
- (19) Iacona, F.; Franzò, G.; Ceretta Moreira, E.; Pacifici, D.; Irrera, A.; Priolo, F. *Mater. Sci. Eng., C* **2002**, *19*, 377.
- (20) Zhang, R. J.; Seo, S. Y.; Milenin, A. P.; Zacharias, M.; Gösele, U. *Appl. Phys. Lett.* **2006**, *88*.
- (21) Saleh, B. E. A.; Teich, M. C. *Fundamentals of Photonics*; 2nd Ed. ed.; Wiley: New Jersey, USA, 2007.
- (22) Amans, D.; Callard, S.; Gagnaire, A.; Joseph, J.; Ledoux, G.; Huisken, F. *Mat. Sci. Eng. B-Solid* **2003**, *101*, 305.
- (23) Hryciw, A.; Laforge, J.; Blois, C.; Glover, M.; Meldrum, A. *Adv. Mater.* **2005**, *17*, 845.
- (24) Sung, J. Y.; Tewary, A.; Brongersma, M. L.; Shin, J. H. *IEEE J. Sel. Top. Quant.* **2006**, *12*, 1388.
- (25) Hessel, C. M.; Henderson, E. J.; Veinot, J. G. C. *Chem. Mater.* **2006**, *18*, 6139.

- (26) Hessel, C. M.; Henderson, E. J.; Veinot, J. G. C. *J. Phys. Chem. C* **2007**, *111*, 6956.
- (27) Hessel, C. M.; Summers, M. A.; Meldrum, A.; Malac, M.; Veinot, J. G. C. *Adv. Mater.* **2007**, *19*, 3513.
- (28) Loboda, M. J.; Grove, C. M.; Schneider, R. F. *J. Electrochem. Soc.* **1998**, *145*, 2861.
- (29) *An introduction to optoelectronic sensors*; World Scientific: Electronic reproduction, 2009; Vol. 7.
- (30) Smith, W. F. *Waves and oscillations : a prelude to quantum mechanics*; Oxford University Press: New York, USA, 2010.
- (31) Young, H. D.; Freedman, R. A. *University Physics*; 11th Ed. ed.; Pearson Education: San Francisco, USA, 2004.
- (32) Kazes, M.; Lewis, D. Y.; Banin, U. *Adv. Funct. Mater.* **2004**, *14*, 957.
- (33) Rong, H.; Jones, R.; Liu, A.; Cohen, O.; Hak, D.; Fang, A.; Paniccia, M. *Nature* **2005**, *433*, 725.
- (34) Paniccia, M.; Koehl, S. *IEEE Spectrum* **2005**, *42*, 30.
- (35) Vollmer, F.; Arnold, S. *Nature Methods* **2008**, *5*, 591.
- (36) Gómez, D. E.; Pastoriza-Santos, I.; Mulvaney, P. *Small* **2005**, *1*, 238.
- (37) Kekatpure, R. D.; Brongersma, M. L. *Phys. Rev. A: At., Mol., Opt. Phys.* **2008**, *78*.
- (38) Teraoka, I.; Arnold, S. *J. Opt. Soc. Am. B: Opt. Phys.* **2007**, *24*, 653.
- (39) Teraoka, I.; Arnold, S. *J. Opt. Soc. Am. B: Opt. Phys.* **2006**, *23*, 1434.
- (40) Lambeck, P. V. *Meas. Sci. Technol.* **2006**, *17*, R93.
- (41) Yunus, W. M. B.; Rahman, A. B. *Appl. Opt.* **1988**, *27*, 3341.
- (42) Hanumegowda, N. M.; Stica, C. J.; Patel, B. C.; White, I.; Fan, X. *Appl. Phys. Lett.* **2005**, *87*, 1.
- (43) Zamora, V.; Díez, A.; Andrés, M. V.; Gimeno, B. *Opt. Express* **2007**, *15*, 12011.
- (44) Sumetsky, M.; Windeier, R. S.; Dulashko, Y.; Fan, X. *Opt. Express* **2007**, *15*, 14376.
- (45) White, I. M.; Zhu, H.; Suter, J. D.; Hanumegowda, N. M.; Oveys, H.; Zourob, M.; Fan, X. *IEEE Sens. J.* **2007**, *7*, 28.
- (46) Lin, V. S. Y.; Motesharei, K.; Dancil, K. P. S.; Sailor, M. J.; Ghadiri, M. R. *Science* **1997**, *278*, 840.
- (47) Schwartz, M. P.; Alvarez, S. D.; Sailor, M. J. *Anal. Chem.* **2007**, *79*, 327.

**Chapter 6:**

**Conclusions**

**and**

**Future Work**

## 6.1. Conclusions

Over the last two decades, research in nanosized materials has made giant strides.<sup>1</sup> The interest fueling this development arises from the unique properties that some materials possess when one or more dimensions have less than 100 nm.<sup>2</sup> The manufacturing of materials and structures in the nanometer scale is a natural technological progression that started with the miniaturization of transistors as predicted by Moore in the mid-1960s.<sup>3</sup> Quantum dots are semiconductor nanocrystals with unique size related properties.<sup>4</sup> These structures have been suggested for applications in medicine, biology, sensing, among others.<sup>5-7</sup> The most common QDs use elements from Group II, III, V, VI, with CdSe being the workhorse material in this field. Unfortunately, many of these elements are toxic even in small quantities.<sup>8</sup> This toxicity may render particles made with these elements inappropriate for a number of applications. For example, in 2004 the European Union banned cadmium based electronics due to toxicity concerns.<sup>9,10</sup> The scientific community is switching their attention to less toxic materials. Silicon is an attractive alternative. It is an essential nutrient that oxidizes in the body to form silicic acid which is readily cleared by the kidneys.<sup>11,12</sup> Silicon nanocrystals (Si-NCs) with a diameter close to the Bohr exciton radius (ca. 5 nm) exhibit luminescence that arises from quantum confinement and are expected to be less toxic than their II-VI and III-V counterparts.<sup>2,13</sup> In addition to medical and biological applications, Si-NCs are of great interest for computing applications due to their compatibility with existing Si-based electronics.<sup>14</sup> Many methods to produce Si-NCs have been reported in

the literature, among them thermolysis of silicon-rich-oxides (SRO) prepared via sol-gel synthesis.<sup>15-18</sup> A technologically relevant, commercially available, SRO, is hydrogen silsesquioxane (HSQ).<sup>19</sup> HSQ yields oxide-embedded Si-NCs (OE-Si-NCs) upon thermal processing at temperatures over 1000 °C under slightly reducing conditions. Adding to the versatility of HSQ, it forms smooth thin films allowing for efficient coating of a variety of substrates including capillaries and fiber optics.<sup>20</sup> OE-Si-NCs prepared by HSQ (and by other methods) exhibit broad luminescence upon photoexcitation.<sup>19</sup> The broad profile is due to a mixture of homogeneous and inhomogeneous broadening sources with the latter playing a significant role. The broad profile can be problematic for the development of Si-NC-based lasing or sensing devices. This thesis described methods to narrow the luminescence observed from photoexcitation of Si-NCs (oxide embedded or free-standing) by sensitization of sharp luminescent species (i.e., Er<sup>3+</sup> ions), by controlling the size distribution, and by confining the luminescence into optical microcavities.

The second chapter of this thesis outlines a method to place Er<sup>3+</sup> ions in close proximity to oxide-embedded Si-NCs (OE-Si-NCs). Er<sup>3+</sup> ions exhibit sharp luminescence at the low-loss window of silica fiber-optics and are routinely used in amplifiers.<sup>21</sup> The luminescence of interest arises from a Laporte forbidden *intra-f* transition with low absorption cross-section. Si-NCs can act as sensitizers absorbing excitation energy and transferring it to neighbouring Er<sup>3+</sup> ions. The method described in Chapter two involves solution mixing HSQ with three different erbium precursors by co-precipitation. This method may be significant

due to the solution processability of HSQ. The solid obtained is heated to 1100 °C under reducing conditions. The optical and physical properties of the resulting material were studied. This investigation began with  $\text{ErCl}_3$ . This precursor displays strong  $\text{Er}^{3+}$  luminescence at the telecommunications relevant wavelength. In addition, mixing with  $\text{ErCl}_3$  does not decrease the solution processability of HSQ (a pivotal property if these materials are going to be used in telecommunication applications). However, SEM studies showed that most of the Er present is in the form of non-optically active  $\text{ErCl}_3$  even after heating. This was attributed to a lack of solution compatibility between the ionic  $\text{ErCl}_3$  and non-polar HSQ. A non-polar solvent Er precursor was studied next. Erbium tris(bis(trimethylsilyl))amide (ErA) is a commercially available precursor soluble in non-polar solvents. Unfortunately, mixing of ErA (even at concentrations below 0.01 at.%) with HSQ caused gelation of the HSQ solution. The gelation was attributed to the strongly basic ligands of ErA (namely hexamethyldisilazane). Gelled solids were heated to 1100 °C producing OE-Si-NCs which display strong  $\text{Er}^{3+}$  luminescence at 1554 nm. In contrast with  $\text{ErCl}_3$ , SEM shows little agglomeration of Er precursors in the composite. However, the observed gelation reduces the solution processability of HSQ. The third precursor studied was Erbium octanoate (ErOct). ErOct can be prepared by reaction of octanoic acid with ErA. ErOct combines the solution compatibility of ErA and the solution processability of  $\text{ErCl}_3$  mixtures. ErOct composites display  $\text{Er}^{3+}$  luminescence with little agglomeration of the rare earth (SEM) and may be useful for signal amplification applications. Lastly, a chemical method to elucidate the

location of the  $\text{Er}^{3+}$  ions in the composite was reported. HF etching of OE-Si-NCs containing  $\text{Er}^{3+}$  ions, strongly suggests the presence of the rare earth atoms in the oxide matrix surrounding the NCs. This was the first demonstration of the use of a chemical method to conclusively identify the location of the ions in the composite material.

Chapter three of this thesis describes a method to pattern OE-Si-NCs using commercially available diblock copolymers. As was discussed previously, some amines can crosslink HSQ. Under certain conditions, diblock copolymers self-assemble to produce micelles which can be patterned on substrates by spin coating.<sup>22,23</sup> When a mixture of HSQ with polystyrene-b-poly4vinylpyridine (PS-b-P4VP) diblock copolymer (BCP) is spin coated on a substrate, the micelles form a hexagonal-closed-pack pattern on the surface. Thermal processing of the substrate under reducing conditions removes the BCP leaving a pattern of OE-Si-NCs discs. The nanodiscs have a height of approximately 3 nm. The diameter and particle-to-particle spacing can be controlled by modifying the molecular weights of the blocks. This inexpensive and straightforward patterning method may help control the size distribution of the NCs. Controlling the size distribution can help reduce the breadth of the luminescence profile. Unfortunately, no PL was observed, possibly due to the low quantity of the emissive species. The patterning method was extended to germanium nanostructures. A polymer with  $\text{GeO}_2$  stoichiometry can be formed via hydrolysis and condensation of tetraethoxygermane using amine moieties as basic catalysts. Thermal processing

yields GeO<sub>2</sub> nanodiscs at temperatures of 400 °C (ambient or slightly reducing conditions) and elemental Ge nanodiscs at 500 °C (20% H<sub>2</sub> / 80% Ar).

Size distribution can also be reduced by etching a NC population to a predetermined size. Such a method will stop once the NCs reach the size of interest producing a narrowly distributed population. An exciton mediated etching method is presented in Chapter four. If a NC sample is irradiated with monochromatic light, an exciton will be formed if the NC bandgap is less than or equal to the energy of the monochromatic light. The hole formed can then migrate to the surface of the crystal polarizing a silicon atom. This will render the silicon atom more electrophilic and thus more prone to HF attack. Etching will proceed until the bandgap is equal to the size of the monochromatic radiation. The PL of free-standing Si-NCs (FS-Si-NCs) prepared by this method can be controlled by changing the radiation wavelength up until 568 nm. Irradiation with higher energy light causes etching to proceed via a non-excitonic pathway. Interestingly, the PL of particles etched using this method does not entirely reflect the size distribution as measured by Small-angle X-ray scattering (SAXS). It is hypothesized that upon removal of the oxide matrix via HF etching, a large percentage of the NC population contains defects that prevent the particle from forming an exciton. Therefore, these particles will not be etched and will not exhibit photoluminescence. A two-step etching method in which the matrix is removed and the crystal surface is passivated using HF:EtOH:H<sub>2</sub>O (water acts as an oxidizing agent) prior to exciton mediated etching was devised. This method

showed narrow size distribution and better agreement between SAXS and PL data.

Another method used to produce narrow luminescence is by coupling the NC radiation with modes in a cavity. Chapter five describes a method to coat non-planar microcavities (capillaries and fiber optics) with OE-Si-NCs using HSQ. The resulting films display strong confinement of the light in the film partly owing to the smoothness of the film. The coating is uniform over distances of a few cm. Light is confined by total internal reflection in the film giving rise to Whispering Gallery modes (WGMs) observable in the PL spectrum. WGMs manifest themselves as sharp peaks superimposed over the broad PL spectrum. A cavity  $Q$ -factor is a figure of merit commonly used to quantify the losses. The method presented in Chapter five yields the highest  $Q$ -factors reported to date for Si-NC luminescence coupled to an optical cavity. The peaks observed in the PL spectra display a full-width-at-half-max of  $\sim 0.3$  nm (i.e. almost three orders of magnitude less than Si-NCs outside of a cavity). In addition, a proof-of-concept sensor that responds to a difference in refractive index in the vicinity of the film surface is presented. WGMs will shift if the refractive index of the medium surrounding the NC film surface is altered. The proof-of-concept sensor can detect variations in concentration of aqueous mixtures containing ethylene glycol or sugar. The sensitivities are comparable to evanescent field measurements.

This thesis reports different methods to decrease the bandwidth of the emission spectrum observed when Si-NC are photoexcited. This is achieved by: sensitization of sharply luminescent ions, decreasing the particle size distribution

and confinement into optical microcavities. Although no luminescence was obtained from the nanodiscs reported in Chapter three, the small dimensions of these structures probably limits the number of particles in a disc and may decrease the size distribution of the particles in a disc. Characterization using more sensitive methods may provide interesting luminescence results. The other three chapters show important results in regards to the bandwidth observed when NCs are optically excited. For example, the full-width-at-half-maximum (FWHM) of the  $\text{Er}^{3+}$  luminescence obtained from sensitized rare-earth ions reported in Chapter two is approximately 40 nm. Free standing silicon nanocrystals etched using laser irradiation (Chapter four) display a FWHM of 83 nm. Lastly, the narrowest modes reported in Chapter five have a FWHM of less than 0.5 nm. These observations are particularly impressive in light of the report by Valenta et al. where the homogeneous distribution of a single nanocrystal at room temperature is suspected to approach 40 nm.<sup>24</sup> These methods provide the means to obtain narrow luminescence using Si-NCs and may be of great importance in the development of biological applications as well as lasing or sensing.

## 6.2. Future work

While this thesis reports some important steps toward decreasing the luminescence bandwidth there is still much work to be done. In the area of erbium sensitization, a more efficient method will involve covalent attachment of erbium species to free-standing silicon nanocrystals. Such method may conclusively answer how many Er ions can be sensitized by a single NC, it will also provide control of the Er-NC distance to maximize transfer efficiency. Further work related to the studies described in Chapter three can be directed toward evaluating the optical response of Si-NCs in a single nanodisc. This could be potentially evaluated using near-field scanning optical microscopy (NSOM) and may provide interesting optical behavior that could be controlled via the molecular weight of the copolymer blocks. Research in Chapter four can be followed by anodic etching of a NC mixture under strongly acidic conditions. Such a method may provide narrower size distributions than those obtained via photoassisted etching. Lastly, the development of a sensitive and selective sensor is certainly possible using optical microcavities. A sensor of this type can be prepared by covalently functionalizing molecules onto the OE-Si-NC surface that can selectively bind to an analyte of interest. Preliminary studies in this area are reported in Appendix A.

### 6.3. References

- (1) Hersam, M. *ACS Nano* **2011**, *5*, 1.
- (2) Fahlman, B. *Materials Chemistry*; Springer: Dordrecht, Netherlands, 2007.
- (3) Huff, H. R. *Into the nano era*; Springer: Electronic reproduction, 2009.
- (4) Smart, L. E. M. E. A. *Solide State Chemistry An Introduction*; 3rd ed.; CRC Press: Florida, USA, 2005.
- (5) Zhang, L.; Gu, F. X.; Chan, J. M.; Wang, A. Z.; Langer, R. S.; Farokhzad, O. C. *Clin. Pharmacol. Ther.* **2008**, *83*, 761.
- (6) Åkerman, M. E.; Chan, W. C. W.; Laakkonen, P.; Bhatia, S. N.; Ruoslahti, E. *P. Natl. Acad. Sci. USA* **2002**, *99*, 12617.
- (7) Medintz, I. L.; Uyeda, H. T.; Goldman, E. R.; Mattoussi, H. *Nat. Mater.* **2005**, *4*, 435.
- (8) Hardman, R. *Environmental Health Perspectives* **2006**, *114*, 165.
- (9) Deaves, M. *Manuf. Eng.* **2004**, *83*, 12.
- (10) Sinha, P.; Kriegner, C. J.; Schew, W. A.; Kaczmar, S. W.; Traister, M.; Wilson, D. J. *Energy Policy* **2008**, *36*, 381.
- (11) Anglin, E. J.; Cheng, L.; Freeman, W. R.; Sailor, M. J. *Adv. Drug Deliver. Rev.* **2008**, *60*, 1266.
- (12) Park, J. H.; Gu, L.; Von Maltzahn, G.; Ruoslahti, E.; Bhatia, S. N.; Sailor, M. J. *Nat. Mater.* **2009**, *8*, 331.
- (13) Erogbogbo, F.; Yong, K. T.; Roy, I.; Xu, G. X.; Prasad, P. N.; Swihart, M. T. *ACS Nano* **2008**, *2*, 873.
- (14) Paniccia, M.; Koehl, S. *IEEE Spectrum* **2005**, *42*, 30.
- (15) Das, G.; Ferraioli, L.; Bettotti, P.; De Angelis, F.; Mariotto, G.; Pavesi, L.; Di Fabrizio, E.; Soraru, G. D. *Thin Solid Films* **2008**, *516*, 6804.
- (16) Sorarù, G. D.; Modena, S.; Bettotti, P.; Das, G.; Mariotto, G.; Pavesi, L. *Appl. Phys. Lett.* **2003**, *83*, 749.
- (17) Henderson, E. J.; Kelly, J. A.; Veinot, J. G. C. *Chem. Mater.* **2009**, *21*, 5426.
- (18) Kelly, J. A.; Henderson, E. J.; Veinot, J. G. C. *Chem. Commun.* **2010**, *46*, 8704.
- (19) Hessel, C. M.; Henderson, E. J.; Veinot, J. G. C. *Chem. Mater.* **2006**, *18*, 6139.
- (20) Hessel, C. M.; Summers, M. A.; Meldrum, A.; Malac, M.; Veinot, J. G. C. *Adv. Mater.* **2007**, *19*, 3513.
- (21) Becker, P. C. O., N.A.; Simpson, J.R. *Erbium-Doped Fiber Amplifiers Fundamentals and Technology*; Academic Press: San Diego, 1999.
- (22) Park, C.; Yoon, J.; Thomas, E. L. *Polymer* **2003**, *44*, 6725.
- (23) Riess, G. *Prog. Polym. Sci.* **2003**, *28*, 1107.
- (24) Valenta, J.; Juhasz, R.; Linnros, J. *Appl. Phys. Lett.* **2002**, *80*, 1070.

**Appendix A:**

**Functionalization of thin  
Oxide-Embedded  
Silicon Nanocrystal  
films with Oligonucleotides**

## A.1. Introduction

Two important attributes relating to the accuracy of a sensor are sensitivity and selectivity among others. Sensitivity can be defined in as: “a) the ability to detect (qualitative analysis) and determine (quantitative analysis) small amounts of an analyte in a sample, and b) the ability to discriminate between similar amounts of an analyte in samples”.<sup>1</sup> The sensitivity is related to the limit of detection of the analytical technique.<sup>1</sup> Selectivity is defined as the “ability of a method to produce signals (and results) that are exclusively dependent on the analyte in the sample.”<sup>1</sup> When an interferent species causes an error in measurement through a mechanism similar to the analyte, the selectivity can be quantified in terms of the sensitivity ratio (1):<sup>1</sup>

$$SR = \frac{S_{analyte}}{S_{interferent}} \quad (1)$$

where  $S_{analyte}$  and  $S_{interferent}$  are the slopes of the linear ranges of the analyte and interferent independent calibration curves. In Chapter five, the sensitivity of a WGM sensor was reported, however the specificity of this analytical technique remains a question. In fact, the refractive-index based sensor lacked specificity because it only responded to changes in  $\eta$  (i.e., it could not differentiate between glucose and EG).

One could envision a chemically selective sensor in which an oligonucleotide is covalently bonded to the surface of a fiber optic or a capillary coated with OE-Si-NCs. A structure of this type will afford sensing via the

bonding and release of complimentary oligonucleotide (See Figure A.1). If a strand of DNA that is complimentary to the surface bonded oligonucleotide is present in solution, it is expected it will bond to the surface and induce a shift in the WGMs. If exposed to a non-complimentary DNA strand hybridization will not occur and thus no shift is expected.

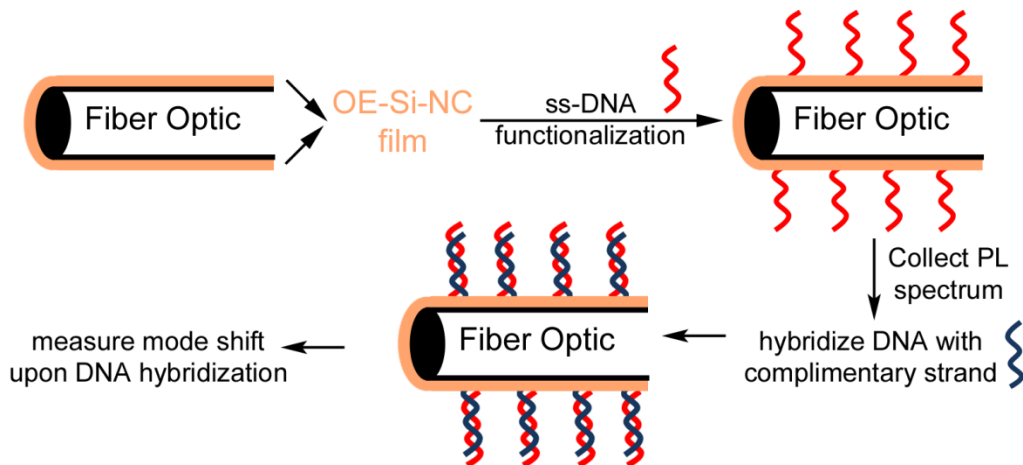


**Fig. A.1** Schematic of a DNA based sensor using WGMs

This Appendix will describe a method to functionalize planar thin films of OE-Si-NCs functionalized with DNA. This is the first step in development of a sensor using OE-Si-NC coated fiber optics. Characterization of the surfaces was complicated by overlap with silica and NC fluorescence.

## **A.2. Experimental**

### **A.2.1. DNA functionalization of glass and OE-Si-NC surfaces**

Quartz substrates were spin coated with HSQ solutions (FOx 15 or 16) and heated to 1100 °C under 5% H<sub>2</sub> / 95% Ar. Substrates were heated to 1100 °C at a rate of 18 °C/min for one hour yielding a thin-film of OE-Si-NCs on quartz.

Surfaces of quartz only and OE-Si-NCs were cleaned by sonication under solvents of increasing polarity (hexanes, acetone, ethanol and water) for 20 minutes. After cleaning, the substrates were exposed to piranha solution to remove any organic impurities and to promote formation of hydroxyl groups on the surface. The substrates were then washed with distilled water while spinning at 3000 rpm for 2 minutes and then spin dried under ambient conditions. The substrates were immediately placed in a solution of m-xylene, 3-glycidoxypropyltrimethoxysilane and N,N-Diisopropylethylamine (100:30:1, v/v/v) under flowing Ar and heated to 80 °C for at least 12 hours.

The 3' amine modified oligonucleotide probe (GGC CGG CGC ATT, Figure A.2) was dissolved in deionized water to a concentration of 50 μM. A 50 μL droplet was placed on the functionalized surface (quartz or OE-Si-NC) and incubated at 36 °C for at least 6 hours in air regulated at 95% relative humidity (5% CO<sub>2</sub>). Unreacted probe was then removed by washing with water.

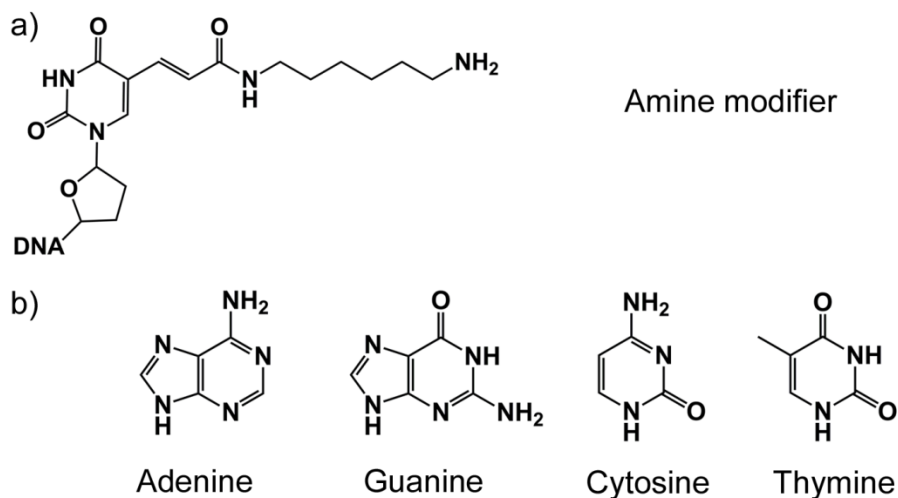


**Fig. A.2** a) Amine modifier used to attach DNA to a quartz or OE-Si-NC surfaces. b) DNA bases.

For luminescence detection, fluorescent complimentary strands (GCG CCG GCC with 6-FAM attached to the 3' end) were diluted in a standard hybridization buffer (3M Tetramethylammonium chloride, 60 mM Tris buffer, 6 mM EDTA and 0.03% SDS) to a concentration of 5  $\mu$ M. Substrates were exposed for two hours to the hybridization solution at  $\sim 5$   $^{\circ}$ C. The hybridization solution was then replaced by 50  $\mu$ L of the fluorescent DNA solution for at least 2 hours at  $\sim 5$   $^{\circ}$ C. After hybridization, the substrates were washed with cold water ( $<10$   $^{\circ}$ C) followed by air drying. Substrates were characterized by photoluminescence spectroscopy and X-ray photoelectron spectroscopy.

### **A.2.2. X-ray photoelectron spectroscopy (XPS)**

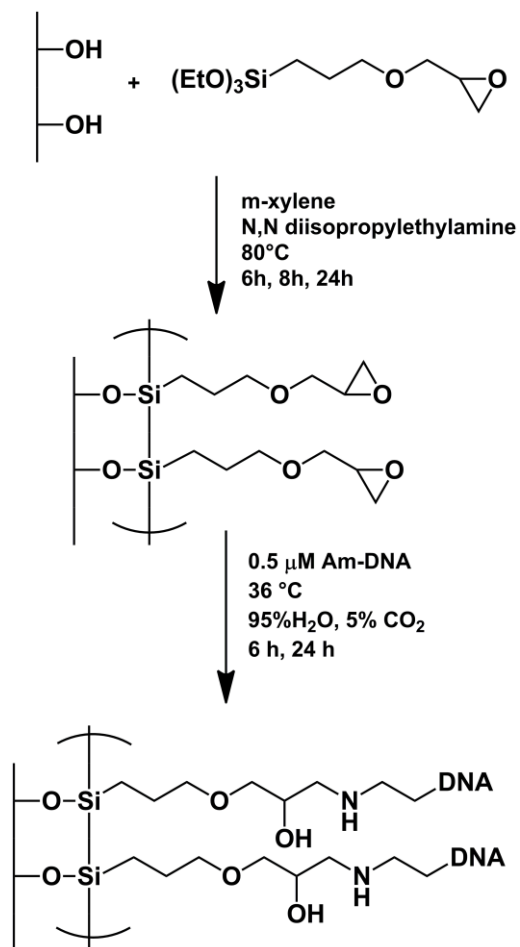
Surfaces functionalized with DNA were characterized using an AXIS -165 spectrometers (Kratos Analytical) at the Alberta Centre for Surface Engineering and Science (ACSES), University of Alberta. The base pressure in the analytical chamber was lower than  $3 \times 10^{-8}$  Pa. Monochromatic Al K $\alpha$  source ( $h\nu = 1486.6$  eV) was used at a power of 210 W. The analysis spot was 400 x 700  $\mu\text{m}$ . The resolution of the instrument is 0.55 eV for Ag 3d and 0.70 eV for Au 4f peaks. For the high-resolution spectra the pass-energy was 20 eV with a step of 0.1 eV. Electron flooding was required to compensate the sample charging during the analysis.

### **A.2.3. Photoluminescence (PL) measurements**

The 325 nm line of a He/Cd laser (non-resonant with Er<sup>3+</sup> excitation) was used to excite all samples presented in this study. The spectral response was corrected using a standard blackbody radiator. Luminescence between 300 nm and 1000 nm was detected using a USB2000 spectrometer from Ocean Optics. Laser light was filtered out using a coloured glass long pass filter purchased from Thor Labs.

### A.3. Results and Discussion

Because characterizing a monolayer of DNA on a delicate non-planar surface (e.g., capillaries or fiber optics) is non-trivial, DNA functionalization of planar quartz (SiO<sub>2</sub>) and OE-Si-NC surfaces was attempted. Quartz discs with an HSQ thin-film were heated to 1100 °C for one hour to yield a film (thickness ~500 nm according to Dow Corning Corporation Information) of OE-Si-NCs. After excitation using the 325 nm line of a He/Cd laser, the film displayed the characteristic red luminescence arising from OE-Si-NCs. Covalent attachment of the oligonucleotide was performed using a method similar to that reported by Lamture *et al.*<sup>2</sup> Cleaned quartz substrates and OE-Si-NC surfaces are first epoxisilanized using 3-glycidoxypropyltrimethoxysilane in m-xylene. Following surface attachment of the epoxide group, it was apparent that the functionalized surfaces had become more hydrophobic (compared to untreated substrates). This was noted when adding the aqueous oligonucleotide solution for covalent attachment. Oligonucleotides were subsequently attached to the surface via reaction of amine terminations with the surface bonded epoxide in humid air (95% H<sub>2</sub>O, 5% CO<sub>2</sub>).



**Scheme A.1** Quartz and OE-Si-NC surfaces have hydroxyl groups on the surface which can undergo epoxysilanization upon standard based catalyzed sol-gel reaction. The epoxide ring is opened using an amine terminated DNA strand dissolved in water.

A fluorescently labelled (6-FAM,  $\lambda_{\text{em}} = 495 \text{ nm}$ ,  $\lambda_{\text{ex}} = 517 \text{ nm}$ ) oligo strand was hybridized with its complimentary strand (c-DNA) (attached to the surface) at 4 °C at low temperatures. Following hybridization, the substrates were rinsed with cold water (< 10 °C) and the PL studied. Evaluation of DNA binding

(measured via fluorescence of the c-DNA) was inconclusive. Quartz substrates with fluorescent DNA hybridized onto the substrate displayed PL at 517 nm upon excitation using a 325 nm laser line. Unfortunately, control substrates also display PL in this spectral region (although of low intensity) (Figure A.3.a); this precluded confirmation of DNA attachment via PL analysis. Characterization of DNA functionalized OE-Si-NC surfaces was not possible because the tail of the NC luminescence lies in the same spectral region as the 6-FAM.

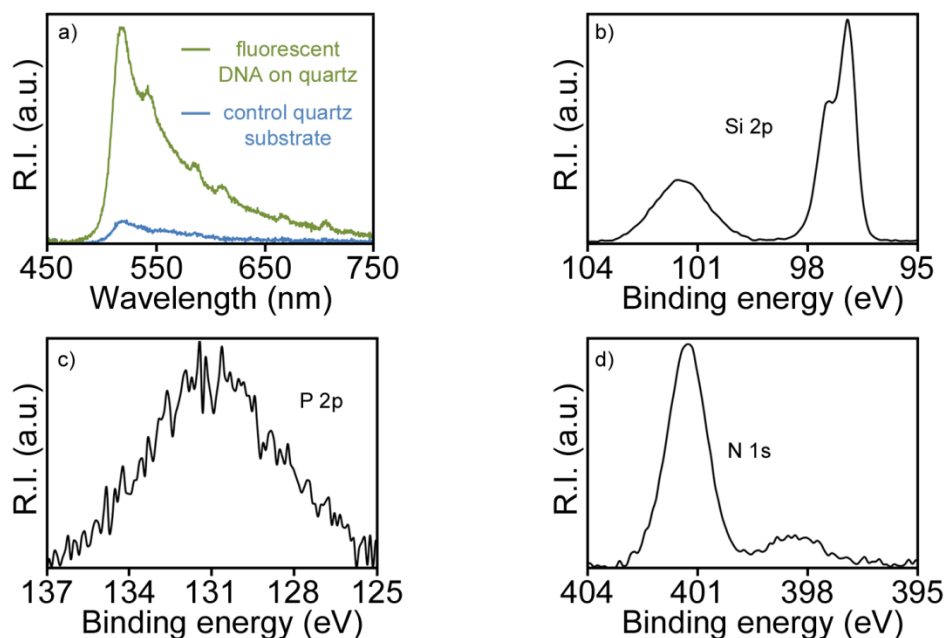


**Fig. A.3** a) PL of a quartz surface exposed to fluorescently labeled DNA (green trace) and a control quartz substrate not exposed to fluorescent DNA (blue trace). XPS spectra of an OE-Si-NC surface with covalently bound DNA showing the b) Si (2p), c) P (2p), and d) N (1s) binding energies.

XPS was used to thoroughly characterize DNA attachment to a surface coated with OE-Si-NCs. XP spectra of Si (Figure A.3.b) shows three features at 96.9 eV, 97.5 eV (shoulder), and at 101 eV. Figure A.3.c,d show peaks corresponding to the N 1s and P 2p binding energies confirming the presence of DNA on the surface, however it is unclear whether the DNA is physisorbed or chemisorbed to the OE-Si-NC surface.

#### **A.4. Conclusions and Future work**

A DNA sensor was envisioned using a fiber optic coated with OE-Si-NCs which has a single strand of DNA covalently bound to the surface. Resonance shifts can be expected upon DNA binding as this event will produce a change in the refractive index surrounding the luminescent film. A modified method to bind a single strand of DNA to flat substrates was studied as a first step towards the development of the sensor. Unfortunately, the fluorescent DNA used ( $\lambda_{EM} = 517$  nm) overlaps with the broad luminescence arising from Si-NCs. Further XPS studies used to characterize the functionalized surfaces suggest a mixture of covalently bound DNA and unreacted material.

To prepare the proposed sensor, a reproducible method to functionalize and characterize surfaces with DNA must be demonstrated. XPS characterization may be able to prove DNA attachment, however surface cleaning techniques that completely remove physisorbed impurities need to be improved for this characterization method to be reliable. Fluorescent detection of a complimentary strand will be problematic due to the overlapping Si-NC luminescence. Unfortunately, commercially available DNA labels in the IR or UV (outside of the NC luminescence range) are not readily available. Furthermore, excitation sources for dyes in these ranges are limited. A different alternative can be the hybridization with a radiolabeled strand. This approach will circumvent the issues arising from the NC luminescence. Developing a procedure to attach DNA to planar OE-Si-NC surfaces is the first step towards building a DNA sensor.

## A.5.       References

- (1)     *Analytical chemistry : a modern approach to analytical science*;  
2nd Edition ed.; Wiley-VCH: Weinheim. Great Britain, 2004.
- (2)     Lamture, J. B.; Beattie, K. L.; Burke, B. E.; Eggers, M. D.; Ehrlich,  
D. J.; Fowler, R.; Hollis, M. A.; Kosicki, B. B.; Reich, R. K.; Smith, S. R.;  
Varma, R. S.; Hogan, M. E. *Nucleic Acids Res.* **1994**, 22, 2121.

**Appendix B:**

**Capillary and Fiber**

**Mode Modeling**

**and**

**Indexing**

## B.1. Mode Modeling and Indexing

A theoretical analysis was performed by Dr. Pablo Bianucci to model the mode spectra by using the capillary (fiber) inner diameter (diameter), film thickness, and refractive index as variable parameters. Each WGM was characterized by its polarization (transverse electric, TE, or transverse magnetic), azimuthal mode number  $l$ , and radial mode number  $p$ . The radial distribution of the field in a mode is given by:

$$F_z(r)^{(l,p)} = \begin{cases} AJ_l(k_0^{(p)}\eta_{air}r), & r \leq r_1 \\ BJ_l(k_0^{(p)}\eta_{film}r) + CH_l^1(k_0^{(p)}\eta_{film}r), & r_1 \leq r \leq r_2, \\ DH_l^1(k_0^{(p)}\eta_{glass}r), & r \leq r_2 \end{cases} \quad (3)$$

where  $J_l$  and  $H_l^{(1)}$  are Bessel functions of the first and third kind and  $F_z$  is the electric (magnetic) field for TM (TE) modes. Enforcing boundary conditions at the interfaces results in a characteristic equation that can be numerically solved to find the mode resonant wavelength.

$$\begin{vmatrix} J_l(k_0^{(p)}n_{air}r_1) & -J_l(k_0^{(p)}n_{film}r_1) & -H_l^{(1)}(k_0^{(p)}n_{film}r_1) & 0 \\ J_l'(k_0^{(p)}n_{air}r_1) & -J_l'(k_0^{(p)}n_{film}r_1) & -H_l^{(1)'}(k_0^{(p)}n_{film}r_1) & 0 \\ 0 & J_l(k_0^{(p)}n_{film}r_2) & H_l^{(1)}(k_0^{(p)}n_{film}r_2) & -H_l^{(1)}(k_0^{(p)}n_{glass}r_2) \\ 0 & J_l'(k_0^{(p)}n_{film}r_2) & H_l^{(1)'}(k_0^{(p)}n_{film}r_2) & -H_l^{(1)'}(k_0^{(p)}n_{glass}r_2) \end{vmatrix} = 0. \quad (4)$$

Equation (4) was used to index the modes in the measured spectra. The known inner diameter and film thickness of the capillaries were used as fixed parameters while  $\eta_{film}$  was adjusted to achieve the best agreement with the observed spectrum. The optimal match was found for  $\eta_{film}=1.67$  consistent with literature values for Si-NC films.<sup>1</sup> Applying this process to the 25  $\mu\text{m}$  capillary

allowed indexing of all the observed modes. Limitations associated with the numerical evaluation of the higher-order Bessel functions allowed only partial indexing of the 50  $\mu\text{m}$  fibers. A similar process was used to index the modes arising from OE-Si-NCs coating a fiber optic.

## B.2. References

- (1) Rodríguez, J. R.; Veinot, J. G. C.; Bianucci, P.; Meldrum, A. *Appl. Phys. Lett.* **2008**, 92.